

The Mass Dependence Between Protoplanetary Disks and their Stellar Hosts

Sean M. Andrews, Katherine A. Rosenfeld, Adam L. Kraus, and David J. Wilner

Harvard-Smithsonian Center for Astrophysics, 60 Garden Street, Cambridge, MA 02138, USA

sandrews@cfa.harvard.edu

ABSTRACT

We present a substantial extension of the millimeter-wave continuum photometry catalog for circumstellar dust disks in the Taurus star-forming region, based on a new “snapshot” $\lambda = 1.3$ mm survey with the Submillimeter Array. Combining these new data with measurements in the literature, we construct a mm-wave luminosity distribution, $f(L_{\text{mm}})$, for Class II disks that is statistically complete for stellar hosts with spectral types earlier than M8.5 and has a $3\text{-}\sigma$ depth of roughly 3 mJy. The resulting census eliminates a longstanding selection bias against disks with late-type hosts, and thereby demonstrates that there is a strong correlation between L_{mm} and the host spectral type. By translating the locations of individual stars in the Hertzsprung-Russell diagram into masses and ages, and adopting a simple conversion between L_{mm} and the disk mass, M_d , we confirm that this correlation corresponds to a statistically robust relationship between the masses of dust disks and the stars that host them. A Bayesian regression technique is used to characterize these relationships in the presence of measurement errors, data censoring, and significant intrinsic scatter: the best-fit results indicate a typical 1.3 mm flux density of ~ 25 mJy for $1 M_\odot$ hosts and a power-law scaling $L_{\text{mm}} \propto M_*^{1.5-2.0}$. We suggest that a reasonable treatment of dust temperature in the conversion from L_{mm} to M_d favors an inherently linear $M_d \propto M_*$ scaling, with a typical disk-to-star mass ratio of $\sim 0.2\text{--}0.6\%$. The measured RMS dispersion around this regression curve is ± 0.7 dex, suggesting that the combined effects of diverse evolutionary states, dust opacities, and temperatures in these disks imprint a FWHM range of a factor of ~ 40 on the inferred M_d (or L_{mm}) at any given host mass. We argue that this relationship between M_d and M_* likely represents the origin of the inferred correlation between giant planet frequency and host star mass in the exoplanet population, and provides some basic support for the core accretion model for planet formation. Moreover, we caution that the effects of incompleteness and selection bias must be considered in comparative studies of disk evolution, and illustrate that fact with statistical comparisons of $f(L_{\text{mm}})$ between the Taurus catalog presented here and incomplete subsamples in the Ophiuchus, IC 348, and Upper Sco young clusters.

Subject headings: protoplanetary disks — submillimeter: planetary systems

1. Introduction

Planetary systems are forged from the gas-rich, dusty disks that orbit young stars. The physical mechanisms related to that formation process are extraordinarily complex, so there is considerable ambiguity (and lively theoretical debate) on the dominant pathways and pitfalls involved in producing the planets in our solar system and the larger exoplanet population from their ancestral disks. Yet despite all that uncertainty, theoretical models agree that the overall efficiency of the process depends strongly on the amount of raw material available in the circumstellar disk. Therefore, in the context of planet formation, *mass* is a fundamental disk property. The distribution of disk masses, $f(M_d)$, has been invoked as a key factor in accounting for the diverse demographic properties of the exoplanets (e.g., Ida & Lin 2004, 2008; Alibert et al. 2005; Mordasini et al. 2009), and scaling trends between M_d and other star/disk properties are speculated to generate some of the basic relations that are now being identified from observations of the exoplanet population. The most notable example of the latter is the correlation between the giant planet frequency and stellar host mass (M_*) noted by Johnson et al. (2007), which was predicted theoretically in planet formation models that implicitly assumed there is a fundamental scaling relationship between M_d and M_* (e.g., Laughlin et al. 2004; Ida & Lin 2005; Kornet et al. 2006; Alibert et al. 2011).

The best available observational diagnostic of M_d comes from the thermal continuum emission generated by cool dust grains at (sub)millimeter/radio wavelengths (Beckwith et al. 1990). In this part of the spectrum, the dust emission is optically thin over most of the disk volume: therefore, the mm-wave luminosity is directly proportional to the product of the total mass and (average) temperature of the dust, weighted by the grain emissivity – $L_\nu \propto \kappa_\nu B_\nu(T) M_d$. With this simple relation (and some reasonable assumptions for κ_ν and the gas-to-dust ratio), mm-wave photometry surveys can be used to construct a disk mass distribution (Andrews & Williams 2005, 2007a), and study how it varies as a function of time (Carpenter et al. 2005; Lee et al. 2011; Mathews et al. 2012), environment (Mann & Williams 2009, 2010), or host mass (e.g., Scholz et al. 2006; Schaefer et al. 2009). Previous work has suggested that disk masses are substantially diminished by advanced age (by $\sim 3\text{--}5$ Myr) or proximity to massive (OB-type) stellar neighbors, and are perhaps intrinsically lower for later type (M) stellar hosts. In principle, such results hold clues to the nature of disk evolution and some of the key initial conditions relevant to the planet formation process.

However, the quantitative inferences of those studies should be regarded with caution. In practice, this work relies on comparisons relative to a “reference” $f(M_d)$, constructed from a deep mm-wave photometry survey of disks in the Taurus region (Andrews & Williams 2005). Because of its proximity ($d \approx 140$ pc) and youth (~ 2 Myr), Taurus receives considerable (some might say disproportionate) attention from astronomers. However, it comprises the most complete and best-characterized young cluster available, and therefore is the most desirable stellar population to use in building a reference $f(M_d)$ for the comparative work noted above. Unfortunately, it is not generally appreciated that such comparisons are problematic because the reference census of Andrews & Williams (2005) is *incomplete* and *biased* against low-mass stellar hosts. In fact, nearly half of the M stars with disks in Taurus had regrettably never been observed at millimeter

wavelengths. Since the M stars represent the peak of the stellar mass function and a wide range in M_* (a factor of ~ 10), a complete census of their disk masses is vital in efforts to develop a more appropriate reference $f(M_d)$ and to facilitate a robust search for any relationship between disk and star masses.

In this article, we present an extension of the Taurus disk mass survey based on “snapshot” observations with the Submillimeter Array that is complete for known Class II sources with spectral types earlier than M8.5, and has a mm-wave luminosity sensitivity comparable to the Andrews & Williams (2005) study. In Section 2, we describe the extension of the sample as well as the new millimeter continuum observations and their calibration. In Section 3, we construct an updated distribution of mm-wave flux densities ($\propto M_d$) for Taurus disks, consider how it depends on various environmental and evolutionary factors, and directly explore the basis for a relationship between M_d and M_* . The results are discussed in Section 4 in the contexts of practical consequences for future comparative observational work, implications for theoretical models of planet formation, and potential demographic connections in the populations of circumstellar disks and exoplanets. A summary of the key conclusions of this work is provided in Section 5, and an extensive data catalog is made available in an Appendix (and through a web-accessible electronic database).

2. Sample Selection and New Observations

The Taurus-Auriga region includes a few hundred young, low-mass stars interspersed among small groups of dark clouds, spanning roughly 100 square degrees on the sky (e.g., Kenyon et al. 2008). Historical spectroscopic parallax estimates have favored a mean distance of $d \approx 140 \pm 20$ pc to the association, in good agreement with a few precise, individual trigonometric parallaxes from VLBI measurements (Loinard et al. 2007; Torres et al. 2009, 2012). Although a distributed population of Class III (young, but presumably disk-less) sources may still remain elusive (e.g., Herbig 1978; Neuhaeuser et al. 1995; Slesnick et al. 2006), there is a robust, vetted, and effectively complete list of Class II (those with infrared excesses indicative of disks) members available thanks to the deep, wide coverage afforded by various *Spitzer* photometry surveys (Luhman et al. 2010; Rebull et al. 2010). The infrared-selected Luhman et al. catalog of Tau-Aur Class II sources is used as the basis of our sample: it includes 179 young stellar “systems” composed of 227 (known) individual stars with spectral types from B8 to M9 (e.g., Luhman 2000, 2004; Kraus et al. 2011).

Of those 179 systems in the full sample, only 82 ($\sim 46\%$) were included in the Andrews & Williams (2005) (sub)mm continuum photometry catalog (or its precursors). The incompleteness of that catalog is due to a strong bias with respect to the spectral type of the host star, such that most of the M type stars were not observed: measurements were available for 31/50 (62%) of the M0-M2 hosts, 16/45 (36%) for M2-M5, and *none* of those later than M5.¹ A clear demonstration of this

¹For historical purposes, it is worth pointing out some of the underlying circumstances that resulted in this selection

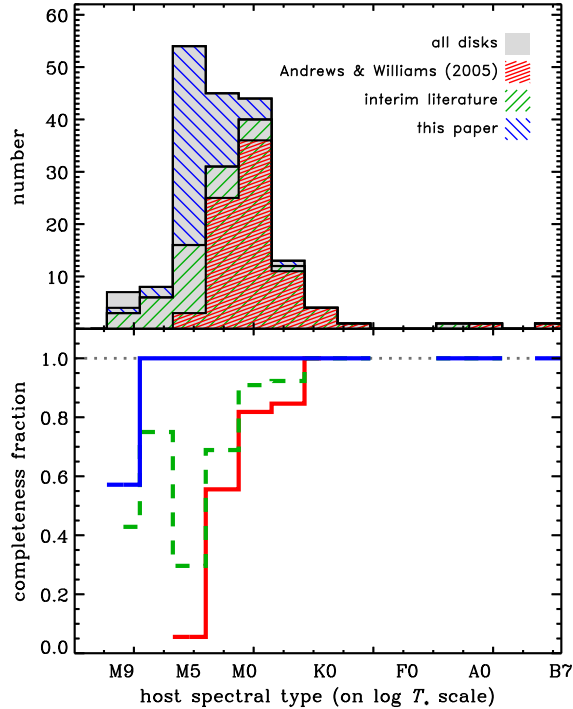


Fig. 1.— (*top*) The distribution of stellar host spectral types (on a $\log T_*$ scale; see Appendix A) for all Taurus Class II members (*gray* background), those in the Andrews & Williams (2005) mm-wave photometry catalog (*red*), plus new measurements since that survey (*green hatched*), and finally including those that have been observed here (*blue hatched*). The new data cover most of the M-type hosts. (*bottom*) The fractional completeness of the mm-wave photometry in the same spectral type bins. The extended sample presented here is complete for types earlier than M8.5.

selection bias is shown in Figure 1. Since the Andrews & Williams (2005) catalog was published, an additional 34 sources have been observed at (sub)mm wavelengths, including a number of M-type hosts (e.g., Scholz et al. 2006; Schaefer et al. 2009). However, Figure 1 demonstrates that even this updated catalog remains highly incomplete for late-type hosts. To remedy that issue, we identified 60 of those remaining sources and designed a survey to measure their mm-wave continuum emission. Combined with the previous measurements, this new sample of 176 sources is *complete* for Class II members with host spectral types earlier than M8.5 (and $\sim 50\%$ complete for later types).

We observed 52 new targets with the Submillimeter Array (SMA; Ho et al. 2004) in its compact configuration (8-70 m baselines) over six tracks from 2012 November to 2013 February. The data

bias. First, the Andrews & Williams (2005) survey was largely conducted in 2003-2004, before the full population of late type Class II sources had been identified or confirmed through *Spitzer* infrared photometry surveys. And second, even had a full sample been vetted, the long-term survey goals of that project would still have been cut short by the (premature) decommissioning of the primary instrument used for the photometry (SCUBA on the JCMT).

were collected in a “snapshot” observing mode, where short integrations on ~ 5 –11 individual targets were interspersed throughout each track, along with brief visits to the nearby quasar 3C 111. Additional observations of Uranus, Callisto, 3C 279, and 3C 84 were conducted for calibration purposes when the science targets were at low elevations. The total integration time per target was ~ 45 minutes. Although this snapshot approach degrades the image fidelity, it facilitates robust flux density measurements for a large number of targets in a short period of time. The SMA double-sideband receivers were tuned to a local oscillator (LO) frequency of 225.5 GHz (1.33 mm), and the correlator was configured to process two IF bands that spanned ± 4 –8 GHz from the LO with 48×108 MHz spectral chunks (each with 32 individual channels) per sideband. The observing was performed in good weather conditions, with precipitable water vapor levels in the 1–2 mm range. An additional 8 targets were found to have useful data in the SMA archive, and are included here.

The data were calibrated with the MIR software package. The spectral response of the system was corrected using observations of 3C 279 and 3C 84, and the visibility amplitude scale was bootstrapped from the observations of Uranus or Callisto, depending on their availability. The absolute amplitude scale has a systematic uncertainty of $\sim 10\%$. Antenna-based complex gain variations from instrumental and atmospheric effects were removed by referencing to regular observations of 3C 111. The visibility spectra for each science target were averaged into a composite wideband continuum dataset for each IF band/sideband pair and then concatenated. The visibilities were Fourier inverted, deconvolved with the CLEAN algorithm, and then restored with the synthesized beam using the MIRIAD package. The resulting continuum emission maps have RMS noise levels of 0.5–2.1 mJy beam $^{-1}$. Flux densities were measured both from these maps and directly from the visibilities (both methods are in agreement in all cases): when no emission is detected, we report upper limits that correspond to $3\times$ the RMS noise level in the corresponding map. Table 1 lists the flux densities or $3\text{-}\sigma$ upper limits for the 60 new targets provided by this survey.

3. Analysis and Results

Combined with previous measurements in the literature, the new observations described above allow us to construct a deep mm-wave photometry catalog of Class II disks that is complete for stellar host spectral types earlier than M8.5. In this section, we generate and analyze an updated set of mm-wave continuum luminosity distributions (§3.1), and investigate the potential dependence of the emission from these dust disks (i.e., their masses) on the masses of their stellar hosts (§3.2).

3.1. Millimeter-wave Luminosity Distributions

Before starting any analysis of the full sample, the diverse set of literature photometry measurements needs to be homogenized. The extension catalog described in §2 was observed at $\lambda = 1.33$ mm, but the literature catalogs include photometry (or upper limits) for each source

at wavelengths of 0.86–0.88 and/or 1.2–1.4 mm. Often, the sources with measurements in both wavelength ranges have one that is significantly more reliable or useful due to its higher signal-to-noise ratio or intrinsically deeper limit. These issues can be mitigated by using all of the available data to generate representative flux densities (or upper limits) from an extrapolation to a “reference” frequency. To facilitate comparisons with future work, two reference frequencies are adopted here based on our expectations of common observing setups for surveys with the Atacama Large Millimeter/Submillimeter Array (ALMA): $\nu_{\text{ref}} = 225$ GHz (1.3 mm) and 338 GHz (0.89 mm). The former corresponds to an ALMA configuration that simultaneously covers the $^{12}\text{CO}/^{13}\text{CO}/\text{C}^{18}\text{O}$ $J=2-1$ lines, while the latter includes the $J=3-2$ transitions of $^{12}\text{CO}/^{13}\text{CO}$ and avoids regions of poorer atmospheric transmission. For the 60 sources in the full catalog with ≥ 2 detections in the 0.7–3 mm wavelength range, we determined flux densities at the reference frequencies from power-law fits, where $F_\nu \propto \nu^\alpha$. In all other cases, we applied an extrapolation based on a weighted average of those fit results, with an effective index $\langle \alpha \rangle = 2.4 \pm 0.5$. The uncertainties on the homogenized flux densities include the uncertainty on the index α . For sources with no available detections, the intrinsically deeper observation is used to extrapolate upper limits at the reference frequencies. Since many more sources in the full sample have measurements at (or near) 1.3 mm, our analysis and results are discussed in the context of this wavelength. A comment on notation: in this article, we use the terms mm-wave “flux density” (F_{mm}) and “luminosity” (L_{mm}) interchangeably, but prefer to employ the standard units (Jy) of the former for ease of use in literature comparisons.²

Next, we adopt an approach for the assignment of emission to individual components of multiple star systems. The recent component-resolved imaging survey by Harris et al. (2012) is used for brighter systems with separations $> 0''.3$. When no component-resolved measurements are available, F_{mm} values are assigned based on the projected separation between a pair of stars. For close pairs ($\leq 0''.1$, roughly 15 AU), dynamical simulations of star-disk interactions suggest that individual disks are unlikely to survive (e.g., Artymowicz & Lubow 1994). In those cases, we associate the emission (or lack thereof) with a circumbinary disk around both components. For undetected systems with wider separations, the measured upper limit is assigned to each individual component. Finally, there are 8 multiple systems³ (containing 16 stars) that are detected but not yet resolved at mm wavelengths. In those cases, we assume that all of the emission is associated with the primary and assign the secondaries an upper limit corresponding to $3\times$ the quoted RMS noise level for the system. For this last scenario, our motivation comes from two considerations. First, Harris et al. (2012) found that the primary component always dominates the F_{mm} budget for binary pairs, and is often the *only* component of a multiple system with any mm-wave emission. And second, the multiplicity census for late-type stellar hosts is likely incomplete, meaning that we may already be de facto assigning F_{mm} in this way for some sources that we assume are single, but may actually have faint companions. Overall, this assumption applies to few enough sources that it is effectively

²Note that $L_{\text{mm}}/L_\odot \approx 0.0014(F_{\text{mm}}/\text{Jy})$ at 1.3 mm, or $\approx 0.0021(F_{\text{mm}}/\text{Jy})$ at 0.89 mm, for a distance $d = 140$ pc.

³FO Tau, FS Tau, XZ Tau, GH Tau, IS Tau, Haro 6-28, GN Tau, and V955 Tau.

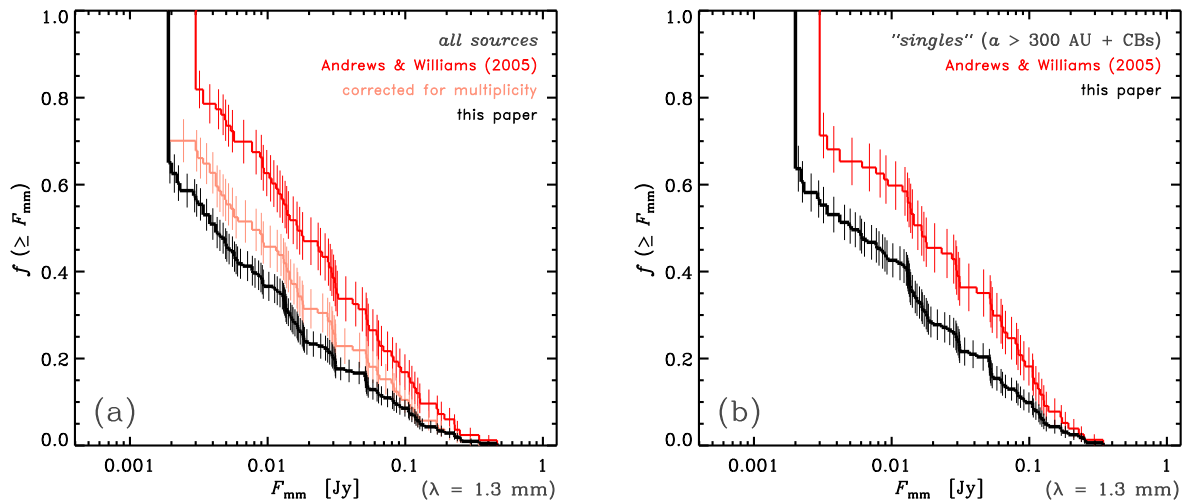


Fig. 2.— (a) The cumulative mm-wave luminosity distributions for the complete sample presented here (*black*) and the original Andrews & Williams (2005) catalog as published (*red*) and corrected for multiplicity (*pink*). The complete sample has systematically lower luminosities, due to selection biases in previous catalogs. (b) The same cumulative distributions, but only for sources where the influence of a companion on the disk properties is minimal: single stars, close pairs with circumbinary disks, and wide binaries. The difference between the two curves is entirely due to selection effects related to the distribution of host stars in the two samples.

inconsequential in the analysis that follows: alternative assumptions – e.g., that the emission is distributed equally to each component – do not significantly impact any of the results.

Based on the homogenization and emission assignments outlined above, a catalog of F_{mm} values at both reference frequencies for the full sample of Taurus Class II members is provided in Table 2. For reference purposes, the original photometric measurements used to determine these representative F_{mm} are available for each individual source in electronic format in Appendix A.

The catalog in Table 2 is used to generate the cumulative distribution of mm-wave luminosities, $f(\geq F_{\text{mm}})$, shown in Figure 2(a) (*black curve*). This distribution corresponds to a statistically complete sample of Class II disks in Taurus with host spectral types earlier than M8.5, and was constructed using the Kaplan-Meier product-limit estimator to properly account for censored measurements (upper limits on F_{mm}) using the formalism described by Feigelson & Nelson (1985). Its shape can be described reasonably well using a log-normal function with a mean of 4 mJy (the median F_{mm} is the same) and a large standard deviation, 0.9 dex (at the alternative reference wavelength of 0.89 mm, the mean is 11 mJy and the standard deviation is also ~ 0.9 dex).

This cumulative luminosity distribution is dramatically different than the one derived from the Andrews & Williams (2005) catalog; the latter is also shown in Figure 2(a) (*red curve*), updated to use the homogenized F_{mm} values. Some of that discrepancy is related to the proper assignment

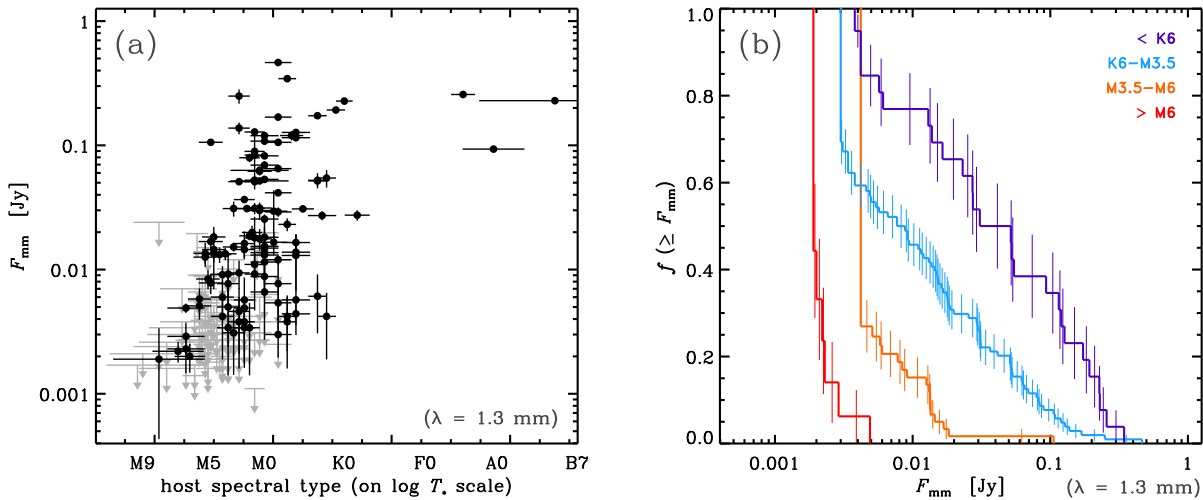


Fig. 3.— (a) The dependence of the mm-wave luminosities from dust disks (3σ upper limits are marked as *grey* arrows) on the spectral types of their stellar hosts: the abscissa axis represents a logarithmic effective temperature scale (see text for details). Statistical tests confirm that there is a clear correlation between these two variables. (b) An illustration of the same relationship, through a comparison of cumulative luminosity distributions for different spectral type bins. The mm-wave luminosities are systematically larger for disks around stellar hosts with earlier spectral types.

of emission in multiple systems: Andrews & Williams (necessarily) treated these as composite systems. After applying a correction based on the accounting system described above (*pink curve*), we find that the overall shapes of the $f(\geq F_{\text{mm}})$ distributions are similar, but the complete sample is preferentially shifted to $\sim 50\%$ lower luminosities (for $F_{\text{mm}} < 0.1$ Jy). The blanket inclusivity of Figure 2(a) obscures how notable the differences are between the old and new catalogs. Figure 2(b) compares the $f(\geq F_{\text{mm}})$ for sources where multiplicity is not expected to substantially diminish the mm-wave emission – for single stars, close pairs with circumbinary disks, and wide binaries with projected separations $a > 300$ AU (Harris et al. 2012) – and highlights a large discrepancy that more faithfully reflects the impact of incompleteness in the Andrews & Williams (2005) sample. In short, a comparison between the mm-wave luminosity distributions for the complete sample and the standard Andrews & Williams (2005) reference catalog confirms that the latter is demonstrably biased toward brighter sources. Since the primary difference between the two samples was the addition here of many new targets with late-type stellar hosts (see Fig. 1), it makes sense to suspect that such sources exhibit preferentially fainter mm-wave emission.

That simple inference is directly examined for the full sample catalog in Figure 3(a), which plots F_{mm} as a function of the host spectral type. The abscissa values are marked on a logarithmic effective temperature (T_*) scale that assumes the standard correspondence with spectral types earlier than M1 (Schmidt-Kaler 1982; Straižys 1992) and the updated T_* scale advocated by Luhman (1999) for later types (as in Fig. 1; see Appendix B for more details). The behavior in this plot

clearly demonstrates that later type stellar hosts harbor disks with systematically lower emission levels, and have an overall lower detection rate compared to their counterparts with earlier types. The standard correlation tests for censored datasets described by Isobe et al. (1986) – the Cox proportional hazard, generalized Kendall rank, and generalized Spearman rank tests – all verify that the null hypothesis is ruled out with very high confidence (i.e., the probability that there is no correlation between F_{mm} and T_* is very low, $p_0 < 10^{-8}$). Figure 3(b) renders the correlation more visually recognizable by splitting the cumulative luminosity distribution into spectral type bins, and thereby showing a clear increasing progression of F_{mm} for earlier spectral types.

The identification of this correlation between L_{mm} and T_* is possible only because the sample presented here is complete over a large range of host spectral types. That new capability illustrates clearly why it is so important to obtain complete samples without selection biases (or to properly account for them; see §4) in demographic studies of disk populations. But perhaps more important, it provides some tantalizing evidence for an intrinsic relationship between the masses of disks and their stellar hosts: L_{mm} is roughly proportional to M_d , and T_* (i.e., the spectral type) scales with M_* over a wide range of young star masses. Nonetheless, there is a large amount of scatter both in the data and in the intrinsic relationships between these *observed* properties, $\{L_{\text{mm}}, \text{spectral type}\}$, and their *derived* analogs, $\{M_d, M_*\}$. The following section aims to map the conversion between the two and explore the basis for a relationship between M_d and M_* more explicitly.

3.2. Dependence on Stellar Host Masses

3.2.1. Derivation of M_* Estimates

In our effort to derive these fundamental stellar properties, we use the Bayesian inference approach first derived by Jørgensen & Lindegren (2005), and later developed by Gennaro et al. (2012). For each individual star, the goal is to determine the joint likelihood function $\mathcal{L}(M_*, t_* | T_*, L_*)$, which characterizes the desired model properties (mass and age) conditioned on a measurement of its temperature and luminosity. However, a determination of $\{T_*, L_*\}$ and their associated uncertainties from directly observable quantities is not trivial. Here, we adopt a simple scaling relation with the spectral classification to assign T_* (see §3.1) and then use a stochastic optimization fitting method to determine L_* (and an extinction, A_V) by matching scaled and reddened spectral templates of stellar photosphere models to the broadband optical/near-infrared spectral energy distribution (SED). Since this effort is not intended to be the focus here, we relegate a detailed explanation of this process and a compilation of the results to Appendix B.

The underlying “model” involved in this technique is a grid of pre-main sequence (pre-MS) stellar evolution calculations. To capture the intrinsic uncertainties in (or disagreements between) these grids themselves (e.g., see Hillenbrand & White 2004), we consider three different sets of model calculations: D’Antona & Mazzitelli (1997, hereafter DM97) with the updated prescription for deuterium burning (D’Antona & Mazzitelli 1998), Baraffe et al. (1998, BCAF98), and

Siess et al. (2000, SDF00). Each grid is used to construct a finely interpolated (discretized) model H-R diagram, with coordinates $\{\hat{T}, \hat{L}\}$. For each individual star and pre-MS model grid, a conditional likelihood function is then defined and evaluated for each location in the model H-R diagram:

$$\mathcal{L}(\hat{T}, \hat{L}|T_*, L_*) = \frac{1}{2\pi\sigma_T\sigma_L} \exp\left(-\frac{1}{2}\left[\frac{(T_* - \hat{T})^2}{\sigma_T^2} + \frac{(L_* - \hat{L})^2}{\sigma_L^2}\right]\right), \quad (1)$$

where σ_T and σ_L are the measured uncertainties (assumed to be normally distributed) associated with T_* and L_* , respectively (we implicitly assume uniform priors on the model parameters, $\{\hat{T}, \hat{L}\}$, in this calculation). A distance uncertainty of ± 20 pc is included in σ_L , added in quadrature to the nominal uncertainty (see Appendix B). The pre-MS model grids provide a direct, one-to-one mapping $\{\hat{T}, \hat{L}\} \mapsto \{M_*, t_*\}$, and therefore a corresponding mapping $\mathcal{L}(\hat{T}, \hat{L}|T_*, L_*) \mapsto \mathcal{L}(M_*, t_*|T_*, L_*)$.⁴ The marginal probability density functions $p(M_*|T_*, L_*)$ and $p(t_*|T_*, L_*)$ can then be determined through an appropriate numerical integration of $\mathcal{L}(M_*, t_*|T_*, L_*)$ over t_* and M_* , respectively. For reference, a graphical illustration of the approach is shown in Figure 4.

The method outlined above was used to determine the best-fit $\{\log M_*, \log t_*\}$ (corresponding to the peaks of the marginal distributions for each parameter) and their associated uncertainties (the marginalized 68% confidence intervals) for each individual star and each of the three pre-MS model grids. The results are compiled in Table 3. It is worth explicitly pointing out that each pre-MS model grid has boundaries, and the inferences of $\{M_*, t_*\}$ outside those boundaries should be considered highly uncertain. This is a relatively minor concern for $M_* < 0.1 M_\odot$ in the SDF00 models, but is a serious issue when $M_* > 1.4 M_\odot$ or $t_* < 1$ Myr in the BCAH98 models. Whenever relevant in the following, we are sure to highlight these extrapolated quantities.

Before moving on, it is worthwhile to comment on the stellar properties inferred for this catalog. Figure 5(a) displays the ensemble stellar mass functions, constructed by summing (and then binning) the marginal distributions, $p(M_*|T_*, L_*)$, for each individual star in the sample. The morphology is similar to previous measurements of the overall Taurus mass function (e.g., Luhman 2000, 2004; Briceño et al. 2002), although this version has the added benefit of explicitly incorporating the uncertainties for each contributing M_* estimate. Taken together, the three different pre-MS model grids predict mass functions for this sample that are generally consistent with one another. A similar approach was employed in Figure 5(b) to determine a mean age distribution for the sample, in the view of each pre-MS model grid. The BCAH98 and SDF00 models both suggest an ensemble mean age of ~ 2.5 – 3 Myr for Taurus Class II sources; the DM97 models argue for a younger age, ~ 1 Myr. This systematic offset between the isochronal ages is primarily related to the assumed initial conditions in the evolutionary model calculations (e.g., Stahler 1983; Palla & Stahler 1993), as was noted in a similar comparison of ages inferred from the DM97 and

⁴In practice, all of the analysis described here is performed on logarithmic variables to facilitate a more straightforward numerical evaluation of the likelihood grid over the wide ranges spanned by the parameters of interest. For the sake of clarity in notation, we have omitted the $\log X$ in favor of the simpler X for each variable.

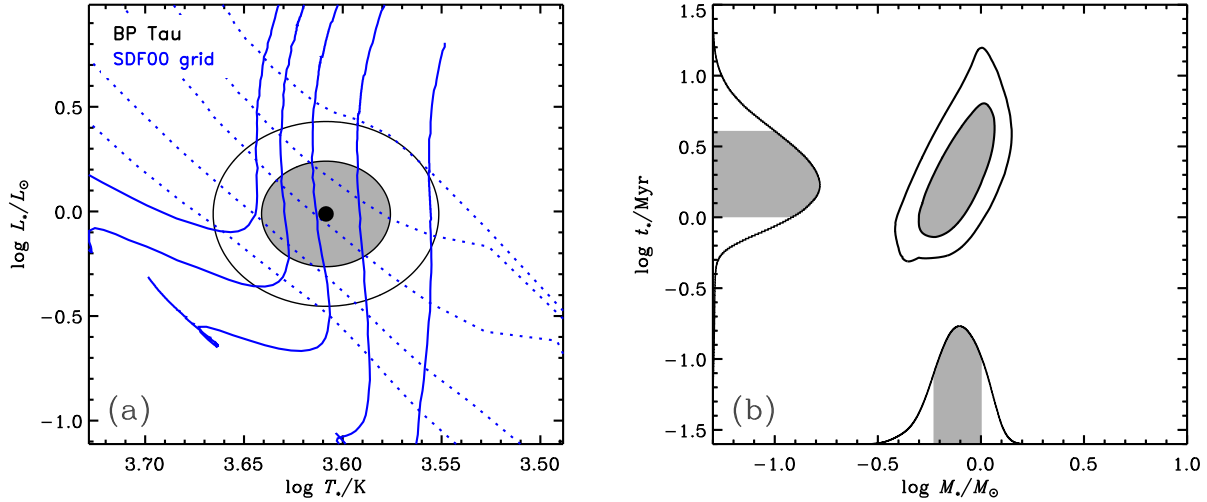


Fig. 4.— An illustration of the method used to estimate stellar masses and ages, for the case of BP Tau and the SDF00 models. (a) The local H-R diagram with the SDF00 tracks for $M_* = 0.4, 0.6, 0.8, 1.0$, and $1.2 M_\odot$ (solid curves, from right to left) and isochrones for $t_* = 0.5, 1, 2, 5$, and 10 Myr (dotted curves, from top to bottom) overlaid. The black dot represents the measured $\{\log T_*, \log L_*\}$ values, and the contours around it mark the 68 and 95% confidence intervals of the likelihood function in Eq. (1). (b) The likelihood function mapped onto $\{\log M_*, \log t_*\}$ -space. The marginal probability density functions for each parameter are shown along their respective axes. The best-fit parameters and their uncertainties listed in Table 3 are determined from the peaks of those distributions and the 68% confidence intervals (in shaded gray), respectively.

other model grids for young stars in Orion (Hillenbrand 1997). However, despite this apparent discrepancy, the widths of these mean age distributions are very large – 68% of their areas are enclosed in a range of ~ 0.2 –8 Myr – suggesting reasonable agreement overall.

Although the three different pre-MS model grids do make different predictions for the stellar properties that correspond to each location in the H-R diagram, there is generally good agreement between them within the (substantial) uncertainties inferred with this technique. We find a modest tendency for the BCAH98 models to predict higher masses: on average ~ 0.2 dex above the DM97 values and ~ 0.1 dex higher than SDF00, although the RMS dispersions in the residuals are of the same order and that progression is reversed over a narrow mass range ($M_* \approx 0.1$ – $0.2 M_\odot$). These features are manifestations of structural differences between the models, tied to the resulting \hat{T} values. Dynamical mass estimates (M_{dyn}) are available for ~ 20 sources in this sample, derived either from gas disk rotation curves (Simon et al. 2000; Dutrey et al. 2003, 2008; Piétu et al. 2007; Schaefer et al. 2009; Tang et al. 2012), radial velocity monitoring of spectroscopic binaries (plus some external inclination constraint; e.g., Mathieu et al. 1997; Prato et al. 2002), or the reconstruction of astrometric orbits for close binaries (Tamazian et al. 2002; Schaefer et al. 2006). A comparison of M_{dyn} and our estimates of M_* shows a pattern similar to the inter-model compar-

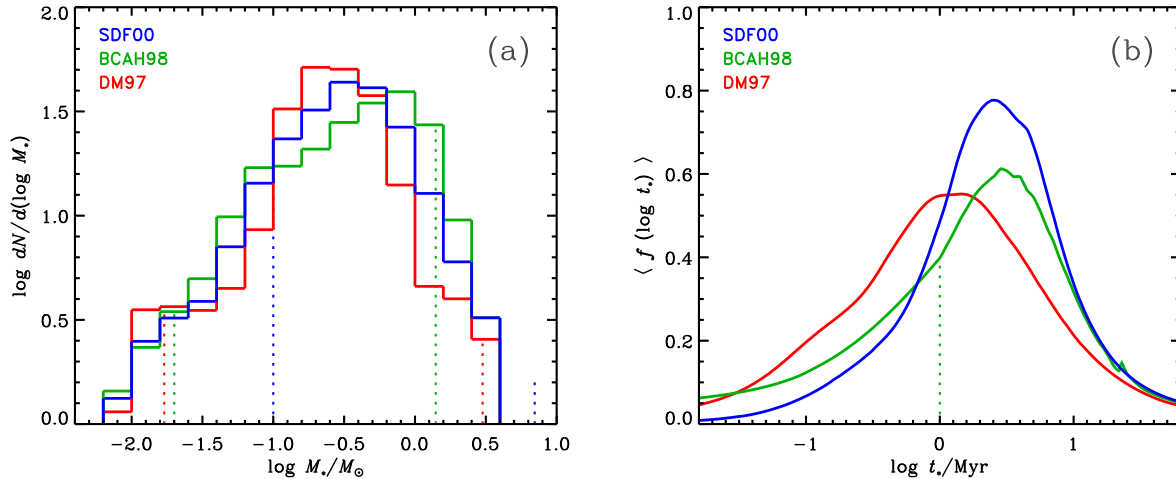


Fig. 5.— (a) The ensemble stellar mass functions for the sample, constructed by summing the marginal M_* probability density functions for individual sources and then integrating into discrete bins (thereby properly incorporating the uncertainty on each individual measurement). Dotted vertical lines mark the boundaries of each pre-MS model grid: outside those lines, the M_* values were determined from extrapolations. (b) The ensemble mean age distributions for the sample, determined by averaging the marginal t_* probability density functions for individual sources. Ages less than the green dotted line for the BCAH98 models are extrapolations.

isons: the BCAH98 models slightly over-predict M_{dyn} by ~ 0.1 dex, the SDF00 models marginally under-predict by ~ 0.05 dex, and the DM97 models under-predict by ~ 0.2 dex (the RMS dispersions of the residuals are ~ 0.1 dex). However, it is worth noting that the range of M_{dyn} measurements available for Class II Taurus sources is still biased to solar-mass (or greater) systems. Quantitatively, this level of mass disagreement is similar to what was found by Hillenbrand & White (2004) for a larger, and primarily older, sample. The stellar ages inferred here have considerably more (formal) uncertainty associated with them. Again, on an individual basis the t_* estimates from different models are consistent within the uncertainties, although the best-fit DM97 ages are systematically younger (a median shift of ~ 0.3 dex) compared to both the BCAH98 and SDF00 predictions.

3.2.2. A Statistical Comparison of M_d and M_*

Now, using the M_* values derived above (Table 3), we can make a direct mass comparison between disks and their stellar hosts. First, we consider the relationship between the observational proxy for disk mass, L_{mm} , and M_* . The plots in Figure 6 clearly indicate that the mm-wave luminosities from dust disks are highly correlated with their host star masses in the full Taurus Class II sample (210 datapoints). That visual exhibition of a strong relationship between L_{mm} and M_* is quantitatively confirmed by correlation tests adapted for use on censored datasets (Isobe et al.

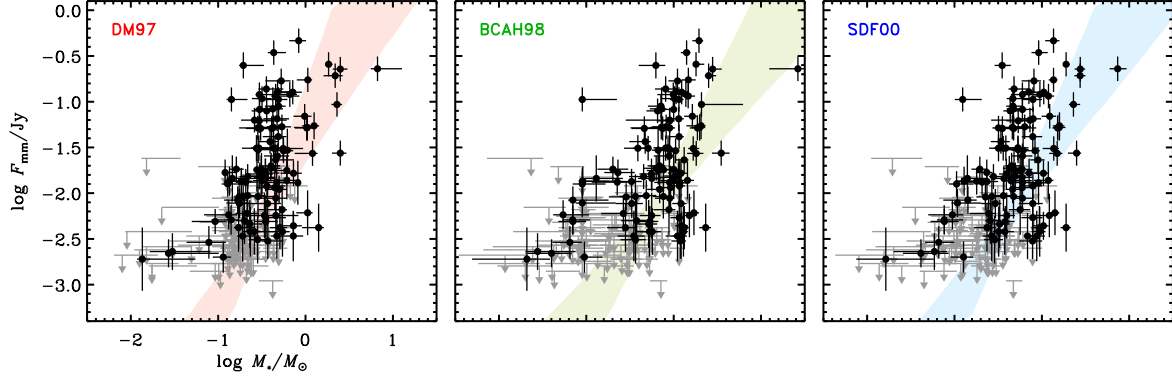


Fig. 6.— A comparison of L_{mm} and M_* for each set of pre-MS models (upper limits are shown as gray arrows). The colored swaths mark 95% confidence intervals on the $\log L_{\text{mm}} \sim \log M_*$ relationship, derived from a Bayesian linear regression analysis that accounts for censored data.

1986). The Cox proportional hazard test suggests that the null hypothesis (no correlation) has a probability $p_0 < 10^{-8}$ for each of the pre-MS models (with global χ_r^2 values of 56, 73, and 72 for DM97, BCAH98, and SDF00, respectively). Similarly stringent limits on p_0 are derived from the generalized Kendall or Spearman rank tests (with z -scores of 8.3, 9.1, and 9.1 and $\rho = 0.55, 0.61$, and 0.60 for each model grid and correlation test, respectively). Assuming an intrinsic power-law scaling between L_{mm} and M_* , this correlation is quantified with a linear regression analysis in the log-log plane, where $\log(L_{\text{mm}}/L_\odot) = A + B \log(M_*/M_\odot)$, using the Bayesian methodology developed by Kelly (2007) to properly account for the measurement uncertainties, data censoring, and substantial scatter along the correlation. The results of that analysis are presented in Figure 7, which shows the marginal posterior probability density functions for the regression intercept (A) and slope (B) for each pre-MS model grid, along with the derived standard deviation of datapoints around the regression line (this scatter is assumed to be normally distributed with mean 0) and the associated correlation coefficient. The last panel of Figure 7 affirms the strong relationship determined from the correlation tests. The 95% confidence intervals for the regression lines are shown as shaded regions for the comparisons between L_{mm} and M_* in Figure 6.

We find an intercept $A = -1.2 \pm 0.3$, -1.8 ± 0.2 , and -1.6 ± 0.2 and slope $B = 2.0 \pm 0.5$, 1.5 ± 0.4 , and 1.7 ± 0.4 for the DM97, BCAH98, and SDF00 pre-MS model grids, respectively (quoted uncertainties represent 95% confidence intervals). These fits suggest a typical 1.3 mm flux density of ~ 25 mJy for $1 M_\odot$ stars, falling to only ~ 4 mJy at the peak of the host mass function ($\sim 0.3 M_\odot$). The inferred slope (B) values indicate that L_{mm} scales rather steeply with host mass (but see below). That said, it should be obvious in Figure 6 that there is a substantial scatter around the underlying relationship that is much larger than the conservative formal uncertainties on L_{mm} or M_* can accommodate. Assuming that this scatter is described by a normal distribution (with mean 0), the Kelly (2007) regression method provides an inference of the variance of that distribution. The corresponding standard deviation is 0.7 ± 0.1 dex for all models: in short, at any given host

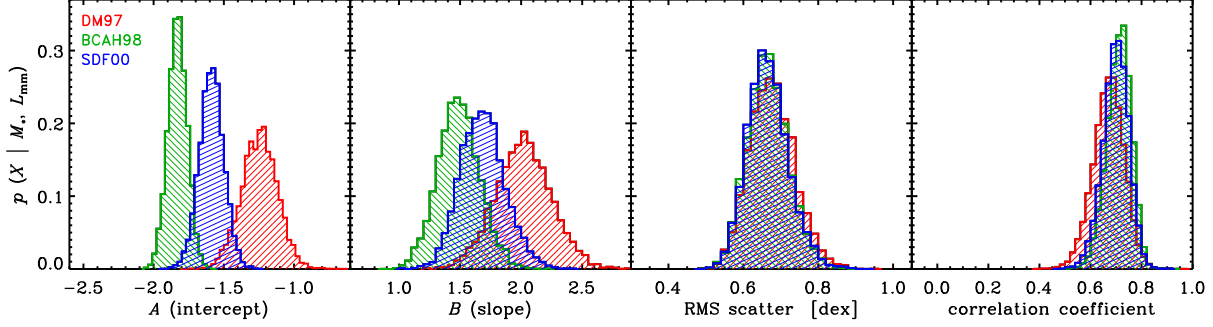


Fig. 7.— Results from a Bayesian linear regression analysis of the relationship between $\log L_{\text{mm}}$ and $\log M_*$. From left to right, the marginal posterior probability density functions for the intercept (A), slope (B), dispersion around the regression, and corresponding correlation coefficient.

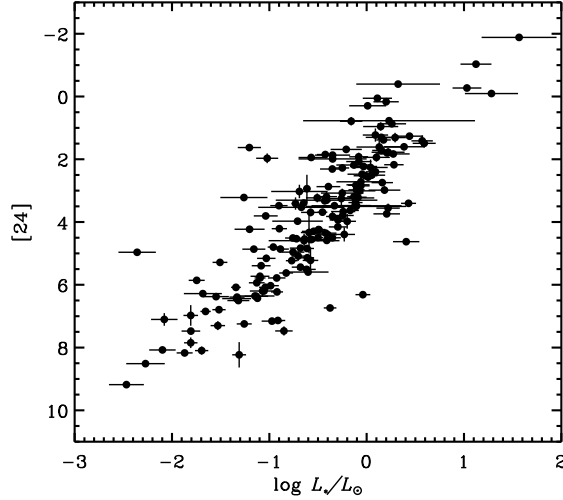


Fig. 8.— Demonstration of the strong correlation between the amount of dust emission in the mid-infrared (shown here as the *Spitzer* 24 μm apparent magnitude; Luhman et al. 2010; Rebull et al. 2010), which scales with the dust temperature $\langle T_d \rangle$, and the luminosity of the stellar host.

mass, 68% of the L_{mm} values span a factor of ~ 5 on either side of the best-fit regression line.

A disk mass can be crudely estimated from a simple scaling of the mm-wave continuum luminosity (Beckwith et al. 1990). Assuming the emitting dust is optically thin and isothermal,

$$\log M_d = \log F_\nu + 2 \log d - \log(\zeta \cdot \kappa_\nu) - \log B_\nu(\langle T_d \rangle), \quad (2)$$

where κ_ν is the dust opacity, ζ is the dust-to-gas mass ratio, and $B_\nu(\langle T_d \rangle)$ is the Planck function at the average disk temperature. For ease of comparison with other studies, we adopt the assumptions of Andrews & Williams (2005) and fix $d = 140 \text{ pc}$, $\zeta = 0.01$, and $\kappa_\nu = 2.3 \text{ cm}^2 \text{ g}^{-1}$ (at the reference wavelength of 1.3 mm). The nominal conversion to M_d advocated by Andrews & Williams (2005) assumes that $\langle T_d \rangle \approx 20 \text{ K}$ is applicable for all disks. In principle, the assumption of an average

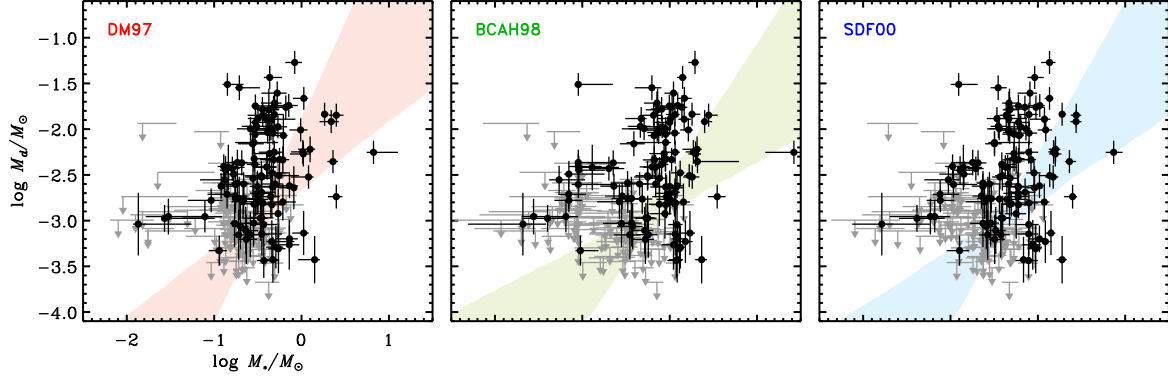


Fig. 9.— As in Fig. 6, but for M_d and M_* .

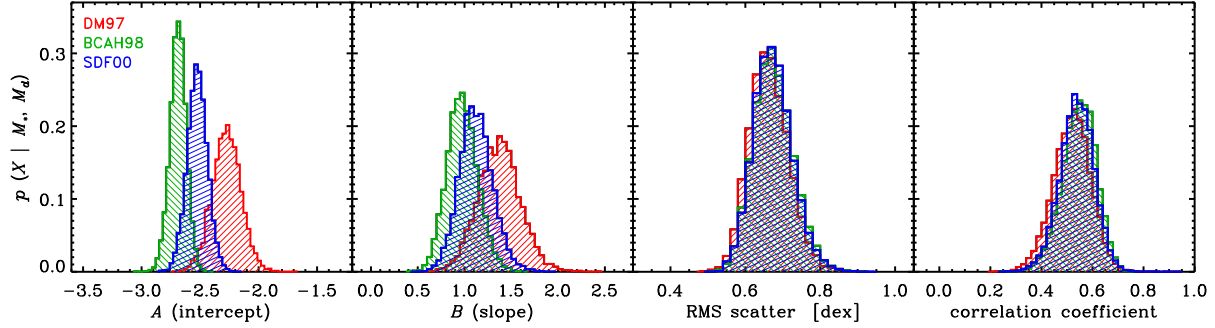


Fig. 10.— As in Fig. 7, but for M_d and M_* .

temperature in this calculation is well justified, since most of the mm-wave emission comes from cool material in the nearly isothermal outer disk (radiative transfer calculations suggest a shallow T_d profile, $\propto r^{-q}$ with $q \approx 0.4-0.6$; Chiang & Goldreich 1997; D’Alessio et al. 1998). However, there is good reason to expect that $\langle T_d \rangle$ increases with M_* . In the regions where most of the mm-wave emission is generated, the disk is heated solely by irradiation from the central star. Therefore, the local $\langle T_d \rangle$ is primarily set by L_* : all else being equal, disks around less luminous hosts should be cooler. That hypothesis has a firm empirical backing, as demonstrated in Figure 8 through the tight correlation of L_* and the *Spitzer* 24 μm emission: this mid-infrared emission is optically thick, and therefore roughly scales with $\langle T_d \rangle$. To reflect that thermal relationship, we assume a reasonable scaling $\langle T_d \rangle \approx 25(L_*/L_\odot)^{1/4}$ K (see Appendix B for L_* estimates and Appendix C for a validation of this scaling using more sophisticated radiative transfer calculations). Then, disk mass estimates (or upper limits) and uncertainties are determined from Equation 2 using the F_{mm} measurements in Table 2. As with our calculations of $\{M_*, t_*\}$, we include an additional uncertainty on M_d that accounts for an intrinsic ambiguity in the assumed distance of ± 20 pc ($\sim 15\%$).

Figure 9 shows the direct comparisons of M_d and M_* for the full catalog sample for each of the three pre-MS model grids. Again, we identify a strong correlation between these variables: the same censored statistical tests rule out the null hypothesis with similarly high confidence as

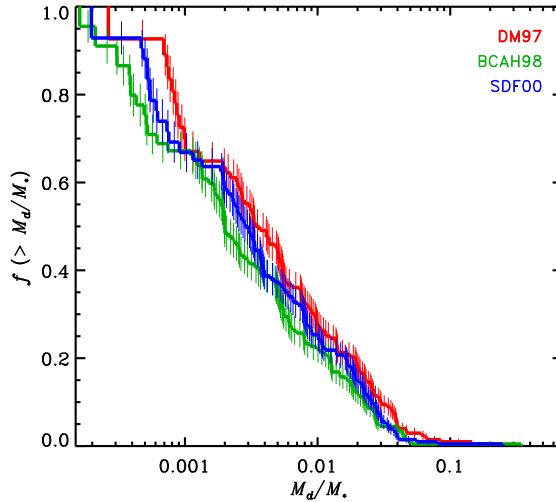


Fig. 11.— The cumulative distribution of the disk-to-star mass ratios, constructed from the Kaplan-Meier product-limit estimator to incorporate censored datapoints. The median mass ratio is $\sim 0.3\%$, the upper quartile of the distribution has $M_d/M_* \geq 1\%$: very few sources have $M_d/M_* \geq 10\%$.

for the $L_{\text{mm}} \sim M_*$ relationship. The results of a Bayesian linear regression on this correlation, where $\log(M_d/M_\odot) = A + B \log(M_*/M_\odot)$, are shown in Figure 10; the shaded regions in Figure 9 represent the 95% confidence intervals on the regression lines. We find intercepts $A = -2.3 \pm 0.3$, -2.7 ± 0.2 , and -2.5 ± 0.2 and slopes $B = 1.4 \pm 0.5$, 1.0 ± 0.4 , and 1.1 ± 0.4 for the DM97, BCAH98, and SDF00 model grids, respectively (quoted uncertainties are at the 95% confidence level). In short, this sample suggests a roughly linear scaling between disk and host star masses, $M_d \propto M_*$, with a typical disk-to-star mass ratio of $\sim 0.2\text{--}0.6\%$. For reference, the cumulative distributions of that mass ratio, $f(> M_d/M_*)$, for each pre-MS model grid are shown together in Figure 11. The intrinsic scatter measured around this correlation is the same as was inferred from the relationship between L_{mm} and M_* , with a standard deviation of 0.7 ± 0.1 dex (this corresponds to a full-width at half-maximum spread of a factor of ~ 40 in the disk masses present at any given host mass).

3.2.3. Potential Sources of Scatter and Bias

In the previous section, we demonstrated that there is a strong correlation between the measured mm-wave continuum luminosities from dust disks and the inferred masses of their stellar hosts. It is natural to associate the shape of that correlation and the scatter around it with a corresponding relationship between M_d and M_* and an intrinsic distribution of M_d at any given host mass (as was illustrated in Figs. 6–7). However, the assumption of that scaling or those made in converting L_{mm} to M_d could introduce scatter into the relationship, and might also bias the shape of the correlation derived from the regression analysis. Here, we discuss five of the key issues that might influence these results: (1) a potentially more complex intrinsic relationship between

M_d and M_* ; (2) additional dust temperature effects; (3) contamination from high optical depths; (4) assumptions about the emitting material (i.e., κ_ν); and (5) variations in evolutionary state.

The first issue is one of practical interpretation: we have implicitly assumed that the measured correlation between L_{mm} (or M_d) and M_* can be functionally represented as a power-law scaling with a single index over the full range of host masses. An intrinsic relationship that is different from the one imposed here would naturally bias our inferences of its shape and the associated scatter around it. Although the current survey data do not necessarily warrant a more complex prescription to parameterize these relationships, they by no means rule out such a scenario either. For example, bimodal or logistic functions might describe the correlations in Figures 6 and 9 equally well, and could perhaps be characterized by less intrinsic scatter/outliers. With the currently available data, the regression analysis is (rightfully) focused on the many low- M_* targets that tend to have faint mm-wave emission, or, more commonly, upper limits on L_{mm} or M_d . A more sensitive survey of this population that provides robust mm-wave continuum detections (or much deeper upper limits) should be able to discriminate between these (or other) alternatives.

The nominal conversion to M_d used above assumes a simple relationship between the host luminosity and the average dust temperature is applicable for all disks in the sample. That relationship implies that the slope of the correlation between M_d and M_* is substantially less steep than would be inferred from the normal assumption of a single $\langle T_d \rangle$ value (which is identical to the $L_{\text{mm}} \sim M_*$ relationship represented in Figs. 6 and 7). Through this $\langle T_d \rangle$ correction, the intrinsic L_* scatter in the H-R diagram (see Appendix B) contributes a dispersion of $\lesssim 0.2$ dex in the $\{M_d, M_*\}$ -plane, significantly less than what was measured in §3.2.2 (0.7 dex). However, this $\langle T_d \rangle$ prescription only considers the source of irradiation energy, and not the (possibly related) efficiency at which the disk absorbs (thermalizes) it. The latter is partly set by the surface area of the disk that intercepts starlight, as determined by the vertical distribution of small dust grains in the disk atmosphere. If those grains are coupled to a gas phase in hydrostatic equilibrium, the dust height varies like $H \propto (\langle T_d \rangle / M_*)^{0.5}$. In this sample, $L_* \propto M_*^{1.5-2}$, implying that H is relatively independent of M_* (given the scaling between $\langle T_d \rangle$ and L_* advocated above). In reality, the scaling between H , $\langle T_d \rangle$, and M_* depends more intimately on the detailed coupling between the gas and small grains. Unfortunately, the processes that control dust sedimentation and their impact on midplane temperatures are quite complicated (e.g., Dullemond & Dominik 2004; D’Alessio et al. 2006). The diverse SED morphologies for disks (see Appendix A) suggest that dust settling probably represents an important contribution to the scatter in the relationship between M_d and M_* (of uncertain magnitude), but there is no indication that it should preferentially bias its slope.

The fundamental assumption in Eq. (2) is that the mm-wave continuum emission is optically thin. For a reasonable range of grain properties, this is a valid assumption for most disks (e.g., Beckwith et al. 1990). Based on a fiducial model of disk structure, Andrews & Williams (2005) suggested that $\gtrsim 90\%$ of the total mm-wave luminosity is optically thin, although that fraction likely decreases for the brightest (most massive) sources. Subsequent high angular resolution work has demonstrated that brighter disks tend to be more spatially extended, suggesting that most

of their emission is generated from low column densities in the outer disk (Andrews et al. 2010). Moreover, recent multi-wavelength observations of disks suggest that optical depths remain low even for the high column densities expected at small disk radii, due to the natural decrease in particle emissivities produced by dust grain growth (e.g., Guilloteau et al. 2011; Pérez et al. 2012). Given these resolved constraints, and since the under-estimate of M_d induced by optically thick contamination is expected to be quite small in any case ($\lesssim 0.05$ dex), it is clear that the assumption of optically thin emission made in Eq. (2) has negligible influence on the shape of the correlation between M_d and M_* or the scatter around its corresponding best-fit regression lines.

The impact of the material properties of disks in the $\{M_d, M_*\}$ -plane – encapsulated here in the grain opacity, κ_ν , and dust-to-gas mass ratio, ζ – are considerably more difficult to predict generically. Particle growth promotes a net decrease in the disk-averaged κ_ν , while particle migration (dominated by radial drift; Weidenschilling 1977) effectively decreases ζ over most of the disk volume (e.g., Takeuchi & Lin 2002; Brauer et al. 2008; Birnstiel et al. 2010). Models of this material evolution predict that growth timescales increase like $1/\zeta\sqrt{M_*}$ up to grain sizes (a) that are limited by fragmentation ($a_{\max} \propto M_d$; Birnstiel et al. 2011) or drift ($a_{\max} \propto M_*M_d\zeta$; Birnstiel et al. 2012). If all else is equal, the disks around more massive stellar hosts would have more top-heavy particle size distributions and (if $a_{\max} \gtrsim \lambda$) therefore lower κ_ν on average (this effect would be amplified by an underlying relationship between M_d and M_*). Considering our assumptions in Eq. (2), this would imprint a negative bias on the regression slope inferred in §3.2.2: the true value of B might be larger than suggested. However, some caution in the generic interpretation of these models is warranted. The quantitative effects of other parameters (including turbulence, ζ , temperature, etc.) and how they mutually interact and scale with M_* might dominate the model behavior. In principle, the *sense* of any bias can be determined empirically by examining how the slope of the mm/radio-wave spectrum (which is related to κ_ν ; e.g., Beckwith & Sargent 1991) depends on M_* . In terms of the scatter in the relationship between M_d and M_* , the natural dispersions in κ_ν and ζ would seem perfectly reasonable explanations. For example, an RMS scatter of an order of magnitude in a_{\max} and a factor of ~ 2 in ζ can account for the measured dispersion.

Aside from these effects of material evolution, the global viscous evolution of disk structures more generally might be expected to imprint some feature on the observed relationship between M_d and M_* . In the standard model for viscous evolution, disk masses decay at a rate $M_d \propto (t_*/t_s)^{-1/2}$, where t_s is the viscous timescale (Hartmann et al. 1998). In this scenario, a correlation between disk and host masses could be imposed at the formation epoch, or could be produced naturally if t_s scales with M_* and/or t_* scales inversely with M_* . There is no evidence for the latter; indeed, if anything, young clusters tend to exhibit preferentially older ages among their early-type members (e.g., see Pecaute et al. 2012). Formally, $t_s \propto \sqrt{M_*}/\langle T_d \rangle$, which implies a negligible contribution to an intrinsic scaling between M_d and M_* (although a relationship between either M_d or M_* and the level of disk turbulence might imprint a feature). In essence, there is no obvious reason to assume that viscous evolution significantly biases the observed correlation. Moreover, we find no evidence whatsoever for a relationship between M_d and t_* in this sample. Given the large uncertainties on

the latter, this is not such a surprise: in §3.2.1 we argued that there is no firm statistical evidence for an age gradient larger than ± 0.7 dex in this sample. Nevertheless, the permitted dispersion in t_* is roughly sufficient to explain the measured scatter around the $M_d \propto M_*$ regression lines.

4. Discussion

We have significantly expanded the mm-wave photometry catalog of circumstellar disks in the Taurus star-forming region, using “snapshot” continuum observations of ~ 60 new sources with the SMA. Folding these new disks, most of which have M-type stellar hosts, in with survey results in the literature, we have constructed a $\lambda = 1.3$ mm luminosity census that is *complete* for the known Class II members in Taurus with spectral types earlier than M8.5 (cf., Luhman et al. 2010), down to a ($3\text{-}\sigma$) sensitivity limit of ~ 3 mJy (corresponding to a disk mass limit of ~ 0.1 to $1 M_{\text{Jup}}$ for A- or M-type hosts, respectively, following the assumptions outlined in §3.2.2). The derived luminosity distribution is found to be substantially different than in previous work, with a notable shift to weaker emission that was identified through a more robust understanding of individual disks in multiple systems (facilitated by Harris et al. 2012) and the incorporation of a large subset of previously un-observed faint disks that are preferentially hosted by low-mass stars and brown dwarfs. Having remedied the selection bias of the original Andrews & Williams (2005) survey against these late-type members, we uncovered a strong correlation between the mm-wave luminosities emitted by dust disks and the spectral types (effective temperatures) of their hosts.

A Bayesian estimation technique developed by Jørgensen & Lindegren (2005) has been used to convert the location of each individual host star in the H-R diagram into a corresponding mass and age, with reference to three representative grids of pre-MS evolution models (D’Antona & Mazzitelli 1997; Baraffe et al. 1998; Siess et al. 2000). The results are used to demonstrate that the mm-wave dust continuum luminosity – a proxy for the disk mass, through a simple scaling relation – is strongly correlated with the mass (but not age) of its host, regardless of which pre-MS model grid is assumed. A linear regression analysis in the (logarithmic) $\{M_d, M_*\}$ -plane, conducted with the maximum likelihood estimator derived by Kelly (2007) to properly account for measurement error, data censoring, and intrinsic scatter, favors a roughly linear scaling, $M_d \propto M_*$, with a typical disk-to-host mass ratio of $\sim 0.2\text{--}0.6\%$. Although the statistical evidence for this relationship is robust, its physical origins remain unclear: it may be a manifestation of the initial conditions imposed at disk formation, and/or a consequence of the combined effects from various evolutionary mechanisms that depend on the host mass. Regardless, these results indicate that the host mass plays a fundamental factor in setting M_d , with an influence that is roughly equivalent to the presence of a close stellar companion (e.g., Jensen et al. 1994, 1996; Harris et al. 2012).

There is substantial scatter around the correlation between M_d and M_* , which reflects the net effects of the intrinsic distributions of masses, temperatures, opacities, and evolutionary states in the sample. Assuming this dispersion is characterized by a normal distribution in the regression analysis, we measure a standard deviation of 0.7 dex (a factor of ~ 5 on either side of the scaling

between M_d and M_*). For a relationship that spans only ~ 3 dex in each variable, this scatter is large in an absolute sense. However, considering the substantial uncertainties we have regarding the physical processes that play important roles in setting L_{mm} – particularly related to the material evolution of dust particles – it is remarkable that the scatter is limited enough that a correlation can be identified at all. These results suggest that the product of mm-wave dust opacities, disk masses, and temperatures has an intrinsic FWHM of a factor of ~ 40 for any given M_* .

Improved constraints on the basic morphology of the relationship between M_d and M_* will require a substantially more sensitive mm-wave photometry survey for M-type hosts. For example, a census that probes $10\times$ deeper than the data presented here (a relatively trivial time investment for ALMA) should be able to differentiate between the power-law scaling we have assumed and more dramatic alternatives (i.e., a precipitous drop in the mass scaling). Moreover, a multi-wavelength photometry census (preferably a long-wavelength complement to the catalog provided here) of the full Taurus sample is crucial, since it can provide fundamental constraints on the contribution of material evolution in these disks to the intrinsic scatter in the observed $M_d \propto M_*$ correlation.

4.1. Implications for Planet Formation Models

Although the analysis presented here represents the first statistically robust confirmation and characterization of a correlation between M_d and M_* , it is by no means the first to suggest that such a relationship exists. With a sample that was biased against hosts that span the lowest available M_* decade and had a naturally sparse population at high M_* , Andrews & Williams (2005) found no evidence for the relationship inferred here (see their Fig. 9). Some hints of a correlation have been tentatively noted when a larger (inhomogeneous) sample of Herbig AeBe stars is considered (e.g., Natta et al. 2000; Williams & Cieza 2011).⁵ As others started to measure mm-wave luminosities from the disks around later type hosts, low detection rates and faint emission suggested a potential trend: Scholz et al. (2006) indicated that the disks around brown dwarf hosts are intrinsically low-mass (see also Klein et al. 2003), and Schaefer et al. (2009) argued that hosts with spectral type later than M2 had systematically less mm-wave emission than their counterparts with earlier types. However, there was a legitimate concern that the large population of M-type hosts that had *not* yet been observed might exhibit a different behavior than these limited subsamples.

Despite the previous (and justified) reticence of the observational community, an implicit linear scaling $M_d \propto M_*$ is pervasive in theoretical studies of planet formation. The concept of such a scaling seems so natural in a gravitational sense that a physical basis for this foundational assumption is rarely offered in the literature. Given the lingering uncertainties on the nature of disk formation and early evolution (and how those processes might depend on a changing M_*), there

⁵It is worth noting that both of these review articles ignored star-disk systems that did not have firm mm-wave *detections*, which was presumably part of the reason that they chose not to invest in a more involved correlation analysis or make any strong claims on the validity or characteristics of a relationship between M_d and M_* .

was good reason to question that assumption. However, the results we have presented here now provide a firm empirical validation of the physical intuition behind it, thereby supporting some key conclusions inferred from planet formation theories that use disk properties as initial conditions.

In both the core accretion (Pollack et al. 1996) and disk instability (Boss 1997) models, the overall efficiency of the giant planet formation process scales with the amount of mass available in the disk. For the disk instability case, this is more of a threshold effect: regardless of the host mass, the potential for disk fragmentation and gaseous protoplanet formation is enhanced if M_d/M_* is sufficiently large (e.g., Boss 2006; Durisen et al. 2007). However, our characterization of the $M_d \propto M_*$ scaling indicates that the disk-to-star mass ratio is basically independent of M_* . Taking that as an initial condition, the disk instability model would predict a roughly constant gas giant planet fraction across the stellar mass distribution.⁶ On the other hand, the efficiency of the core accretion model depends on a key timescale: a sufficiently massive solid core must be assembled before the gas disk dissipates. This core growth is accelerated for disks with higher densities ($\propto M_d$; e.g., Ikoma et al. 2000; Hubickyj et al. 2005; Thommes et al. 2008), and sees modest benefits from shorter orbital periods ($\propto \sqrt{M_*}$ at a fixed semimajor axis) and larger potential formation zones ($\sim M_*$; e.g., Kennedy & Kenyon 2008). In this case, the intrinsic $M_d \propto M_*$ correlation found here implies that planet formation is inherently more likely around more massive stellar hosts (e.g., Laughlin et al. 2004; Ida & Lin 2005; Kennedy & Kenyon 2008; Alibert et al. 2011).

The observational demographics of the exoplanet population strongly support this latter core accretion scenario: the incidence of giant planets orbiting <2.5 AU from their hosts scales roughly linearly with M_* (e.g., Johnson et al. 2007, 2010; Bowler et al. 2010). This relationship between stars and their planets not only fortifies the case for core accretion as the dominant pathway for giant planet formation, it also should be recognized as a clear manifestation of the initial association between the masses of young stars and their disks during the epoch of planet formation.

4.2. Practical Consequences for Disk Evolution Studies

From a more practical standpoint, we stressed in §1 that a proper accounting of selection biases is a fundamental requirement for comparative studies of disk evolution. Previous work has suggested that disks in Orion (Mann & Williams 2010), IC 348 (Lee et al. 2011), and Upper Sco (Mathews et al. 2012) have systematically lower masses compared to Taurus (Andrews & Williams 2005) and Ophiuchus (Andrews & Williams 2007a), presumably due to evolutionary effects related to their environment, particle growth, and disk dispersal, respectively. However, these studies all relied on comparisons between incomplete samples with (usually unknown) selection biases. Now that we have constructed a complete “reference” sample for Taurus disks and identified an

⁶Note that the incidence of systems where disk instability is thought to operate, those with $M_d/M_* \gtrsim 0.1$, is very small in this sample: $<5\%$ (see Fig. 11). Since M_d estimates are likely to be under-estimated, the giant planet frequency expected from this model could reasonably be scaled up by a factor of a few (see §3.2.3 for more details).

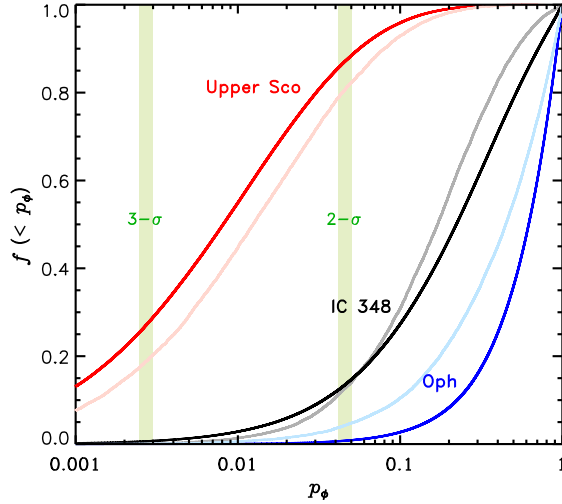


Fig. 12.— The cumulative distributions of null hypothesis probabilities, p_\emptyset – the probability that an incomplete comparison sample of mm-wave luminosities is drawn from the same parent distribution as the Taurus reference sample – constructed from two-sample tests for censored datasets in Monte Carlo simulations designed to account for selection biases related to multiplicity and host classification. The lighter curves include the effects of L_{mm} uncertainties, using random draws from a normal distribution with mean L_{mm} and variance σ_L^2 for individual sources in each sample. For reference, we mark the nominal 2- σ and 3- σ probabilities that the two samples are different.

important trend between the mm-wave luminosity ($\propto M_d$) and the stellar host type ($\sim M_*$) that could introduce strong selection effects in the comparison samples, it is imperative to re-evaluate these claimed signatures of disk evolution in a more robust statistical framework.

To properly compare the mm-wave luminosity distribution of an incomplete (potentially biased) sample from an arbitrary young cluster with the complete, reference sample derived here for Taurus, we must assume that both samples have the same intrinsic stellar mass function and multiplicity demographics. Under those assumptions, a straightforward Monte Carlo simulation can be used to statistically compare the samples. First, a trial reference sample of mm-wave luminosities is randomly drawn from the complete Taurus survey for a subset of sources that have the same distribution of host spectral types as the comparison sample. In that random selection, multiplicity selection effects can be incorporated by treating close pairs as composite systems that are assigned the spectral type of the primary (as would be inferred with observations at any given resolution). Next, the probability that these two subsamples are drawn from the same parent distribution, p_\emptyset , is evaluated using the standard suite of two-sample tests for censored datasets (e.g., Feigelson & Nelson 1985). Then, that process is repeated for a large number ($\sim 10^6$) of individual trials, and the results are used to construct a cumulative distribution of null hypothesis probabilities, $f(< p_\emptyset)$.

This technique was applied to the incomplete comparison samples of the Class II disks cata-

logged in Ophiuchus (Andrews & Williams 2007a), IC 348 (Lee et al. 2011; Espaillat et al. 2012), and Upper Sco (Mathews et al. 2012), with reference to the Taurus sample provided here (in computing luminosities, we adopt distances of 125, 350, and 145 pc, respectively, for the comparison samples).⁷ The resulting cumulative distribution functions, $f(< p_\theta)$, constructed from the Peto-Prentice test are shown in Figure 12 (the Gehan and logrank tests give similar results). Vertical green bars denote the $p_\theta = 0.0455$ and 0.0027 levels, which correspond to the nominal “2- σ ” and “3- σ ” probabilities, respectively, that the two samples being compared are different.

The cumulative distributions in Figure 12 indicate that the incomplete Ophiuchus and IC 348 samples have mm-wave luminosity distributions that are statistically indistinguishable from the Taurus reference sample compiled here, while the Upper Sco sample appears to have marginally ($\sim 2.5\text{-}\sigma$) different (in this case lower) luminosities on average. For Ophiuchus and Upper Sco, these results are in good agreement with the original analyses of Andrews & Williams (2007a) and Mathews et al. (2012) – although the latter case does not quite represent as striking a difference as originally suggested, primarily due to the limited size (only 20 Class II disks) of the comparison sample. In contrast, Lee et al. (2011) claimed that the IC 348 disks have a mm-wave luminosity distribution that is significantly shifted to values $\sim 20\times$ lower than its Taurus counterparts. Those results are not borne out by our analysis, which only finds a $<2\text{-}\sigma$ difference between the samples in $>85\%$ of the Monte Carlo trials and suggests a much smaller L_{mm} shift between the two samples (only $\sim 30\%$ on average). This discrepancy is due solely to selection effects in the IC 348 sample: most of the Lee et al. (2011) disk targets have mid/late M-type hosts, and we have demonstrated that such targets are systematically weaker mm-wave sources in the Taurus reference sample. When this host selection bias is taken into account, there is no available evidence for evolution in the mm-wave luminosity distribution between the Taurus and IC 348 samples.

5. Summary

We have used a “snapshot” $\lambda = 1.3$ mm survey with the SMA to obtain mm-wave photometry measurements of the continuum emission from protoplanetary dust disks, primarily around M-type hosts, for 60 previously un-observed targets in the Taurus star-forming region. By combining these new results with previous measurements in the literature, we constructed a mm-wave continuum luminosity census for the Taurus region that is statistically complete for Class II disks for hosts with spectral types earlier than M8.5, with a ($3\text{-}\sigma$) depth of approximately 3 mJy. This L_{mm} catalog was then used to explore the potential mass relationship between dust disks and their stellar hosts. The key conclusions that were drawn from the analysis of these data include:

⁷The Orion sample compiled by Mann & Williams (2010) lacks a sufficient number of hosts with firm spectral classifications to make a meaningful comparison. Nevertheless, the key environmental effect noted in that work – a systematic decrease in mm-wave luminosities for hosts near OB stars – is independent of host properties.

- There is a strong correlation between the mm-wave luminosities from dust disks and the spectral types (or effective temperatures) of their stellar hosts. Employing the Jørgensen & Lindegren (2005) method for estimating stellar masses and ages from the behavior of pre-main sequence model grids in the H-R diagram, we found that this correlation corresponds to $L_{\text{mm}} \propto M_*^{1.5-2.0}$, with a typical 1.3 mm flux density of $\sim 25 (d/140\text{pc})^{-2} \text{ mJy}$ for a $1 M_\odot$ stellar host. The steepness of that relationship should be an important consideration in the planning for future mm-wave continuum surveys of disks in other young clusters.
- Assuming a reasonable scaling of the dust temperature with host luminosity (where $\langle T_d \rangle \propto L_*^{1/4}$), we associated the correlation between L_{mm} and spectral type with an intrinsic, roughly linear, scaling between the disk and host masses, $M_d \propto M_*$. The typical disk-to-star mass ratio is $\sim 0.2\text{--}0.6\%$. There is a large dispersion around this correlation – ~ 0.7 dex, corresponding to a FWHM range of a factor of ~ 40 in M_d at any given M_* – contributed by the inherent diversity in temperatures, dust opacities, and evolutionary states in the Taurus sample.
- After considering the predictions from planet formation models, we suggested that the linear correlation between M_d and M_* determined here likely represents the origin of the correlation between the giant planet frequency and host mass that has been identified in the exoplanet population. This fundamental demographic association between stellar hosts and both the initial conditions (disks) and final outcomes (exoplanets) of the planet formation process provides strong, albeit circumstantial, support for the theoretical “core accretion” model.
- Finally, we urged caution in the comparative analysis of incomplete, potentially biased, mm-wave luminosity samples with the goal of placing constraints on disk evolution mechanisms. We used a set of Monte Carlo simulations with two-sample tests designed for censored datasets to demonstrate that a selection bias *toward* late-type hosts, and not dust evolution, is most likely responsible for the perceived difference in $f(L_{\text{mm}})$ between the IC 348 and Taurus Class II disk populations. In the future, such comparisons should rely on this kind of statistical analysis when comparing potentially biased sub-samples, while striving to assemble complete samples that ideally have well-characterized selection effects.

We are very grateful to Rahul Shetty and Brandon Kelly for their invaluable advice on a Bayesian approach to linear regression analysis, to Jonathan Williams for providing the full set of mm-wave measurements for IC 348 members, and to Til Birnstiel and Anaëlle Maury for helpful comments and critiques. We also would like to thank the referee for a prompt and constructive review that helped fortify the presentation of our key conclusions. ALK was supported by a Clay Fellowship from the Harvard-Smithsonian Center for Astrophysics. The SMA is a joint project between the Smithsonian Astrophysical Observatory and the Academia Sinica Institute of Astronomy and Astrophysics and is funded by the Smithsonian Institution and the Academia Sinica. The research involved in this article has made extensive use of the SIMBAD database, operated at CDS, Strasbourg, France and the NASA/IPAC Infrared Science Archive, which is operated by the

Jet Propulsion Laboratory, California Institute of Technology, under contract with the National Aeronautics and Space Administration.

A. Spectral Energy Distributions

In our efforts to determine some key observable stellar parameters (see Appendix B) and place the mm-wave measurements presented here in an appropriate context, we assembled a broadband reference SED for each system in this sample, using measurements available in the literature. Those SEDs are made available for each individual source in a simple electronic ASCII format (an associated `readme` file explains the columns in each table), and are displayed together in Figure 13.

Optical photometry measurements were collated from monitoring surveys (Bastian & Mundt 1979; Rydgren 1984; Vrba et al. 1986, 1989, 1993; Walker 1987; Bouvier et al. 1988, 1993, 1995; Herbst et al. 1994; Herbst & Shevchenko 1999; Petrov et al. 1999; Oudmaijer et al. 2001; Grankin et al. 2007, 2008), smaller compilations for individual targets (Rydgren & Vrba 1983; Myers et al. 1987; Gregorio-Hetem et al. 1992; Hartigan et al. 1994; Strom & Strom 1994; Kenyon & Hartmann 1995; Torres et al. 1995; Duchêne et al. 1999; White & Ghez 2001; de Winter et al. 2001; Briceño et al. 2002; Vieira et al. 2003; Beskrovnaya & Pogodin 2004; Luhman 2004; Kraus et al. 2006; Guieu et al. 2006; Audard et al. 2007; Herczeg & Hillenbrand 2008; Luhman et al. 2009b; Duchêne et al. 2010), as well as the Sloan Digital Sky Survey (SDSS–8; Adelman-McCarthy & et al. 2011) and the Carlsberg Meridian Catalog (CMC14; Evans et al. 2002). All *UBVRI* or *u'g'r'i'z'* measurements were converted to the Johnson-Cousins (Bessell 1979) or SDSS (Fukugita et al. 1996) photometric systems, respectively. Near-infrared data was compiled primarily from the Two Micron All-Sky Survey point source catalog (2MASS; Skrutskie et al. 2006), and supplemented with other data as appropriate (Kenyon et al. 1994; Kenyon & Hartmann 1995; Malfait et al. 1998; Eiroa et al. 2001, 2002; Woitas et al. 2001; White & Ghez 2001; Kraus & Hillenbrand 2007; Konopacky et al. 2007; Duchêne et al. 2010; McCabe et al. 2011; Dahm & Lyke 2011; Schaefer et al. 2012). All *JHK* measurements were transformed to the 2MASS–*JHK_s* photometric system (Carpenter 2001).

Each datapoint in the optical/near-infrared SED is associated with a measurement error in the flux density (or magnitude), σ_m , and a systematic calibration error, $\sigma_s \approx f \cdot F_\nu$ (where f usually reflects the fractional uncertainty in the filter zero-point, magnitude system conversions, etc.; for the wavelengths of interest here, f is small, $\sim 2\text{--}5\%$). However, T Tauri stars are also known (indeed partially *defined*) to be variable, which naturally increases the scatter in the SED to levels that are typically larger than these formal observational uncertainties. Unfortunately, simultaneous observations at a range of wavelengths sufficient to robustly determine the stellar parameters of interest at each epoch are practically non-existent. Nevertheless, the scatter induced by variability can be accomodated by treating it as an additional error term, even if we are ignorant of its origins or cadence. Of the Taurus Class II members in this sample, ~ 40 have a large number of independent optical measurements that we use to construct a composite distribution of magnitudes (m) at each

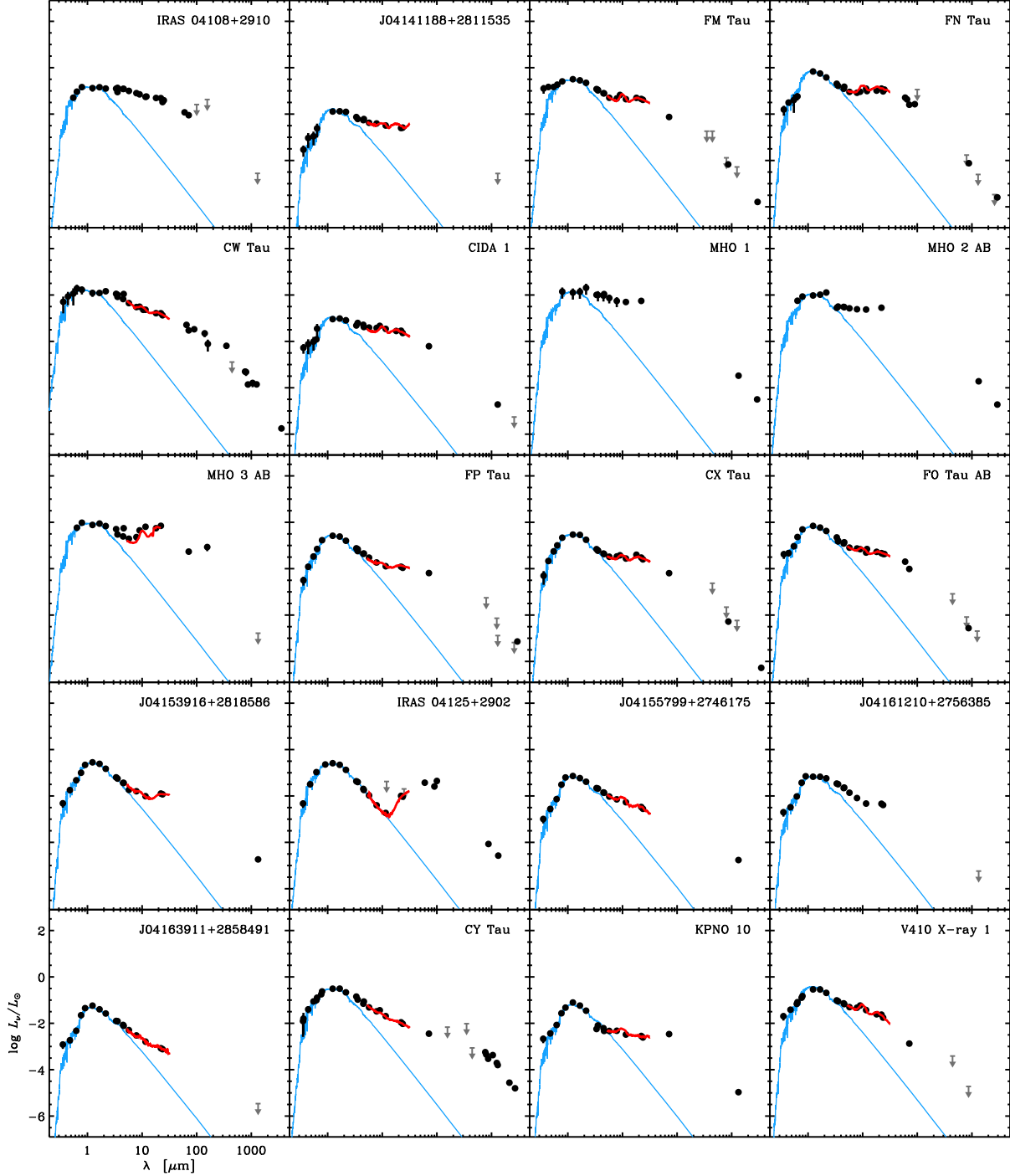


Fig. 13a.— Spectral energy distributions for the 179 Class II systems in Taurus that have mm-wave photometry measurements (note the ordinate axis is $L_\nu = 4\pi d^2 \nu F_\nu$ in L_\odot units). Each SED has been de-reddened based on the best-fit A_V values listed below in Table 4. Upper limits are shown as grey arrows (at the $3\text{-}\sigma$ level). Blue curves represent the best-fit stellar photosphere model (or composite for multiple systems); see Appendix B for details on the modeling process. Red curves mark the *Spitzer* IRS spectra that are available from the Infrared Science Archive.

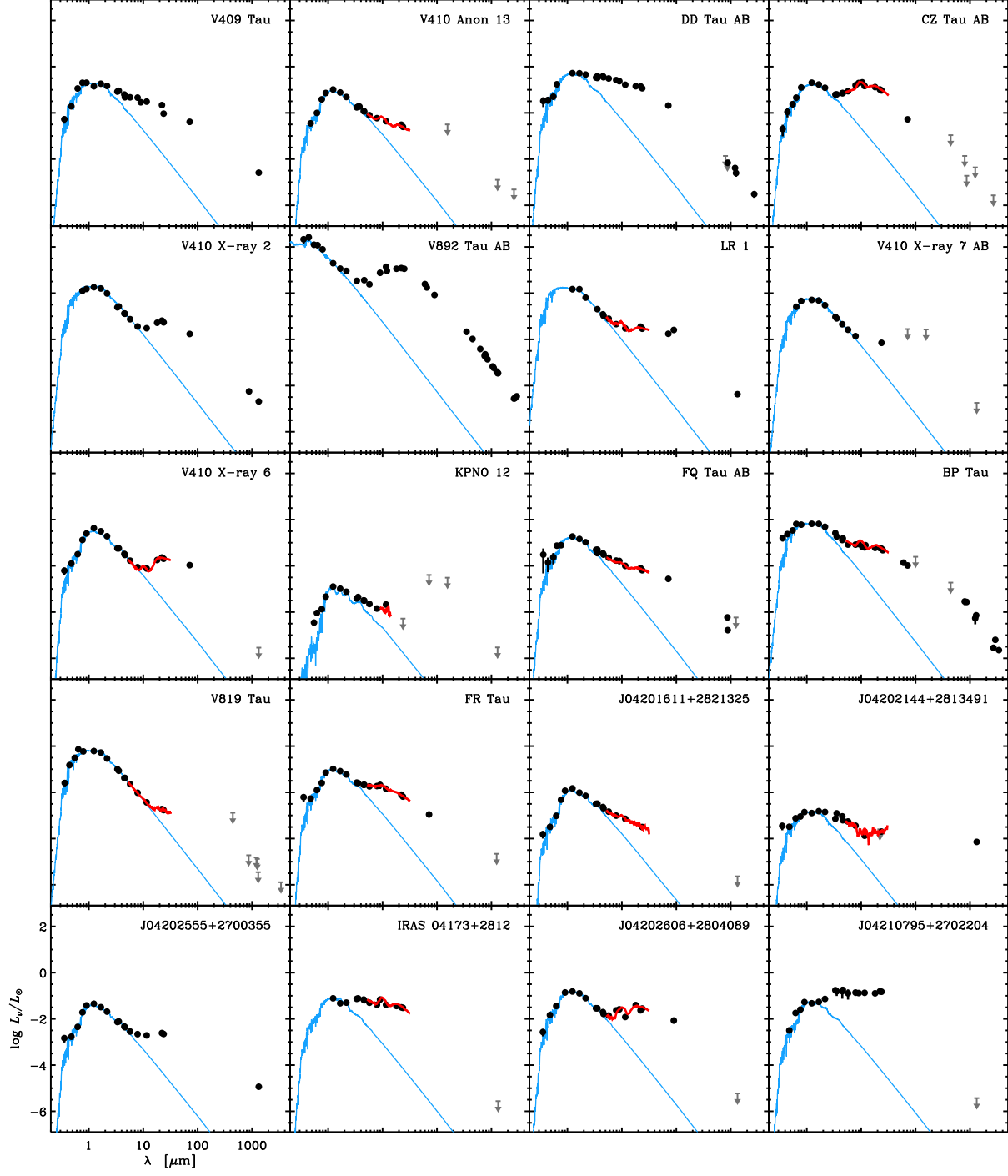


Fig. 13b.— As in panel (a).

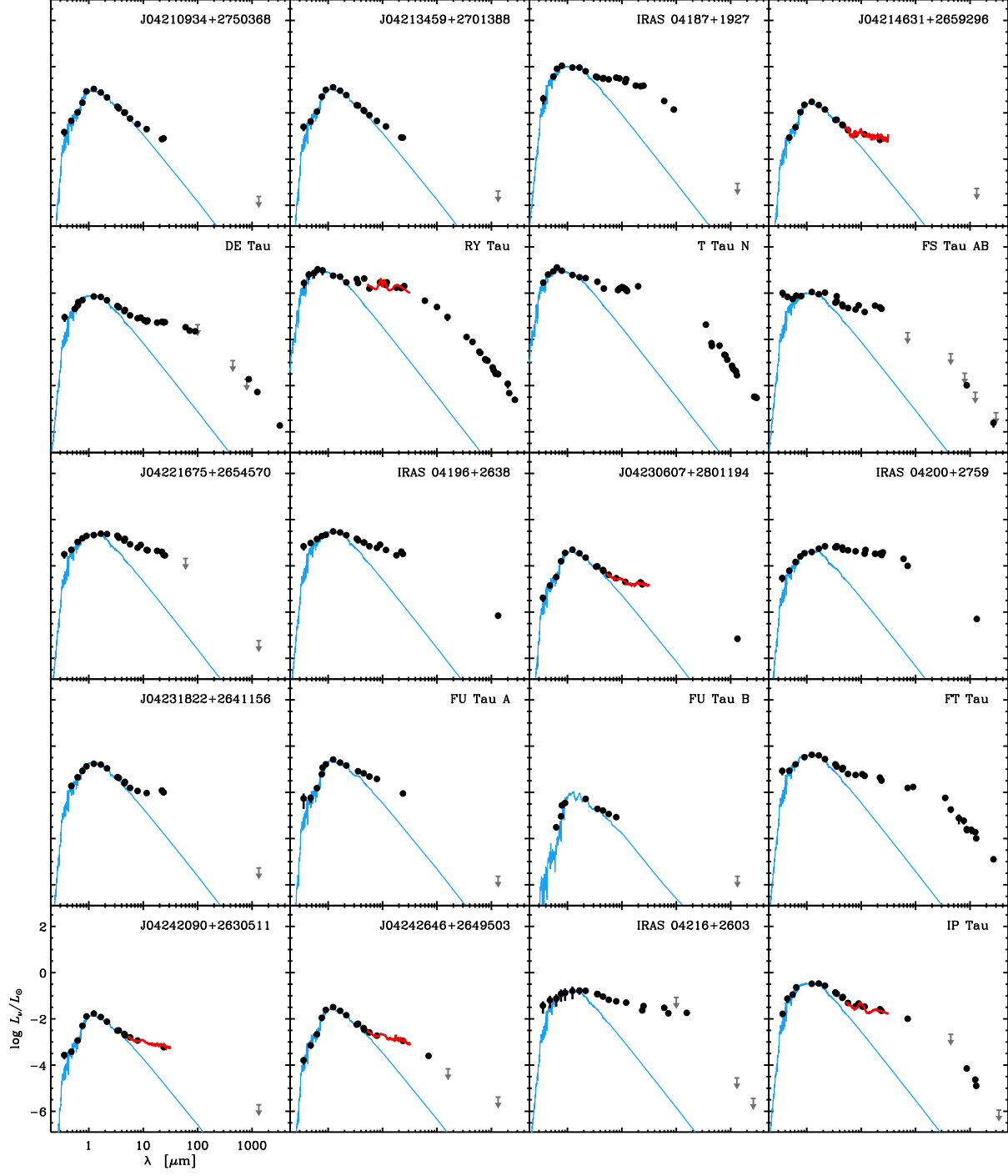


Fig. 13c.— As in panel (a).

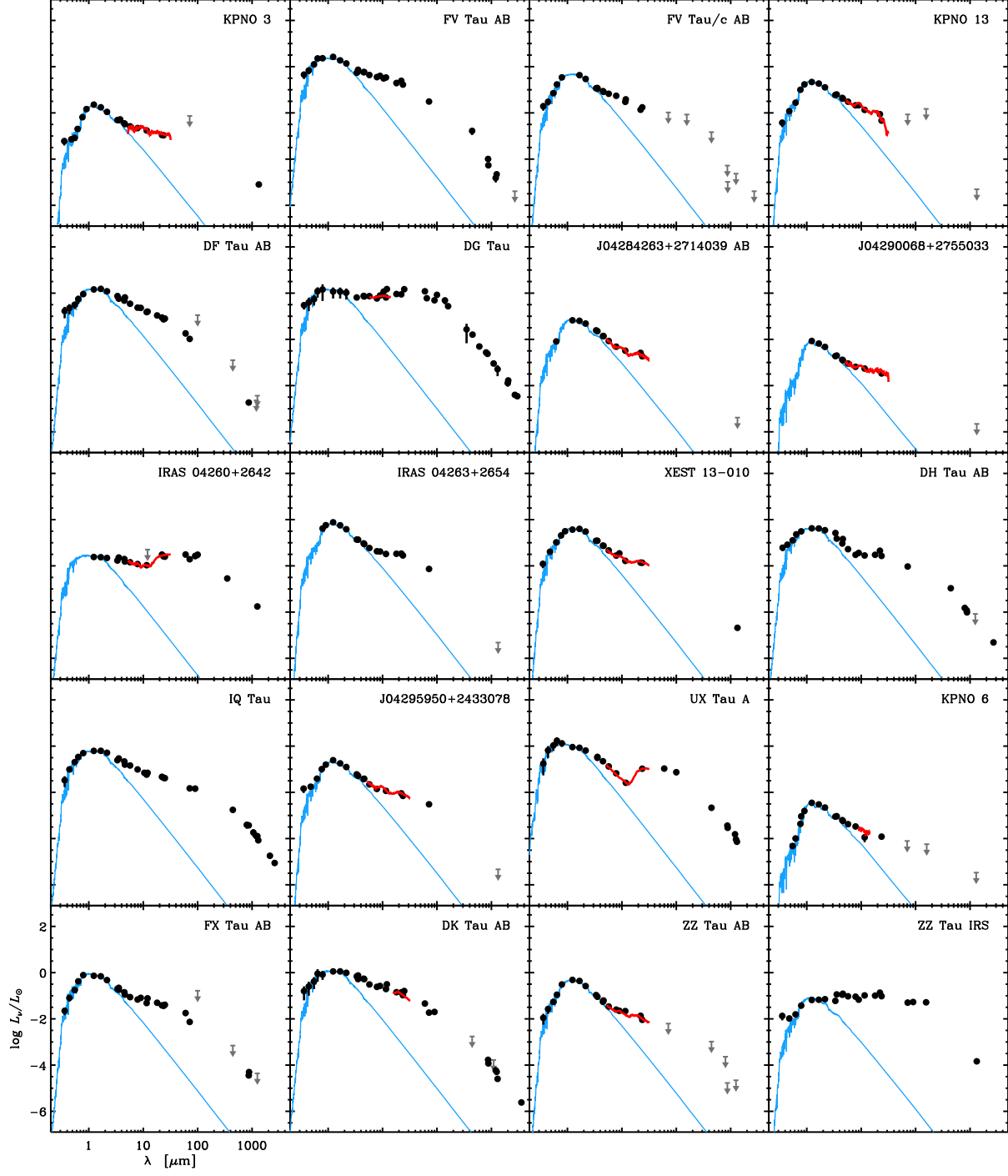


Fig. 13d.— As in panel (a).

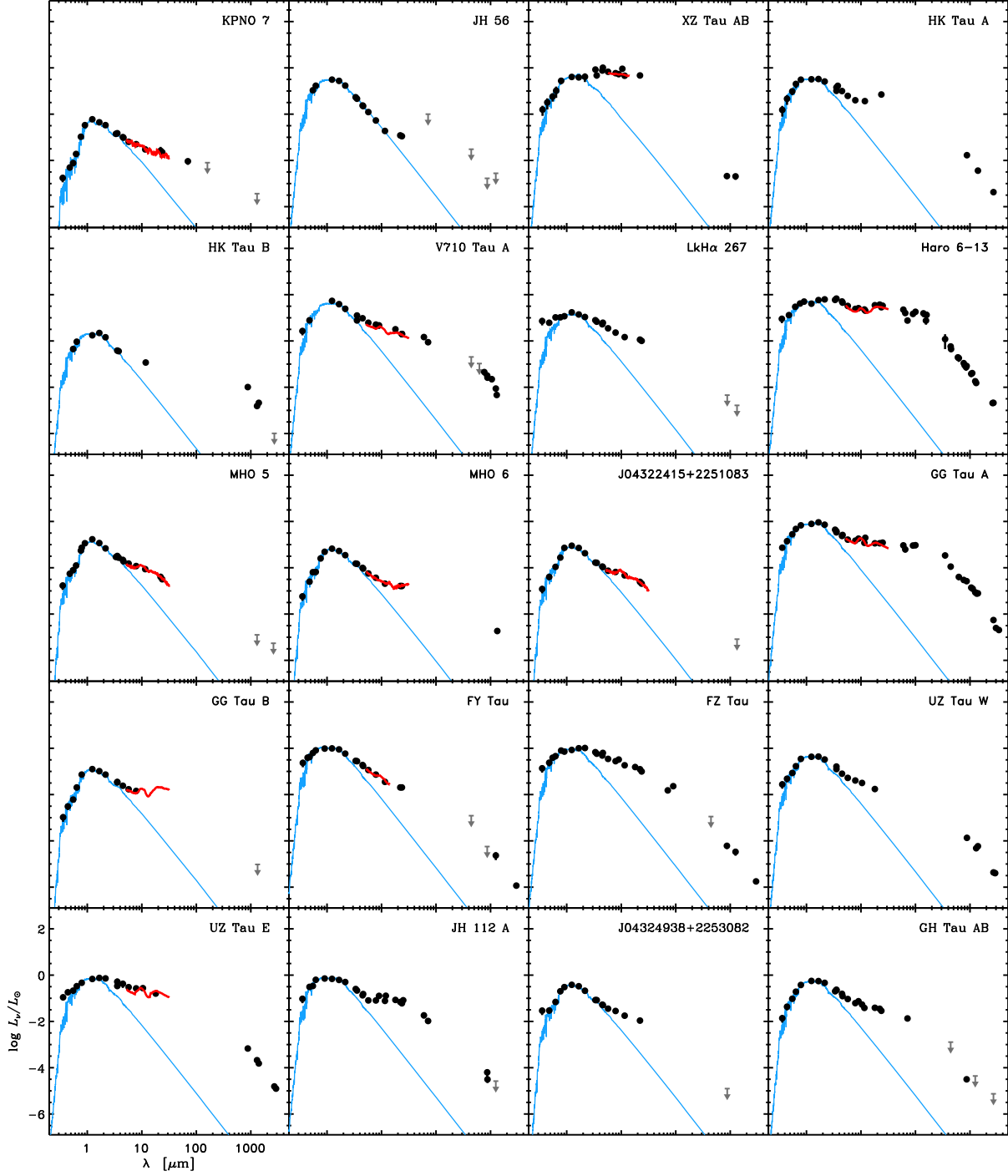


Fig. 13e.— As in panel (a). Note that the panel for V710 Tau A utilizes some composite, unresolved measurements for the A–B pair, but a stellar photosphere model for V710 Tau B has been subtracted (see Table 4 for V710 Tau B stellar parameters).

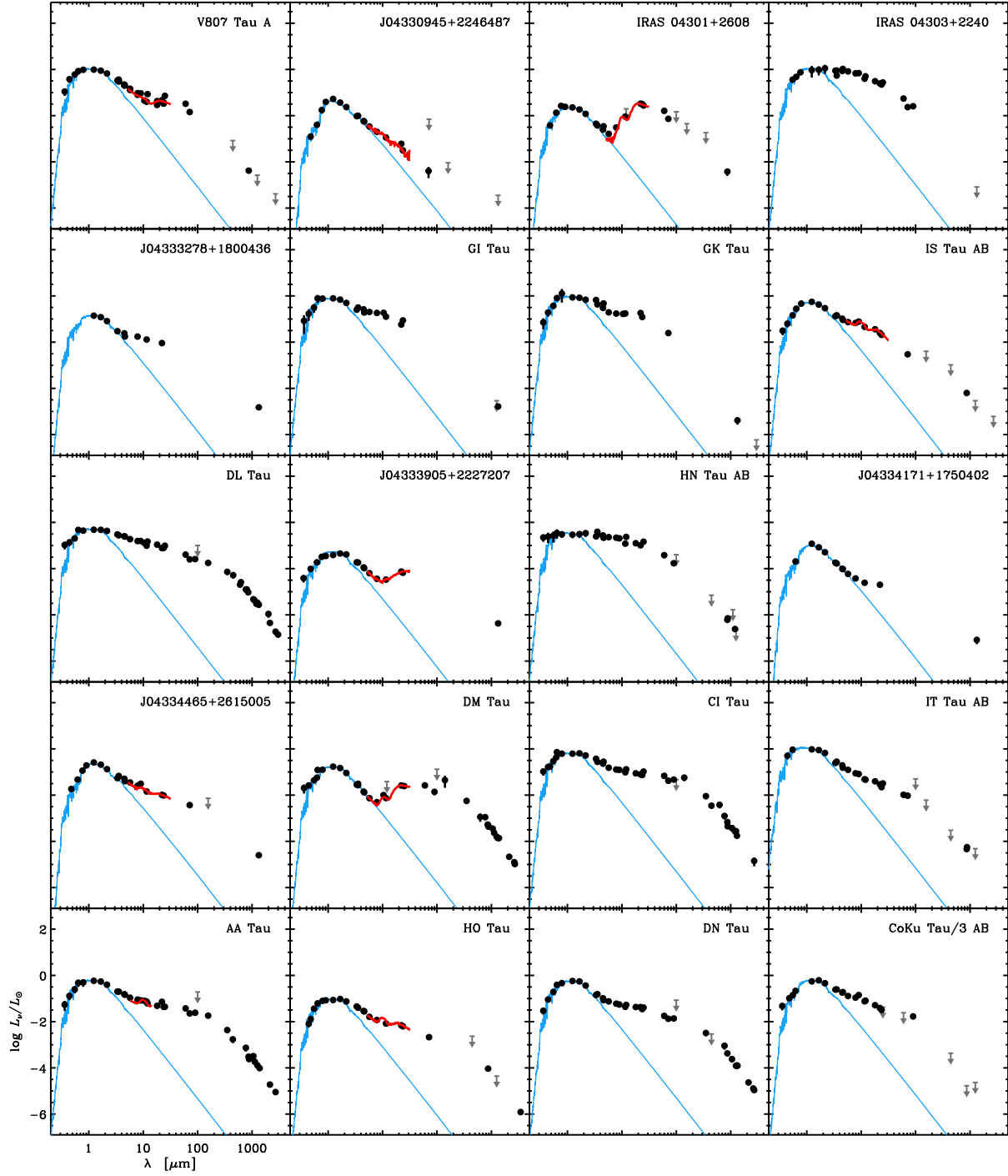


Fig. 13f.— As in panel (a). Note that the panel for V807 Tau A utilizes some composite, unresolved measurements for the A–B system, but a stellar photosphere model for V807 Tau B has been subtracted (see Table 4 for V807 Tau B stellar parameters).

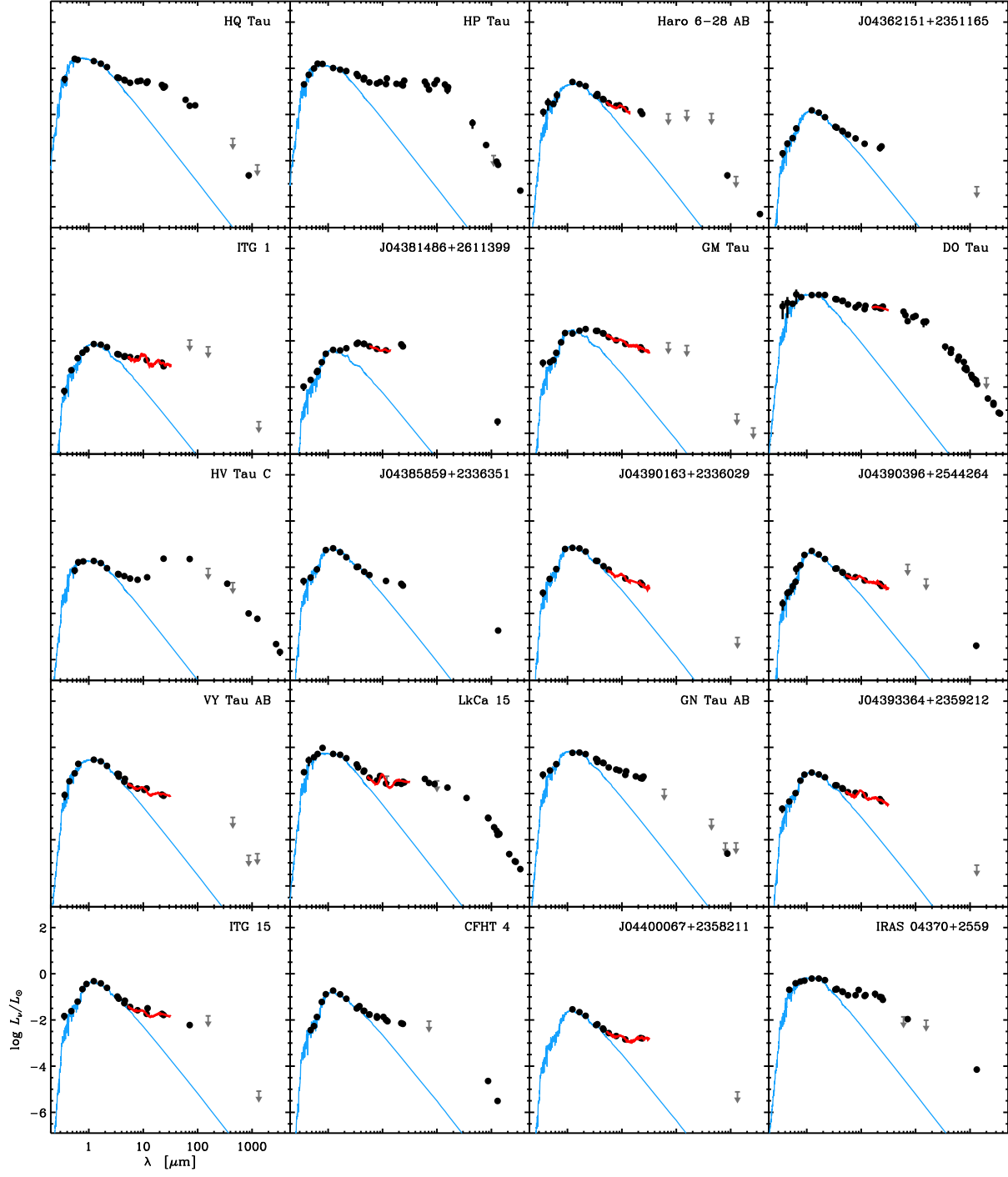


Fig. 13g.— As in panel (a).

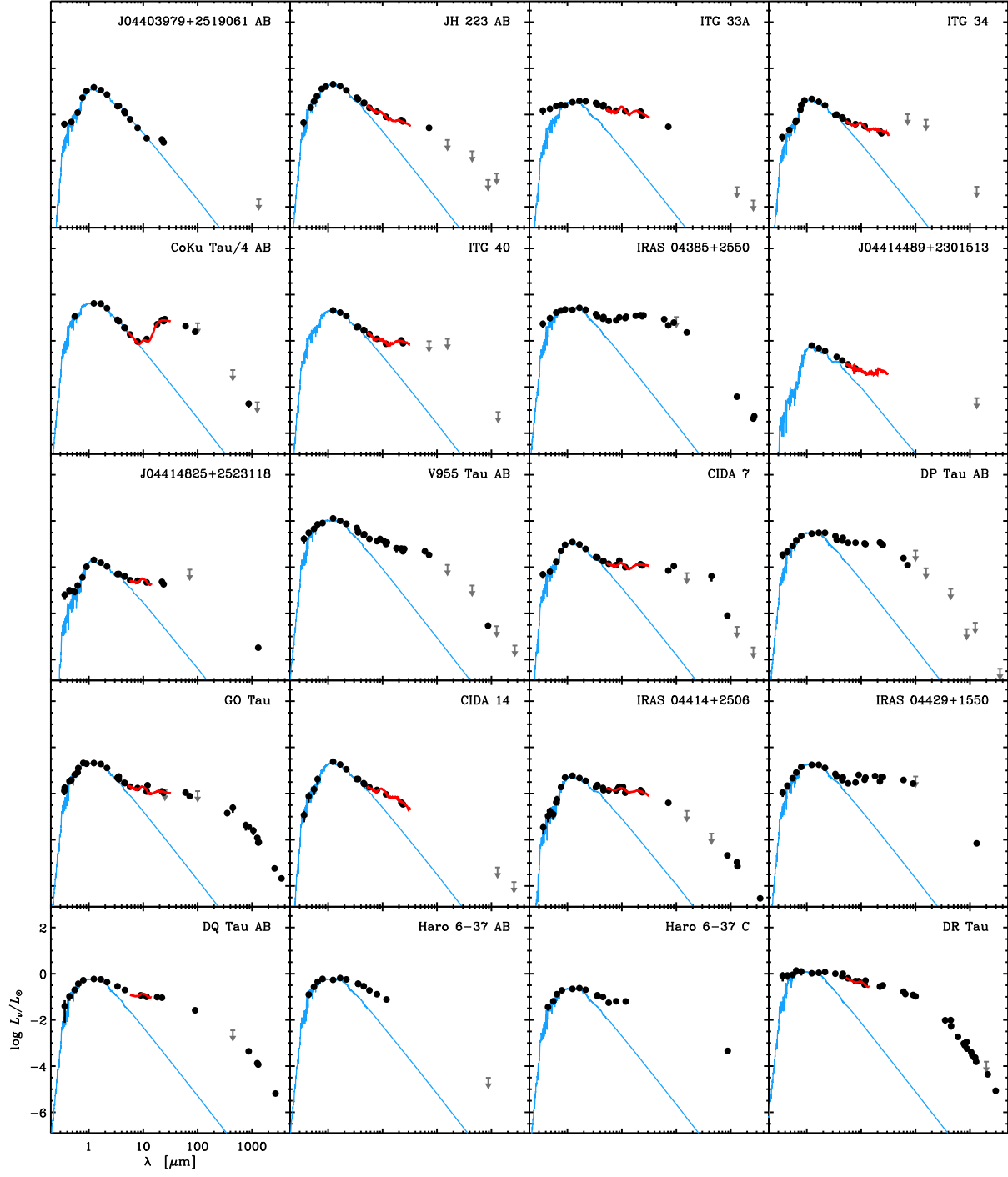


Fig. 13h.— As in panel (a).

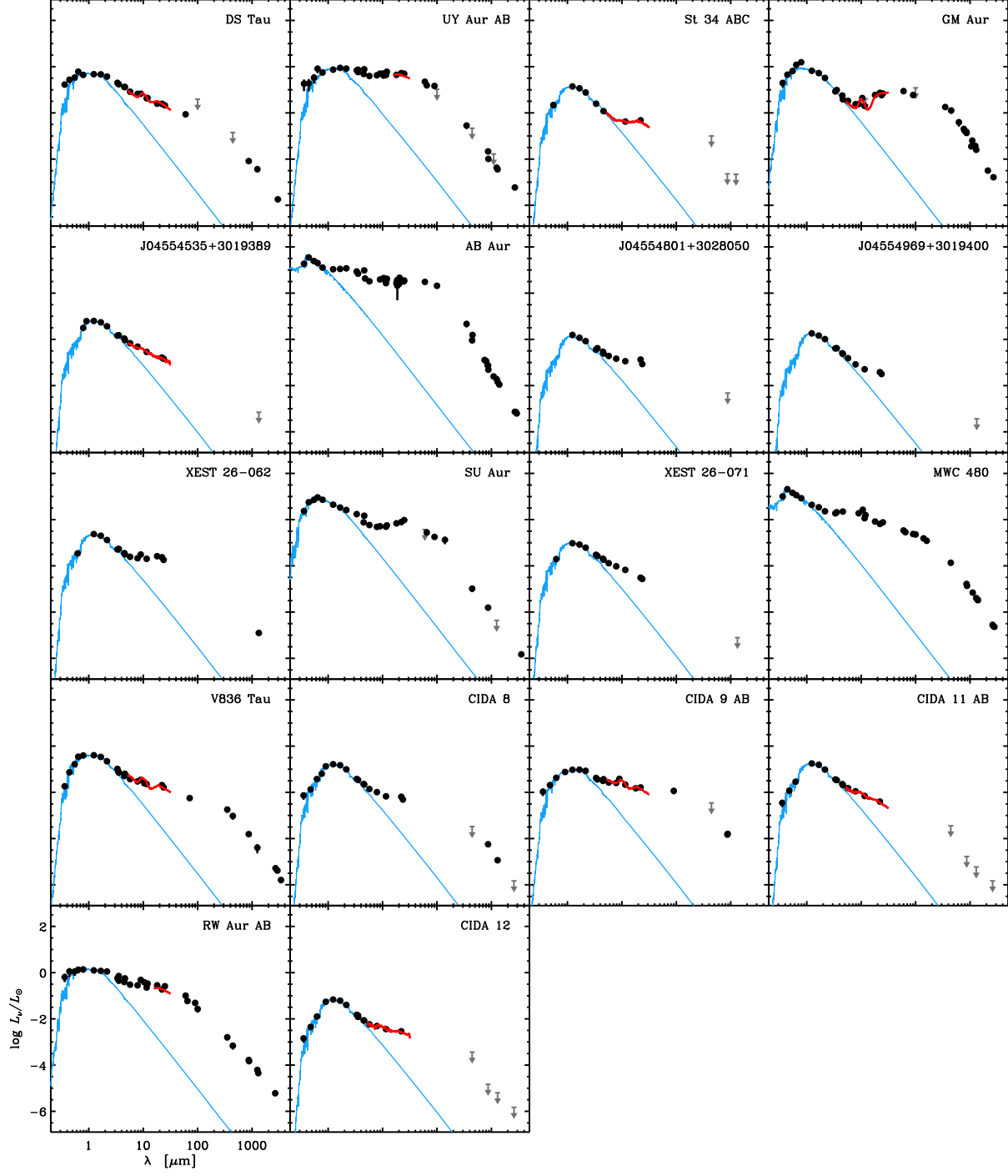


Fig. 13i.— As in panel (a).

wavelength, using an average of a sequence of normal distributions,

$$\langle \mathcal{F}(m) \rangle = \frac{1}{N} \sum_{i=1}^N \frac{1}{\sqrt{2\pi}\sigma_i} \exp \left[-\frac{(m - \mu_i)^2}{\sigma_i^2} \right], \quad (\text{A1})$$

where N is the number of measurements, μ_i are the reported magnitudes, and $\sigma_i^2 = \sigma_{m,i}^2 + \sigma_{s,i}^2$. In most cases, $\langle \mathcal{F}(m) \rangle$ has a single, clearly defined (if asymmetric) peak that we then define as the representative magnitude in the ensemble, $\langle m \rangle$. The cumulative distribution of $\langle \mathcal{F}(m) \rangle$ is used to assign a noise term caused by variability, σ_v , that represents the central 68% of the composite distribution. In essence, this is a slightly more sophisticated version of a weighted mean and standard deviation. For the many other sources that do not have sufficient data available to measure $\langle \mathcal{F}(m) \rangle$, we assign a mean σ_v term determined from this subset: $\bar{\sigma}_v = 0.33$ mags in B , 0.25 mags in V and R , and 0.11 mags in I .⁸ Near-infrared variability studies are rare for Taurus sources, so we adopt the results of a similar analysis of analogous sources in Orion by Carpenter et al. (2001), where $\bar{\sigma}_v \approx 0.09, 0.08$, and 0.07 mags at J , H , and K_s (in the 2MASS system). Flux densities are calculated assuming the zero-points advocated by Bessell (1979) – $F_U = 1810$, $F_B = 4260$, $F_V = 3640$, $F_R = 3080$, and $F_I = 2550$ Jy – and in the 2MASS point source catalog explanatory supplement (Cutri et al. 2003) – $F_J = 1594$, $F_H = 1024$, and $F_{K_s} = 667$ Jy.

At longer infrared wavelengths, the SEDs shown in Figure 13a were collected primarily from *Spitzer* imaging surveys (Luhman et al. 2010; Rebull et al. 2010), the *Wide-field Infrared Survey Explorer* (*WISE*) all-sky catalog (Wright et al. 2010), the *AKARI* point source catalogs (Ishihara et al. 2010), and the *Infrared Astronomical Satellite* (*IRAS*) point source catalog (Beichman et al. 1988), with some additional ground- and space-based measurements (Strom et al. 1989; Hillenbrand et al. 1992; Malfait et al. 1998; White & Ghez 2001; Liu et al. 2003; Jayawardhana et al. 2003; Chen & Jura 2003; Apai et al. 2004; Metchev et al. 2004; Pantin et al. 2005; McCabe et al. 2006, 2011; Kundurthy et al. 2006; Mariñas et al. 2006; Bouy et al. 2008; Monnier et al. 2008; Ratzka et al. 2009; Duchêne et al. 2010; Honda et al. 2010; Skemer et al. 2010; Wahhaj et al. 2010; Gräfe et al. 2011; Harvey et al. 2012). In addition to the new data presented here (see Table 1), integrated flux density measurements in the submillimeter–radio spectrum are compiled from various catalogs in the literature (Weintraub et al. 1989; Adams et al. 1990; Beckwith et al. 1990; Beckwith & Sargent 1991; Altenhoff et al. 1994; Jewitt 1994; Mannings & Emerson 1994; Jensen et al. 1994; Koerner et al. 1995; Osterloh & Beckwith 1995; Ohashi et al. 1996; Momose et al. 1996, 2010; Kitamura et al. 1996, 2002; Dutrey et al. 1996, 2003; Mannings & Sargent 1997; Hogerheijde et al. 1997; di Francesco et al. 1997; Henning et al. 1998; Dent et al. 1998; Akeson et al. 1998; Guilloteau & Dutrey 1998; Guilloteau et al. 1999, 2011; Looney et al. 2000; Duvert et al. 2000; Motte & André 2001; Klein et al. 2003; Jensen & Akeson 2003; Duchêne et al. 2003, 2010; Corder et al. 2005; Piétu et al. 2005, 2006, 2011; Lin et al. 2006; Moriarty-Schieven et al. 2006; Scholz et al. 2006; Hamidouche et al. 2006; Andrews & Williams

⁸For reference, we also found $\bar{\sigma}_v \approx 0.4$ mags in U , but the $\langle \mathcal{F}(m) \rangle$ were much more complex than at longer wavelengths (due to accretion variability). There is circumstantial evidence that the scatter in R is partially tied to variability in $H\alpha$, in that the sources with larger scatter tend to have higher $H\alpha$ equivalent widths (or luminosities).

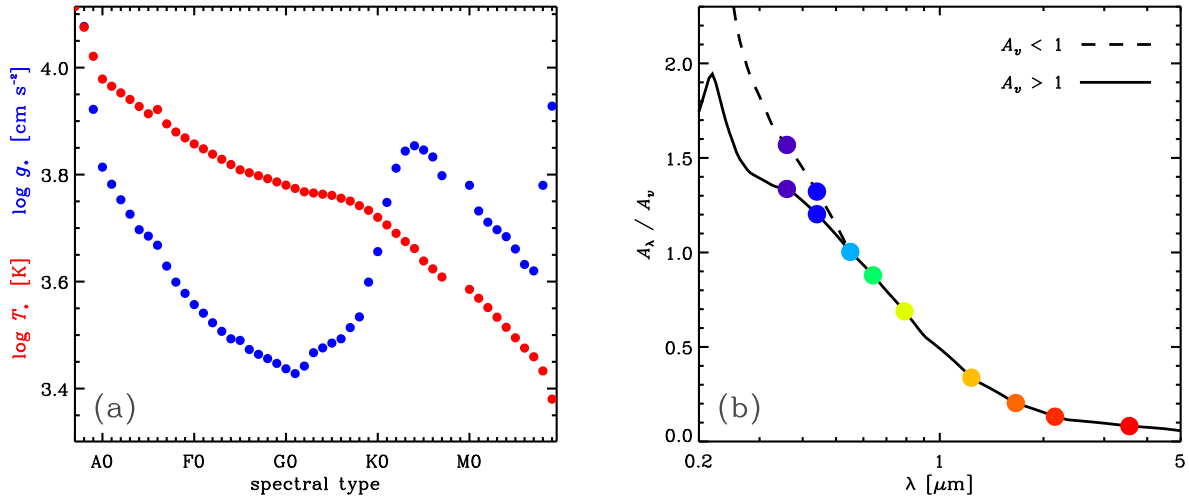


Fig. 14.— (a) The assumed correspondances between T_* (*red*) or $\log g_*$ (*blue*) and spectral type used in our derivation of the observable quantities of the H-R diagram. (b) The extinction curves used in our derivations of stellar luminosities, based on the work by Mathis (1990) and McClure (2009). Colored dots represent the common optical/near-infrared filter bands, for reference.

2005, 2007b; Rodmann et al. 2006; Cabrit et al. 2006; Bouy et al. 2008; Hughes et al. 2008, 2009; Schaefer et al. 2009; Isella et al. 2009, 2010, 2012; Hamidouche 2010; Öberg et al. 2010; Ricci et al. 2010, 2012, 2013; Andrews et al. 2011; Phan-Bao et al. 2011; Sandell et al. 2011; Cieza et al. 2012; Harris et al. 2012, 2013).

B. Effective Temperatures and Stellar Luminosities

As mentioned in §3.1, effective temperatures are assigned based on the correspondances with spectral classification advocated by Schmidt-Kaler (1982), Straižys (1992), and Luhman (1999), as shown in Figure 14(a) (*red* curve). In most cases, the spectral types in Table 2 were culled from the Luhman et al. (2010) catalog (alternative references are in the table notes). We assume the default uncertainty on a type is ± 1 sub-class, and associate a normal (1σ) uncertainty on T_* based on the (largest) temperature difference corresponding to that range of types. Some early-type stars have a wider range of published spectral types (see Table 2), which are appropriately reflected in their adopted T_* uncertainties. The published classifications for many mid/late-M stars are more accurate than assumed here (± 0.5 sub-classes or better; e.g., Luhman et al. 2009a), but we feel our conservative approach is warranted due to the lingering uncertainty in the type – temperature conversion. Spectral classifications for individual stars in 17 close multiple systems are not available (for others, see Duchêne et al. 1999; Hartigan & Kenyon 2003, or the Table 2 notes). In those cases, we assign the composite type to the primary and constrain the type/temperature of the secondary with two limiting assumptions: (1) $T_{*,1} \geq T_{*,2}$ (by definition), and (2) the ratio of stellar radii is

≥ 1 , so $T_{*,2} \geq T_{*,1}(L_{*,2}/L_{*,1})^{1/4}$. The mean optical/near-infrared contrast is used as a proxy for the luminosity ratio in condition (2), and then a temperature and uncertainty are defined as the midpoint and half the range of permissible $T_{*,2}$ values, respectively (corresponding spectral types are assigned from the conversion in Fig. 14a). This approach works well for binaries where individual types are known, and still properly reflects the intrinsic classification uncertainty. It is similar to the method used by Kraus et al. (2011), but has the benefit of not referencing pre-MS evolution models. Finally, three sources (FT Tau, ITG 1, and IRAS 04370+2559) remain unclassified: types and uncertainties were assigned based on the rough accounting bins of Luhman et al. (2010).

We chose to not rely on previous assignments of luminosities because of the heterogeneous measurement techniques adopted in the literature. Instead, we developed a method that estimates luminosities (L_*) and extinctions (A_V) – and their uncertainties – by fitting spectral templates of stellar photosphere models to the optical and near-infrared SED (similar in spirit to the methods used by Bailer-Jones 2011; Brown et al. 2011; Da Rio & Robberto 2012). The basic approach is simple. First, we select a template spectrum based on the spectral type, using the conversions in Figure 14(a) to an appropriate T_* and $\log g_*$. The gravity dependence of the spectrum makes little difference in terms of the broadband photometry being fitted: deviations from these values by up to 0.3 dex produce only small $\{L_*, A_V\}$ changes that are well within the uncertainties determined here. The $\log g_*$ behavior in Figure 14(a) (*blue* curve) corresponds to the mean behavior of the three pre-MS evolution models utilized in §3.2.1 at an age of ~ 2 Myr. We adopt the **NextGen**/PHOENIX-based (Hauschildt et al. 1999) “BT-settl” model templates (Allard et al. 2003, 2011) assuming solar metallicity, although other models (e.g., Lejeune et al. 1997) produce comparable end results. Next, we scale and redden the template for a given $\{L_*, A_V\}$. The adopted extinction curves are shown in Figure 14(b). At low extinctions ($A_V < 1$) we use the standard Cardelli et al. (1989) curve ($R_V = 3.1$). At higher A_V we prefer the McClure (2009) relation, which is based on *Spitzer* observations through dark clouds (and equivalent at the wavelengths of interest to the $R_V = 5$ case of Mathis 1990). Then, we generate a synthetic model SED by convolving the scaled, reddened template with the relevant set of filter profiles to facilitate a proper comparison with the data.

Each model is evaluated with a likelihood function, $\ln(\mathcal{L}) \propto -\chi^2/2$, that is directly related to the standard χ^2 statistic summed over a range of wavelengths (0.4–4 μm), depending on availability and a visual inspection for dust contamination in the infrared.⁹ A Monte Carlo Markov Chain (MCMC) technique is employed to maximize \mathcal{L} and determine the marginal posterior probability density functions $p(\log L_*|\{F_\nu\})$ and $p(A_V|\{F_\nu\})$, where $\{F_\nu\}$ represents the set of fitted flux density measurements, using the Goodman & Weare (2010) ensemble sampler as implemented by Foreman-Mackey et al. (2013). However, this parameter estimation process does not directly account for T_* uncertainties on the inferences of $\{\log L_*, A_v\}$. In principle that could be achieved by treating T_* as another free parameter, but the broadband SED is a poor effective temperature diagnostic compared to a detailed spectrum (from which a spectral type, and therefore T_* ,

⁹Note that U or u' data are never used, due to contributions from accretion energy (e.g., Gullbring et al. 1998).

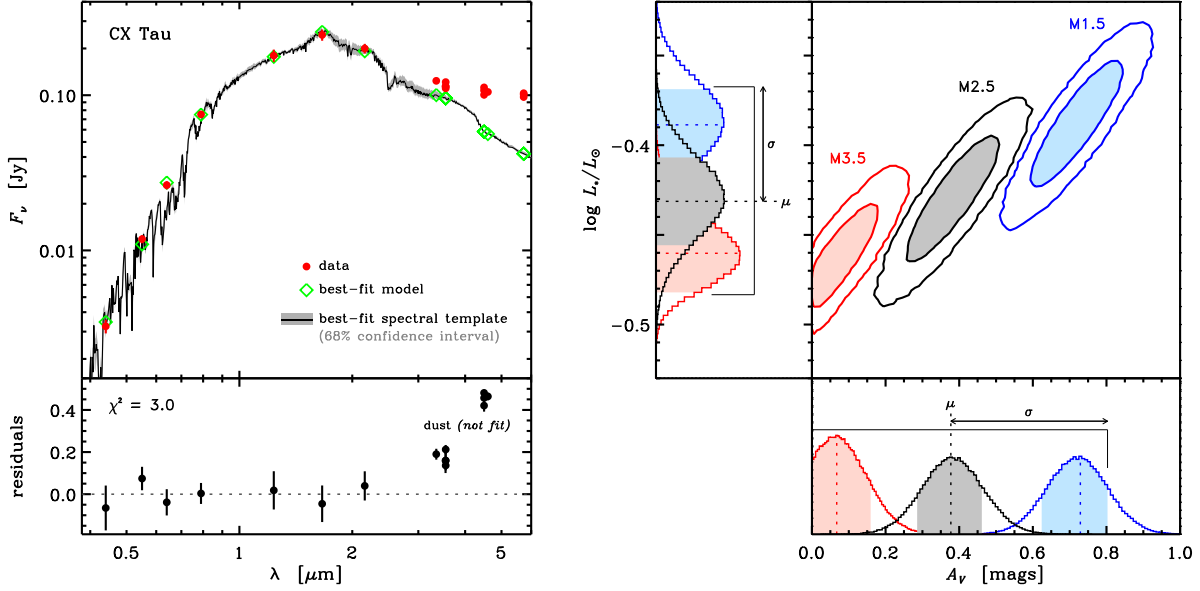


Fig. 15.— A graphical illustration of the fitting technique used to derive $\{\log L_*, A_v\}$ (e.g., for CX Tau, spectral type $M2.5 \pm 1$). (*left*) The broadband SED for CX Tau (*red* points) are compared with the best-fit scaled, reddened **NextGen** spectral template (*black* curve: *gray* shading represents the variations allowed within the 68% confidence intervals of $\{T_*, \log L_*, A_v\}$), and the best-fit SED model (*green* points) determined by convolving the template with the appropriate observational filter profiles. The fractional residuals of that model fit are shown in the lower panel. (*right*) The marginal distributions $p(\log L_* | \{F_\nu\})$ (ordinate), $p(A_v | \{F_\nu\})$ (abscissa), and their joint two-dimensional projections derived from the MCMC fitting for the nominal spectral type (*gray*) and the extrema classifications of ± 1 sub-class (*blue* and *red*, respectively). Contours are drawn at 68 and 95% confidence intervals; the 68% level is shaded. The diagrams mark the adopted best-fit value for each parameter (μ) and its associated uncertainty (σ), as described in the text.

is derived here). Instead, we fold in the T_* uncertainty with a discretized, brute-force approach: the entire modeling process is simply repeated two additional times, for templates with effective temperatures $T_* \pm \sigma(T_*)$. The best-fit $\{\log L_*, A_v\}$ are identified from the peaks of their marginal posterior distributions for the nominal T_* , and their “1- σ ” uncertainties are assigned from the (maximal) distance to the 68% confidence interval in the posterior distributions for the $T_* \pm \sigma(T_*)$ results: mathematically, $\sigma(x) = \max\{|\mu(x) \pm \sigma(x)|_{T_* \pm \sigma(T_*)} - [\mu(x)]_{T_*}\}$, where $x \in \{\log L_*, A_v\}$, $\mu(x)$ denotes the best-fit x , and $\sigma(x)$ the 68% uncertainty derived from $p(x | \{F_\nu\})$. An example of the fitting process is summarized graphically in Figure 15, for the arbitrary case of CX Tau.

We should point out that the adopted modeling procedure explicitly ignores any excess luminosity from accretion. High spectral resolution measurements from the ultraviolet through the near-infrared suggest that a veiling continuum can contribute a non-negligible amount to the observed emission, particularly at blue-optical wavelengths (e.g., Basri & Batalha 1990; Hartigan et al. 1991,

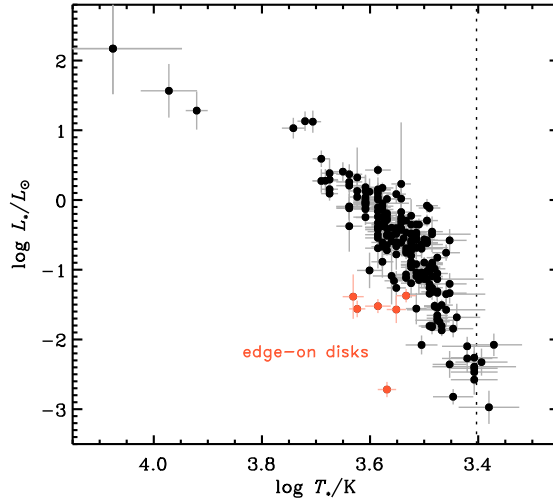


Fig. 16.— The H-R diagram for Class II sources in Taurus, as compiled in Table 3. The dotted vertical line marks the completeness limit in spectral type for this catalog.

1995; Gullbring et al. 1998). Recently, Fischer et al. (2011) demonstrated that even the near-infrared peak of the typical SED can exhibit an excess (Cieza et al. 2005, for high accretion rates; see also). In some pathological cases, that excess can dominate the L_* values determined with our adopted procedure (and certainly affects the context in which the A_V values should be considered), but more often the accretion contribution plays a lesser role. Regardless, the L_* values inferred here are likely slight over-estimates of the true stellar luminosities. Therefore, the stellar ages estimated in §3.2 would be correspondingly younger than the true values. However, we do not expect accretion to significantly bias the derived M_* values that are derived with the results of these stellar model fits, since the pre-MS model mass tracks scale roughly with T_* (e.g., see Fig. 4).

Following the prescription outlined above, we derived estimates of the fundamental stellar “observables” $\{\log T_*, \log L_*, A_V\}$ and their uncertainties for the full sample catalog: the results are compiled in Table 4 and shown together in the H-R diagram in Figure 16. Special care was taken in the fitting for stars in close multiple systems. When component-resolved photometry at *more than two wavelengths* was not available (e.g., not covered by White & Ghez 2001; Woitas et al. 2001, or similar work), we assumed that both components had the same extinction and fit both the contrasts and the composite SED simultaneously to estimate individual luminosities (see notes in Table 3). There are 6 stars in this sample that are either known or strongly suspected to have edge-on disk orientations, either from direct high-resolution imaging (HK Tau B, HV Tau C; Duchêne et al. 2003; McCabe et al. 2011) or a combination of an anomalously low L_* (a $>2\text{-}\sigma$ deviation from the mean luminosity at that spectral type), high A_V , or unusual optical/near-infrared SED morphology (J04202144+2813491, IRAS 04260+2642, IRAS 04301+2608, and ITG 33A).¹⁰ Those sources are

¹⁰Note that LkHα 267 exhibits an anomalously low extinction in the optical bands that are inconsistent with the

marked in Figure 16 and Table 4. The inferred L_* values for these cases are not representative of the true stellar luminosities, due to substantial obscuration from disk material along the line-of-sight to the central stars. When estimating stellar masses and ages for these sources (see §3.2), we assign a luminosity and associated uncertainty based on the weighted mean and standard deviation of the L_* values for all other sources within ± 1 spectral type sub-class.

C. Comments on the Dust Temperature Scaling

In §3.2.2, we adopted a disk-averaged dust temperature that scaled weakly with the host star luminosity, $\langle T_d \rangle \approx 25 (L_*/L_\odot)^{1/4}$ K, as a basic assumption in the conversion of mm-wave continuum luminosities to dust disk masses (see Eq. 2). From a theoretical perspective, this approximate scaling is appropriate only for the strictly optically thin case. However, the disk midplanes responsible for the mm-wave emission studied here are heated indirectly, by radiation from an optically thick layer of dust in the disk atmosphere (e.g., Chiang & Goldreich 1997; D’Alessio et al. 1998). So, there is a valid question about whether or not this intermediate step in the supply chain of thermal energy to the disk interior preserves the scaling with the original irradiation source properties (i.e., L_*). There is no simple analytic prescription for answering this question a priori, and (to our knowledge) this has not been specifically addressed with a simple parameter study that uses continuum radiative transfer calculations in the literature. So, to assess the basic applicability of this assumed scaling, we performed such a parameter study here.

This demonstration followed the general modeling formalism outlined by Andrews et al. (2009, 2011). A two-dimensional model grid of dust densities was constructed from simple radial prescriptions for the surface densities, $\Sigma \propto r^{-1}$, and vertical scale heights, $H \propto r^{1.15}$, between an inner radius (set by the assumed dust destruction temperature of 1500 K; see Dullemond et al. 2001) and a fixed outer edge at $r = 200$ AU (e.g., Andrews & Williams 2007b), such that $\rho(r, z) = (\Sigma/\sqrt{2\pi}H) \exp[-(z/H)^2/2]$. We adopted the settled dust prescription and opacities discussed by Andrews et al. (2011), where small grains representing only 10% of the total dust mass are distributed at larger vertical heights to intercept stellar irradiation, and the remaining 90% of the mass is concentrated in larger grains near the disk midplane (with a scale height of only $0.2H$). We assumed $H \approx 28$ AU at the outer edge in all models. Three different scenarios for normalizing Σ were considered: (1) an optically thin reference case where $M_d = 0.001 M_\odot$; (2) a more massive counterpart where $M_d = 0.01 M_\odot$; and (3) an a posteriori check on the regression results of §3.2.2, where $M_d/M_* \approx 0.4\%$. We used the Monte Carlo radiative transfer code RADMC-3D (v0.35; C. P. Dullemond)¹¹ to compute a two-dimensional dust temperature structure that is physically consistent with the irradiation of a given parametric density structure by an appropriate stellar

observed luminosity in the near-infrared (Kraus & Hillenbrand 2009). We elect to fit the $i'z'JH$ data only here, but note that this source might also be consistent with an edge-on disk (or perhaps some remnant envelope material).

¹¹[http://www.ita.uni-heidelberg.de/\\$\sim\\$dullemond/software/radmc-3d/](http://www.ita.uni-heidelberg.de/\simdullemond/software/radmc-3d/)

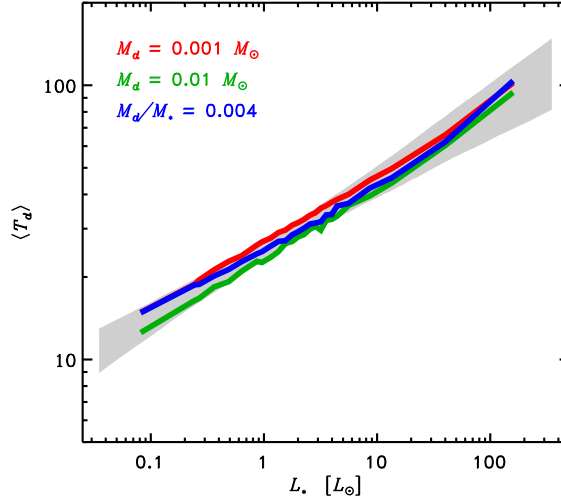


Fig. 17.— A demonstration that the assumed scaling between the disk-averaged dust temperature (weighted by mass) and the stellar host luminosity is reasonable, using radiative transfer calculations for representative disk structure models. The red and green curves show how $\langle T_d \rangle$ varies with L_* for model disk structures with fixed masses of $M_d = 0.001$ and $0.01 M_\odot$, respectively, and stellar parameters along the SDF00 2.5 Myr isochrone. The blue curve marks the analogous behavior for a linear $M_d \propto M_*$ scaling with the normalization found in §3.2.2, as an a posteriori verification of the assumed dust temperatures. The gray shaded band encloses the assumed scaling of $\langle T_d \rangle = 25 (L_*/L_\odot)^{1/4}$ K, within a range of ± 2 K in the normalization and ± 0.05 in the index, for reference.

photosphere model. For each scenario, this was repeated for 25 different input stellar photosphere spectra interpolated from the **NextGen** catalog as described in Appendix B, corresponding to the basic stellar properties along the 2.5 Myr isochrone in the SDF00 models.

The results of these calculations are presented in Figure 17, where we show the mass-weighted average midplane temperature as a function of the input L_* for Scenarios 1, 2, and 3 in red, green, and blue, respectively (the same results are found if we instead use the $\langle T_d \rangle$ that would be inferred from an inversion of Eq. 2, based on the input M_d values and synthetic 1.3 mm flux densities generated by **RADMC-3D**). The shaded gray region corresponds to the adopted dust temperature scaling, with an allowed range of ± 2 K in the normalization and ± 0.05 in the power-law index (for illustrative purposes). Overall, this simple, controlled parameter study provides some basic verification that the $\langle T_d \rangle$ scaling with L_* that was assumed in §3.2.2 is quantitatively reasonable for normal, representative disk parameters. However, some caution should be exercised in generalizing or extrapolating the application of this behavior: variations in the fixed parameters – particularly the scale height distribution – can also induce changes in the shape of this scaling if they depend on the stellar parameters, as was described in more detail in §3.2.3.

Table 1. New 1.3 mm Photometry Measurements

UT Date	Name	F_ν (mJy) ^a
2012 Nov 17	IRAS 04187+1927	< 6.3
	MHO 6	13.5 ± 2.0
	J04322415+2251083	< 6.0
	J04333278+1800436	11.0 ± 1.9
	IRAS 04303+2240	< 6.0
	J04333905+2227207	31.0 ± 2.0
	J04334171+1750402	6.0 ± 2.0
	J04390163+2336029	< 6.6
2012 Nov 25	IRAS 04429+1550	50.7 ± 2.0
	IRAS 04196+2638	51.3 ± 1.2
	J04230607+2801194	5.1 ± 1.1
	IRAS 04200+2759	36.6 ± 1.3
	J04231822+2641156	< 3.9
	J04242646+2649503	< 3.0
	KPNO 3	5.8 ± 1.2
	IRAS 04263+2654	< 3.5
2012 Nov 26	XEST 13-010	15.2 ± 1.2
	J04295950+2433078	< 3.4
	ZZ Tau IRS	105.8 ± 1.5
	J04153916+2818586	13.4 ± 1.4
	J04161210+2756385	< 4.2
	KPNO 10	7.8 ± 1.4
	V409 Tau	18.7 ± 1.4
	LR 1	30.8 ± 1.6
2012 Nov 30 ^b	J04202144+2813491	52.4 ± 1.5
	J04202555+2700355	8.4 ± 1.4
	J04202606+2804089	< 4.3
	J04214631+2659296	< 3.9
	J04221675+2654570	< 4.2
	J04334465+2615005	18.3 ± 1.7
	J04362151+2351165	< 5.4
	J04385859+2336351	13.2 ± 1.8
2012 Nov 30 ^b	J04393364+2359212	< 5.8
	ITG 15	< 6.0
	J04400067+2358211	< 5.6
	ITG 34	< 5.4
	ITG 40	< 6.0
	J04554535+3019389	< 5.1
	XEST 26-062	9.1 ± 1.5
	XEST 26-071	< 5.7

Table 1—Continued

UT Date	Name	F_ν (mJy) ^a
2013 Feb 7 ^c	J04163911+2958491	< 2.5
	J04210795+2702204	< 2.7
	IRAS 04173+2812	< 2.0
	ITG 1	< 2.3
	IRAS 04370+2559	51.7 ± 0.8
2013 Feb 14	J04201611+2821325	< 1.7
	J04242090+2630511	< 1.4
	FU Tau A	< 1.7
	FU Tau B	< 1.7
	J04290068+2755033	< 1.6
SMA archive		
2010 Nov 17	IRAS 04125+2902	19.5 ± 0.8
	V410 X-ray 2	15.0 ± 1.0
	V410 X-ray 6	< 2.1
	J04210934+2750368	< 1.8
	J04213459+2701388	< 3.0
2010 Nov 21	J04330945+2246487	< 2.6
	J04403979+2519061	< 1.6
	J04554969+3019400	< 2.7

^aUpper limits are listed at the 3- σ level.

^bAdditional observations of these same targets were made on 2012 Dec 2 and 2012 Dec 6, because the atmospheric opacity at 225 GHz was too high to meet the desired RMS noise level in an individual track. The data from all tracks were combined to measure these flux densities. The three detections were significant and consistent in each of the three tracks.

^cAs above, but additional observations were performed on 2013 Feb 8 and combined.

Table 2. Millimeter-wave Continuum Photometry Catalog

Name	Spectral Type ^a	Ref. ^b	$F_{1.3\text{mm}}$ (Jy) ^c	$F_{0.89\text{mm}}$ (Jy) ^c	Notes ^d
IRAS 04108+2910	M0	1	< 0.0517	< 0.0198	e, m
J04141188+2811535	M6.25	1	< 0.0509	< 0.0195	e, m
FM Tau	M0	1	0.0288 ± 0.0091	0.0131 ± 0.0027	m, e
FN Tau	M5	1	0.0365 ± 0.0050	0.0168 ± 0.0021	m, e
CW Tau	K3	1	0.1601 ± 0.0268	0.0523 ± 0.0070	m, m
CIDA 1	M5.5	1	0.0353 ± 0.0174	0.0135 ± 0.0028	e, m
MHO 1	M2.5	1	0.5295 ± 0.1207	0.2493 ± 0.0311	e, m
MHO 2 AB	M2.5, M5.5 \pm 3	1, est	0.3017 ± 0.0555	0.1377 ± 0.0142	e, m
MHO 3 AB	K7, M2 \pm 3	1, est	< 0.0313	< 0.0120	e, m
FP Tau	M4	1	< 0.0243	< 0.0093	e, m
CX Tau	M2.5	1	0.0251 ± 0.0076	0.0094 ± 0.0023	m, e
FO Tau A	M3.5	2	0.0130 ± 0.0030	0.0050 ± 0.0025	(m, e)
FO Tau B	M3.5	2	< 0.0090	< 0.0034	(m, e)
J04153916+2818586	M3.75	1	0.0350 ± 0.0161	0.0134 ± 0.0014	e, m
IRAS 04125+2902	M1.25	1	0.0400 ± 0.0042	0.0199 ± 0.0025	m, m
J04155799+2746175	M5.5	1	0.0329 ± 0.0152	0.0126 ± 0.0014	e, m
J04161210+2756385	M4.75	1	< 0.0110	< 0.0042	e, m
J04163911+2858491	M5.5	1	< 0.0065	< 0.0025	e, m
CY Tau	M1.5	1	0.1637 ± 0.0130	0.0794 ± 0.0059	m, m
KPNO 10	M5	1	0.0204 ± 0.0098	0.0078 ± 0.0014	e, m
V410 X-ray 1	M4	1	< 0.0090	< 0.0034	m, e
V409 Tau	M1.5	1	0.0488 ± 0.0222	0.0187 ± 0.0014	e, m
V410 Anon 13	M5.75	1	< 0.0235	< 0.0090	e, m
DD Tau A	M3.5	2	0.0240 ± 0.0030	0.0092 ± 0.0043	e, m
DD Tau B	M3.5	2	0.0090 ± 0.0030	0.0034 ± 0.0019	e, m
CZ Tau A	M3	1	< 0.0090	< 0.0034	m, e
CZ Tau B	M6 \pm 3	est	< 0.0090	< 0.0034	m, e
V410 X-ray 2	M0	1	0.0261 ± 0.0034	0.0154 ± 0.0023	m, m
V892 Tau AB	B8 \pm 3, B8 \pm 3	3	0.5922 ± 0.0586	0.2290 ± 0.0145	m, m
LR 1	K4.5	1	0.0804 ± 0.0363	0.0308 ± 0.0016	e, m
V410 X-ray 7 AB	M0.75, M2.75 \pm 2	1, est	< 0.0340	< 0.0130	e, m
V410 X-ray 6	M5.5	1	< 0.0055	< 0.0021	e, m
KPNO 12	M9	1	< 0.0055	< 0.0021	e, m
FQ Tau A	M3	2	0.0080 ± 0.0020	0.0031 ± 0.0016	m, e
FQ Tau B	M3.5	2	< 0.0050	< 0.0019	m, e
BP Tau	K7	1	0.1297 ± 0.0115	0.0415 ± 0.0022	m, m
V819 Tau	K7	1	< 0.0090	< 0.0025	m, m
FR Tau	M5.25	1	< 0.0392	< 0.0150	e, m
J04201611+2821325	M6.5	1	< 0.0044	< 0.0017	e, m
J04202144+2813491	M1	1	0.1369 ± 0.0615	0.0524 ± 0.0015	e, m
J04202555+2700355	M5.25	1	0.0219 ± 0.0105	0.0084 ± 0.0014	e, m
IRAS 04173+2812	M4	1	< 0.0052	< 0.0020	e, m
J04202606+2804089	M3.5	1	< 0.0112	< 0.0043	e, m
J04210795+2702204	M5.25	1	< 0.0071	< 0.0027	e, m
J04210934+2750368	M5.25	1	< 0.0047	< 0.0018	e, m
J04213459+2701388	M5.5	1	< 0.0078	< 0.0030	e, m

Table 2—Continued

Name	Spectral Type ^a	Ref. ^b	$F_{1.3\text{mm}}$ (Jy) ^c	$F_{0.89\text{mm}}$ (Jy) ^c	Notes ^d
IRAS 04187+1927	M0	1	< 0.0165	< 0.0063	e, m
J04214631+2659296	M5.75	1	< 0.0102	< 0.0039	e, m
DE Tau	M1	1	0.0843 ± 0.0103	0.0311 ± 0.0031	m, m
RY Tau	K1	1	0.4987 ± 0.0334	0.1925 ± 0.0091	m, m
T Tau N	K0	1	0.5707 ± 0.0431	0.2272 ± 0.0126	m, m
FS Tau A	M0	2	0.0449 ± 0.0085	0.0182 ± 0.0051	(m, e)
FS Tau B	M3.5	2	< 0.0255	< 0.0101	(m, e)
J04221675+2654570	M1.5	1	< 0.0110	< 0.0042	e, m
IRAS 04196+2638	M1	1	0.1332 ± 0.0599	0.0510 ± 0.0012	e, m
J04230607+2801194	M6	1	0.0133 ± 0.0066	0.0051 ± 0.0011	e, m
IRAS 04200+2759	M2	4	0.0956 ± 0.0430	0.0366 ± 0.0013	e, m
J04231822+2641156	M3.5	1	< 0.0102	< 0.0039	e, m
FU Tau A	M7.25	1	< 0.0044	< 0.0017	e, m
FU Tau B	M9.25	1	< 0.0044	< 0.0017	e, m
FT Tau	(K6–M3.5)	1	0.1217 ± 0.0095	0.0629 ± 0.0043	m, m
J04242090+2630511	M6.5	1	< 0.0037	< 0.0014	e, m
J04242646+2649503	M5.75	1	< 0.0078	< 0.0030	e, m
IRAS 04216+2603	M0.5	1	< 0.0517	0.0198	e, m
IP Tau	M0	1	0.0320 ± 0.0058	0.0088 ± 0.0015	m, m
KPNO 3	M6	1	0.0151 ± 0.0075	0.0058 ± 0.0012	e, m
FV Tau A	K5	2	0.0150 ± 0.0010	0.0057 ± 0.0026	m, e
FV Tau B	K6	5	0.0110 ± 0.0010	0.0042 ± 0.0019	m, e
FV Tau/c A	M2.5	2	< 0.0050	< 0.0019	m, e
FV Tau/c B	M3.5	2	< 0.0050	< 0.0019	m, e
KPNO 13	M5	1	< 0.0094	< 0.0036	e, m
DF Tau AB	M2, M2.5	2, 2	0.0088 ± 0.0019	0.0034 ± 0.0017	m, e
DG Tau	K6	1	0.9447 ± 0.0780	0.3442 ± 0.0178	m, m
J04284263+2714039 A	M5.25	1	< 0.0078	< 0.003	e, m
J04284263+2714039 B	M7±2	est	< 0.0078	< 0.003	e, m
J04290068+2755033	M8.25	1	< 0.0042	< 0.0016	e, m
IRAS 04260+2642	K5.5	1	0.2706 ± 0.0500	0.1200 ± 0.0100	e, m
IRAS 04263+2654	M5.25	1	< 0.0091	< 0.0035	e, m
XEST 13-010	M3	1	0.0397 ± 0.0181	0.0152 ± 0.0012	e, m
DH Tau A	M1	1	0.0470 ± 0.0040	0.0180 ± 0.0082	m, e
DH Tau B	M7.5	6	< 0.0100	< 0.0038	m, e
IQ Tau	M0.5	1	0.1668 ± 0.0158	0.0619 ± 0.0045	m, m
J04295950+2433078	M5	1	< 0.0089	< 0.0034	e, m
UX Tau A	K2	7	0.1494 ± 0.0106	0.0545 ± 0.0083	m, m
KPNO 6	M8.5	1	< 0.0063	< 0.0024	e, m
FX Tau A	M1	8	0.0240 ± 0.0030	0.0092 ± 0.0043	m, e
FX Tau B	M4	8	< 0.0050	< 0.0019	m, e
DK Tau A	K8	8	0.0575 ± 0.0077	0.0166 ± 0.0033	m, e
DK Tau B	M1	8	< 0.0030	< 0.0011	m, e
ZZ Tau AB	M3, M4.5±2	1, est	< 0.0080	< 0.0031	m, e
ZZ Tau IRS	M5	1	0.2763 ± 0.1241	0.1058 ± 0.0015	e, m
KPNO 7	M8.25	1	< 0.0068	< 0.0026	e, m

Table 2—Continued

Name	Spectral Type ^a	Ref. ^b	$F_{1.3\text{mm}}$ (Jy) ^c	$F_{0.89\text{mm}}$ (Jy) ^c	Notes ^d
JH 56	M0.5	1	< 0.0080	< 0.0031	m, e
XZ Tau A	M2	2	0.0100 ± 0.0020	0.0038 ± 0.0019	(m, e)
XZ Tau B	M3.5	2	< 0.0060	< 0.0023	(m, e)
HK Tau A	M0.5	1	0.0811 ± 0.0089	0.0313 ± 0.0022	m, m
HK Tau B	M2	1	0.0456 ± 0.0059	0.0145 ± 0.0018	m, m
V710 Tau A ^e	M0.5	1	0.1193 ± 0.0142	0.0299 ± 0.0045	m, m
LkH α 267	M3	9	< 0.0220	< 0.0120	m, m
Haro 6-13	M0	1	0.2735 ± 0.0294	0.1196 ± 0.0057	m, m
MHO 5	M6	1	< 0.0235	< 0.0090	e, m
MHO 6	M4.75	1	0.353 ± 0.0167	0.0135 ± 0.0020	e, m
J04322415+2251083	M4.5	1	< 0.0157	< 0.0060	e, m
GG Tau Aab	K7, M0.5	10, 10	1.3447 ± 0.0907	0.4644 ± 0.0239	m, m
GG Tau Ba	M5.5	10	< 0.0183	< 0.0070	e, m
GG Tau Bb	M7.5	10	< 0.0183	< 0.0070	e, m
FY Tau	K5	1	0.0376 ± 0.0068	0.0138 ± 0.0051	e, m
FZ Tau	M0	1	0.0306 ± 0.0068	0.0137 ± 0.0024	m, e
UZ Tau Wa	M2	2	0.0354 ± 0.0039	0.0162 ± 0.0039	m, m
UZ Tau Wb	M3	2	0.0401 ± 0.0043	0.0310 ± 0.0041	m, m
UZ Tau Eab	M1, M4	11, 11	0.3472 ± 0.0343	0.1281 ± 0.0073	m, m
JH 112 A	K6	1	0.0100 ± 0.0030	0.0038 ± 0.0021	m, e
JH 112 B	M8.5 \pm 2	est	0.0050 ± 0.0030	0.0019 ± 0.0014	m, e
J04324938+2253082	M4.25	1	< 0.0060	< 0.0023	m, e
GH Tau A	M2	2	0.0150 ± 0.0030	0.0057 ± 0.0028	(m, e)
GH Tau B	M2	2	< 0.0090	< 0.0034	(m, e)
V807 Tau A ^e	K7	12	0.0200 ± 0.0030	0.0077 ± 0.0036	(m, e)
J04330945+2246487	M6	1	< 0.0068	< 0.0026	e, m
IRAS 04301+2608	M0	1	0.0180 ± 0.0060	0.0066 ± 0.0037	m, e
IRAS 04303+2240	M0.5	1	< 0.0157	< 0.0060	e, m
J04333278+1800436	M1	1	0.0287 ± 0.0138	0.0110 ± 0.0019	e, m
GI Tau	K7	1	0.0313 ± 0.0143	0.0120 ± 0.0010	e, m
GK Tau	K7	1	0.0078 ± 0.0044	0.0030 ± 0.0010	e, m
IS Tau A	M0	2	0.0300 ± 0.0030	0.0115 ± 0.0053	(m, e)
IS Tau B	M3.5	2	< 0.0090	< 0.0034	(m, e)
DL Tau	K7	1	0.4702 ± 0.0357	0.1688 ± 0.0108	m, m
J04333905+2227207	M1.75	1	0.0810 ± 0.0367	0.0310 ± 0.0020	e, m
HN Tau A	K5	13	0.0340 ± 0.0030	0.0130 ± 0.0060	m, e
HN Tau B	M4	13	< 0.0060	< 0.0023	m, e
J04334171+1750402	M4	1	0.0157 ± 0.0088	0.0060 ± 0.0020	e, m
J04334465+2615005	M4.75	1	0.0478 ± 0.0219	0.0183 ± 0.0017	e, m
DM Tau	M1	1	0.2370 ± 0.0117	0.0894 ± 0.0031	m, m
CI Tau	K7	1	0.2636 ± 0.0191	0.1057 ± 0.0057	m, m
IT Tau A	K3	8	0.0160 ± 0.0020	0.0061 ± 0.0029	m, e
IT Tau B	M4	8	0.0110 ± 0.0030	0.0042 ± 0.0022	m, e
AA Tau	K7	1	0.1394 ± 0.0082	0.0650 ± 0.0035	m, m
HO Tau	M0.5	1	0.0427 ± 0.0079	0.0177 ± 0.0033	m, e
DN Tau	M0	1	0.2101 ± 0.0182	0.0823 ± 0.0045	m, m

Table 2—Continued

Name	Spectral Type ^a	Ref. ^b	$F_{1.3\text{mm}}$ (Jy) ^c	$F_{0.89\text{mm}}$ (Jy) ^c	Notes ^d
CoKu Tau/3 A	M1	1	< 0.0080	< 0.0031	m, e
CoKu Tau/3 B	M4.5±2	est	< 0.0080	< 0.0031	m, e
HQ Tau	K2	1	0.0110 ± 0.0030	0.0042 ± 0.0022	m, e
HP Tau	K3	1	0.1136 ± 0.0161	0.0517 ± 0.0047	e, m
Haro 6-28 A	M2	2	0.0110 ± 0.0035	0.0049 ± 0.0012	(m, e)
Haro 6-28 B	M3.5	2	< 0.0105	< 0.0051	(m, e)
J04362151+2351165	M5.25	1	< 0.0141	< 0.0054	e, m
ITG 1	(M3.5–M6)	1	< 0.0060	< 0.0023	e, m
J04381486+2611399	M7.25	1	0.0060 ± 0.0034	0.0023 ± 0.0008	e, m
GM Tau	M6.5	1	< 0.0125	< 0.0048	e, m
DO Tau	M0	1	0.2528 ± 0.0258	0.1082 ± 0.0069	m, m
HV Tau C	K6	1	0.0474 ± 0.0070	0.0231 ± 0.0026	m, m
J04385859+2336351	M4.25	1	0.0345 ± 0.0162	0.0132 ± 0.0018	e, m
J04390163+2336029	M6	1	< 0.0172	< 0.0066	e, m
J04390396+2544264	M7.25	1	0.0076 ± 0.0040	0.0029 ± 0.0008	e, m
VY Tau A	M0	1	< 0.0100	< 0.0038	m, e
VY Tau B	M4.5±2	est	< 0.0100	< 0.0038	m, e
LkCa 15	K5	1	0.3852 ± 0.0224	0.1270 ± 0.0049	m, m
GN Tau A	M2.5	1	0.0120 ± 0.0030	0.0046 ± 0.0024	(m, e)
GN Tau B	M2.5±1.5	est	< 0.0090	< 0.0034	(m, e)
J04393364+2359212	M5	1	< 0.0151	< 0.0058	e, m
ITG 15	M5	1	< 0.0157	< 0.0060	e, m
CFHT 4	M7	1	0.0090 ± 0.0024	0.0020 ± 0.0005	m, m
J04400067+2358211	M6	1	< 0.0146	< 0.0056	e, m
IRAS 04370+2559	(K6–M3.5)	1	0.1350 ± 0.0606	0.0517 ± 0.0008	e, m
J04403979+2519061 AB	M5.25, M7±2	1, est	< 0.0042	< 0.0016	e, m
JH 223 A	M2	1	< 0.0070	< 0.0027	m, e
JH 223 B	M6±2	est	< 0.0070	< 0.0027	m, e
ITG 33A	M3	1	< 0.0133	< 0.0051	e, m
ITG 34	M5.5	1	< 0.0141	< 0.0054	e, m
CoKu Tau/4 AB	M1.5, M2±2	1, est	0.0090 ± 0.0029	0.0034 ± 0.0019	m, e
ITG 40	M3.5	1	< 0.0157	< 0.0060	e, m
IRAS 04385+2550	M0	1	0.0593 ± 0.0084	0.0255 ± 0.0022	e, m
J04414489+2301513	M8.5	1	< 0.0627	< 0.0240	e, m
J04414825+2534304	M7.75	1	0.0057 ± 0.0028	0.0022 ± 0.0004	e, m
V955 Tau A	K7	2	0.0140 ± 0.0020	0.0054 ± 0.0025	(m, e)
V955 Tau B	M2.5	2	< 0.0060	< 0.0023	(m, e)
CIDA 7	M4.75	1	0.0380 ± 0.0080	0.0145 ± 0.0072	m, e
DP Tau A	M0.5	1	< 0.0100	< 0.0038	m, e
DP Tau B	M2±1.5	est	< 0.0100	< 0.0038	m, e
GO Tau	M0	1	0.1624 ± 0.0123	0.0532 ± 0.0028	m, m
CIDA 14	M5	1	< 0.0018	< 0.0045	e, m
IRAS 04414+2506	M7.25	1	0.0116 ± 0.0013	0.0049 ± 0.0004	m, m
IRAS 04429+1550	M2.5	1	0.1332 ± 0.0600	0.0510 ± 0.0020	e, m
DQ Tau AB	M0, M0	14, 14	0.2107 ± 0.0188	0.0693 ± 0.0047	m, m
Haro 6-37 A	K7	1	< 0.0150	< 0.0057	m, e

Table 2—Continued

Name	Spectral Type ^a	Ref. ^b	$F_{1.3\text{mm}}$ (Jy) ^c	$F_{0.89\text{mm}}$ (Jy) ^c	Notes ^d
Haro 6-37 B	M4±3	est	< 0.0150	< 0.0057	m, e
Haro 6-37 C	M1	1	0.2180 ± 0.0060	0.0835 ± 0.0375	m, e
DR Tau	K5	1	0.3149 ± 0.0232	0.1152 ± 0.0069	m, m
DS Tau	K5	1	0.0405 ± 0.0069	0.0165 ± 0.0018	m, m
UY Aur A	M0	2	0.0390 ± 0.0030	0.0149 ± 0.0068	m, e
UY Aur B	M2.5	2	0.0100 ± 0.0030	0.0038 ± 0.0021	m, e
St 34 AB	M3, M3	15, 15	< 0.0110	< 0.0042	m, e
St 34 C	M5.5	16	< 0.0110	< 0.0042	m, e
GM Aur	K3	7	0.5466 ± 0.0358	0.1732 ± 0.0068	m, m
J04554535+3019389	M4.75	1	< 0.0133	< 0.0051	e, m
AB Aur	A0.5±1.5	1, 17	0.3087 ± 0.0224	0.0933 ± 0.0051	m, m
J04554801+3028050	M5.5	1	< 0.0230	< 0.0088	m, e
J04554969+3019400	M6	1	< 0.0071	< 0.0027	e, m
XEST 26-062	M4	1	0.0238 ± 0.0114	0.0091 ± 0.0015	e, m
SU Aur	G8±2	18	0.0710 ± 0.0086	0.0274 ± 0.0025	m, e
XEST 26-071	M3.5	1	< 0.0149	< 0.0057	e, m
MWC 480	A4.5±2	1, 19	0.7506 ± 0.0427	0.2566 ± 0.0093	m, m
V836 Tau	K7	1	0.0673 ± 0.0080	0.0291 ± 0.0024	m, m
CIDA 8	M3.5	1	0.0263 ± 0.0049	0.0077 ± 0.0016	m, m
CIDA 9 A	K8	1	0.0770 ± 0.0030	0.0295 ± 0.0133	m, e
CIDA 9 B	M1.5±2	est	< 0.0070	< 0.0027	m, e
CIDA 11 A	M3.5	1	< 0.0080	< 0.0031	m, e
CIDA 11 B	M4.5±1.5	est	< 0.0080	< 0.0031	m, e
RW Aur A	K2.5	20	0.0560 ± 0.0078	0.0272 ± 0.0022	m, m
RW Aur B	K5	8	0.0132 ± 0.0029	0.0044 ± 0.0008	m, m
CIDA 12	M4	1	< 0.0070	< 0.0027	m, e

^aUnless otherwise specified, the assumed spectral type uncertainty is ± 1 subclass.

^bThe spectral classifications were collated from the following references: 1 = Luhman et al. (2010), 2 = Hartigan & Kenyon (2003), 3 = Hernández et al. (2004), 4 = Furlan et al. (2011), 5 = White & Ghez (2001), 6 = Itoh et al. (2005), 7 = Espaillat et al. (2010), 8 = Duchêne et al. (1999), 9 = Kraus & Hillenbrand (2009), 10 = White et al. (1999), 11 = Prato et al. (2002), 12 = Schaefer et al. (2012), 13 = Hartigan et al. (1994), 14 = Mathieu et al. (1997), 15 = White & Hillenbrand (2005), 16 = Dahm & Lyke (2011), 17 = Roberge et al. (2001), 18 = Massarotti et al. (2005), 19 = Mora et al. (2001), 20 = Gahm et al. (2008). The ‘est’ flag means that the classification was crudely estimated based on the type of its primary companion and optical/near-infrared contrast ratios: more details on this modification to the classification process are available in Appendix B. The classifications for FT Tau, ITG 1, and IRAS 04370+2559 are unknown: we adopt the wide spectral type bins advocated by Luhman et al. (2010), listed here in parenthesis.

^cUpper limits are listed at the $3\text{-}\sigma$ level.

^dThe ‘m’ and ‘e’ flags denote whether each source has a flux density measurement available at (or near) 1.3 and 0.89 mm: ‘m’ implies direct measurement and ‘e’ implies an extrapolation as described in the text. Notes in parenthesis indicate unresolved multiple systems where composite measurements were applied to the primaries, and upper limits to the secondaries (see §3.1).

^eThe companions V807 Tau B (itself a binary) and V710 Tau B have no observational disk signatures, and are therefore excluded from this Class II sample. The V807 Tau system has no resolved mm-wave measurement, but we associate all of the composite emission with the primary

component. Harris et al. (2012) found no mm-wave emission associated with V710 Tau B.

Table 3. Stellar Host Masses and Ages

Name	DM97				BCAH98				SDF00			
	log M_*	CI(log M_*)	log t_*	CI(log t_*)	log M_*	CI(log M_*)	log t_*	CI(log t_*)	log M_*	CI(log M_*)	log t_*	CI(log t_*)
IRAS 04108+2910	-0.22	(-0.44, -0.18)	0.80	(0.13, 1.23)	-0.14	(-0.27, -0.05)	0.99	(0.48, 1.40)	-0.23	(-0.37, -0.15)	0.95	(0.49, 1.39)
J04141188+2811535	-0.93	(-1.23, -0.83)	0.82	(0.50, 1.17)	-1.32	(-1.41, -1.02)	0.60	(-1.12, 0.81)	-1.08	(-1.34, -0.95)	0.81	(0.17, 1.12)
FM Tau	-0.33	(-0.50, -0.20)	0.15	(-0.18, 0.62)	-0.05	(-0.22, -0.01)	0.67	(0.29, 1.00)	-0.22	(-0.34, -0.11)	0.53	(0.27, 0.92)
FN Tau	-0.92	(-0.96, -0.79)	-1.57	(-2.41, -1.23)	-0.64	(-0.79, -0.45)	-1.30	(-1.93, -0.81)	-0.63	(-0.76, -0.57)	-1.11	(-1.55, -0.47)
CW Tau	0.02	(-0.13, 0.10)	-0.13	(-0.50, 0.27)	0.30	(0.21, 0.36)	0.46	(0.11, 0.80)	0.20	(0.13, 0.27)	0.35	(0.06, 0.68)
CIDA 1	-0.87	(-0.93, -0.76)	0.15	(-0.52, 0.25)	-1.04	(-1.08, -0.74)	0.10	(-2.09, 0.17)	-0.89	(-0.98, -0.75)	0.43	(-0.36, 0.48)
MHO 1	-0.71	(-0.76, -0.48)	-0.10	(-2.27, 0.54)	-0.20	(-0.40, -0.10)	-0.86	(-2.15, 0.46)	-0.45	(-0.54, -0.36)	-2.01	(-2.40, 0.41)
MHO 2 AB ^a	-0.49	(-0.54, -0.25)	-1.17	(-1.78, -0.50)	-0.09	(-0.21, 0.05)	-0.56	(-1.22, -0.06)	-0.32	(-0.38, -0.16)	-0.09	(-1.28, -0.08)
MHO 3 AB ^a	-0.12	(-0.25, 0.02)	-0.29	(-0.84, 0.22)	0.16	(0.08, 0.28)	0.50	(-0.01, 0.81)	0.06	(-0.06, 0.18)	0.28	(-0.01, 0.69)
FP Tau	-0.74	(-0.82, -0.64)	-0.09	(-0.88, -0.05)	-0.54	(-0.72, -0.40)	-0.10	(-0.69, 0.15)	-0.65	(-0.72, -0.53)	0.22	(-0.46, 0.29)
CX Tau	-0.66	(-0.71, -0.46)	-0.09	(-0.65, 0.13)	-0.31	(-0.46, -0.20)	0.25	(-0.22, 0.54)	-0.44	(-0.56, -0.36)	0.23	(0.06, 0.46)
FO Tau A	-0.70	(-0.79, -0.61)	-0.17	(-1.04, -0.15)	-0.42	(-0.60, -0.31)	-0.19	(-0.74, 0.12)	-0.59	(-0.65, -0.47)	0.13	(-0.58, 0.21)
FO Tau B	-0.72	(-0.78, -0.57)	-0.06	(-0.82, 0.08)	-0.45	(-0.63, -0.33)	0.02	(-0.55, 0.34)	-0.59	(-0.67, -0.47)	0.25	(-0.35, 0.40)
J04153916+2818586	-0.73	(-0.80, -0.61)	-0.08	(-0.83, 0.00)	-0.48	(-0.68, -0.37)	0.00	(-0.59, 0.24)	-0.63	(-0.70, -0.50)	0.23	(-0.38, 0.33)
IRAS 04125+2902	-0.39	(-0.54, -0.29)	0.13	(-0.08, 0.53)	-0.16	(-0.30, -0.10)	0.65	(0.33, 0.91)	-0.35	(-0.42, -0.24)	0.45	(0.29, 0.78)
J04155799+2746175	-0.89	(-0.96, -0.72)	0.31	(-0.19, 0.54)	-1.05	(-1.16, -0.78)	0.25	(-2.02, 0.36)	-0.98	(-1.06, -0.78)	0.56	(-0.17, 0.64)
J04161210+2756385	-0.74	(-0.87, -0.62)	0.36	(0.11, 0.72)	-1.05	(-1.16, -0.78)	0.32	(-1.05, 0.69)	-0.74	(-0.98, -0.65)	0.60	(0.12, 0.78)
J04163911+2858491	-0.80	(-0.98, -0.70)	0.45	(0.19, 0.77)	-1.09	(-1.21, -0.80)	0.35	(-1.76, 0.52)	-1.06	(-1.13, -0.79)	0.64	(-0.03, 0.78)
CY Tau	-0.44	(-0.62, -0.35)	-0.06	(-0.41, 0.31)	-0.18	(-0.31, -0.10)	0.45	(0.09, 0.74)	-0.36	(-0.44, -0.26)	0.30	(0.15, 0.61)
KPNO 10	-0.76	(-0.91, -0.65)	0.37	(0.12, 0.71)	-1.05	(-1.12, -0.66)	0.31	(-1.48, 0.61)	-0.97	(-1.03, -0.69)	0.61	(0.04, 0.77)
V410 X-ray 1	-0.72	(-0.84, -0.65)	-0.84	(-1.17, -0.24)	-0.49	(-0.68, -0.37)	-0.39	(-0.93, -0.03)	-0.61	(-0.68, -0.54)	0.11	(-0.70, 0.14)
V409 Tau	-0.40	(-0.54, -0.29)	0.27	(0.02, 0.68)	-0.20	(-0.34, -0.13)	0.70	(0.37, 0.98)	-0.37	(-0.45, -0.26)	0.54	(0.35, 0.87)
V410 Anon 13	-0.89	(-0.96, -0.78)	0.20	(-0.44, 0.32)	-1.05	(-1.13, -0.82)	0.14	(-2.27, 0.16)	-0.94	(-1.03, -0.80)	0.48	(-0.33, 0.52)
DD Tau A	-0.71	(-0.79, -0.57)	-0.06	(-0.96, 0.13)	-0.44	(-0.62, -0.32)	0.01	(-0.70, 0.36)	-0.57	(-0.66, -0.47)	0.24	(-0.54, 0.44)
DD Tau B	-0.72	(-0.78, -0.54)	0.00	(-0.76, 0.29)	-0.46	(-0.64, -0.33)	0.08	(-0.50, 0.51)	-0.57	(-0.67, -0.47)	0.34	(-0.28, 0.57)
CZ Tau A	-0.56	(-0.72, -0.43)	0.19	(-0.11, 0.60)	-0.41	(-0.57, -0.29)	0.49	(0.09, 0.83)	-0.50	(-0.61, -0.41)	0.48	(0.32, 0.78)
CZ Tau B	-1.22	(-1.36, -0.53)	0.37	(-1.75, 0.92)	-1.09	(-1.30, -0.54)	0.33	(-2.31, 0.86)	-1.13	(-1.33, -0.57)	0.56	(-0.97, 1.01)
V410 X-ray 2	-0.52	(-0.66, -0.42)	-1.54	(-1.97, -0.99)	0.05	(-0.11, 0.09)	-0.64	(-1.21, -0.20)	-0.30	(-0.39, -0.18)	-0.29	(-1.36, -0.26)
V892 Tau AB	0.82	(0.75, 1.10)	1.03	(0.32, 1.74)	1.42	(1.09, 1.69)	1.37	(-2.06, 1.66)	0.87	(0.78, 0.97)	1.66	(0.31, 1.70)
LR 1	-0.26	(-0.32, -0.03)	-0.48	(-0.95, -0.08)	0.22	(0.17, 0.29)	0.42	(-0.09, 0.61)	0.14	(0.01, 0.20)	0.13	(-0.12, 0.43)
V410 X-ray 7 AB ^a	-0.17	(-0.32, -0.05)	-0.10	(-0.55, 0.37)	0.06	(-0.08, 0.15)	0.49	(0.00, 0.80)	-0.07	(-0.18, 0.05)	0.31	(0.11, 0.73)
V410 X-ray 6	-0.89	(-0.95, -0.77)	-0.98	(-1.39, -0.49)	-0.76	(-0.93, -0.60)	-0.66	(-1.68, -0.32)	-0.70	(-0.82, -0.65)	-0.65	(-0.88, 0.06)
KPNO 12	-2.10	(-2.19, -1.69)	-0.25	(-2.18, 0.84)	-1.93	(-2.46, -1.67)	1.20	(-1.69, 1.23)	-2.09	(-2.36, -1.58)	0.81	(-0.26, 1.48)
FQ Tau A	-0.55	(-0.65, -0.39)	0.72	(0.41, 1.16)	-0.44	(-0.61, -0.32)	0.86	(0.54, 1.30)	-0.54	(-0.66, -0.44)	0.83	(0.64, 1.19)
FQ Tau B	-0.62	(-0.73, -0.47)	0.38	(0.12, 0.82)	-0.51	(-0.68, -0.37)	0.62	(0.19, 0.98)	-0.56	(-0.72, -0.48)	0.61	(0.44, 0.92)
BP Tau	-0.31	(-0.49, -0.22)	-0.31	(-0.79, 0.10)	0.06	(-0.04, 0.12)	0.47	(0.02, 0.75)	-0.10	(-0.23, 0.00)	0.23	(0.00, 0.61)
V819 Tau	-0.31	(-0.48, -0.21)	-0.28	(-0.63, 0.12)	0.06	(-0.04, 0.11)	0.52	(0.11, 0.76)	-0.11	(-0.23, 0.00)	0.26	(0.05, 0.62)
FR Tau	-0.87	(-0.92, -0.71)	0.20	(-0.36, 0.37)	-1.05	(-1.08, -0.70)	0.16	(-1.92, 0.31)	-0.91	(-0.99, -0.73)	0.49	(-0.23, 0.56)
J04201611+2821325	-0.99	(-1.35, -0.87)	0.85	(0.36, 1.25)	-1.39	(-1.47, -1.06)	0.65	(-1.06, 0.91)	-1.12	(-1.41, -0.97)	0.85	(0.16, 1.23)
J04202144+2813491 ^b	-0.37	(-0.58, -0.27)	0.52	(-0.84, 1.02)	-0.14	(-0.27, -0.05)	0.59	(-0.30, 1.11)	-0.34	(-0.43, -0.24)	0.61	(-0.30, 1.17)
J04202555+2700355	-0.78	(-0.93, -0.67)	0.58	(0.39, 0.94)	-1.15	(-1.21, -0.75)	0.45	(-1.28, 0.74)	-0.85	(-1.13, -0.75)	0.69	(0.19, 0.94)
IRAS 04173+2812	-0.66	(-0.77, -0.52)	0.43	(0.19, 0.86)	-0.59	(-0.84, -0.45)	0.58	(0.10, 0.96)	-0.63	(-0.83, -0.55)	0.64	(0.44, 0.92)
J04202606+2804089	-0.76	(-0.78, -0.49)	0.11	(-0.24, 0.43)	-0.49	(-0.67, -0.35)	0.30	(-0.06, 0.66)	-0.53	(-0.69, -0.46)	0.43	(0.26, 0.64)
J04210795+2702204	-0.78	(-0.94, -0.68)	0.44	(0.15, 0.79)	-1.05	(-1.17, -0.73)	0.35	(-1.62, 0.59)	-0.99	(-1.08, -0.74)	0.63	(0.00, 0.80)
J04210934+2750368	-0.87	(-0.92, -0.71)	0.21	(-0.36, 0.42)	-1.05	(-1.09, -0.70)	0.17	(-1.87, 0.33)	-0.91	(-1.00, -0.73)	0.49	(-0.23, 0.58)
J04213459+2701388	-0.87	(-0.93, -0.76)	0.16	(-0.50, 0.26)	-1.04	(-1.08, -0.74)	0.10	(-2.11, 0.18)	-0.90	(-0.98, -0.76)	0.44	(-0.35, 0.49)
IRAS 04187+1927	-0.49	(-0.61, -0.40)	-0.45	(-1.38, -0.43)	0.01	(-0.14, 0.07)	-0.05	(-0.67, 0.26)	-0.37	(-0.41, -0.12)	-0.12	(-0.76, 0.13)
J04214631+2659296	-0.84	(-1.07, -0.74)	0.71	(0.46, 1.05)	-1.20	(-1.32, -0.90)	0.51	(-1.32, 0.73)	-0.96	(-1.24, -0.85)	0.74	(0.13, 1.01)
DE Tau	-0.53	(-0.63, -0.47)	-0.97	(-1.21, -0.38)	-0.09	(-0.20, -0.01)	0.00	(-0.51, 0.24)	-0.41	(-0.45, -0.25)	-0.06	(-0.60, 0.10)
RY Tau	0.34	(0.21, 0.43)	-0.43	(-0.70, -0.16)	0.40	(0.36, 0.49)	-0.28	(-0.88, 0.21)	0.44	(0.37, 0.50)	0.00	(-0.21, 0.26)

Table 3—Continued

Name	DM97				BCAH98				SDF00			
	log M_*	CI(log M_*)	log t_*	CI(log t_*)	log M_*	CI(log M_*)	log t_*	CI(log t_*)	log M_*	CI(log M_*)	log t_*	CI(log t_*)
T Tau N	0.40	(0.31, 0.48)	-0.26	(-0.49, -0.01)	0.45	(0.41, 0.55)	0.20	(-0.65, 0.34)	0.44	(0.38, 0.50)	0.20	(-0.04, 0.41)
FS Tau A	-0.50	(-0.59, -0.36)	-0.37	(-1.22, -0.23)	0.00	(-0.16, 0.05)	0.14	(-0.51, 0.44)	-0.23	(-0.40, -0.11)	-0.03	(-0.49, 0.33)
FS Tau B	-0.62	(-0.75, -0.47)	0.32	(-0.01, 0.78)	-0.50	(-0.68, -0.36)	0.52	(0.09, 0.94)	-0.56	(-0.71, -0.48)	0.59	(0.37, 0.90)
J04221675+2654570	-0.42	(-0.58, -0.31)	0.11	(-0.15, 0.56)	-0.19	(-0.33, -0.11)	0.59	(0.24, 0.89)	-0.37	(-0.44, -0.26)	0.43	(0.25, 0.78)
IRAS 04196+2638	-0.39	(-0.55, -0.29)	0.04	(-0.23, 0.47)	-0.13	(-0.26, -0.07)	0.57	(0.24, 0.86)	-0.32	(-0.40, -0.22)	0.40	(0.21, 0.74)
J04230607+2801194	-0.85	(-1.08, -0.77)	0.47	(0.06, 0.74)	-1.16	(-1.28, -0.96)	0.37	(-1.99, 0.39)	-1.12	(-1.20, -0.90)	0.64	(-0.12, 0.73)
IRAS 04200+2759	-0.41	(-0.54, -0.32)	1.27	(0.74, 1.63)	-0.33	(-0.51, -0.26)	1.45	(0.93, 1.71)	-0.47	(-0.58, -0.37)	1.30	(0.93, 1.68)
J04231822+2641156	-0.75	(-0.78, -0.52)	0.03	(-0.49, 0.27)	-0.47	(-0.66, -0.35)	0.23	(-0.23, 0.53)	-0.53	(-0.69, -0.46)	0.36	(0.11, 0.54)
FU Tau A	-1.03	(-1.09, -0.86)	-1.06	(-2.03, -0.52)	-0.99	(-1.02, -0.72)	-0.77	(-2.32, -0.34)	-0.93	(-1.04, -0.74)	-0.84	(-1.38, -0.08)
FU Tau B	-1.76	(-1.81, -1.45)	-0.51	(-2.03, -0.52)	-1.70	(-2.24, -1.53)	-1.00	(-2.72, -0.31)	-1.86	(-2.08, -1.53)	0.62	(-0.72, 0.68)
FT Tau	-0.58	(-0.74, -0.22)	-0.15	(-1.10, 0.41)	-0.05	(-0.55, -0.02)	0.35	(-0.92, 0.70)	-0.14	(-0.58, -0.08)	0.21	(-0.59, 0.78)
J04242090+2630511	-0.97	(-1.32, -0.86)	0.79	(0.29, 1.18)	-1.37	(-1.46, -1.07)	0.61	(-1.30, 0.81)	-1.35	(-1.40, -0.97)	0.81	(0.08, 1.15)
J04242646+2649503	-0.84	(-1.06, -0.74)	0.69	(0.45, 1.03)	-1.20	(-1.31, -0.90)	0.50	(-1.35, 0.72)	-1.19	(-1.23, -0.84)	0.74	(0.11, 1.00)
IRAS 04216+2603	-0.28	(-0.51, -0.22)	0.81	(-0.22, 1.26)	-0.15	(-0.28, -0.05)	0.90	(0.16, 1.36)	-0.29	(-0.41, -0.19)	0.94	(0.26, 1.42)
IP Tau	-0.34	(-0.53, -0.21)	0.00	(-0.31, 0.51)	-0.05	(-0.21, 0.00)	0.62	(0.19, 0.93)	-0.22	(-0.34, -0.10)	0.44	(0.20, 0.85)
KPNO 3	-0.88	(-1.16, -0.78)	0.79	(0.50, 1.12)	-1.27	(-1.38, -0.97)	0.56	(-1.22, 0.79)	-1.02	(-1.30, -0.90)	0.79	(0.15, 1.08)
J04263055+2443558	-1.85	(-1.91, -1.48)	-0.25	(-2.23, 0.67)	-1.68	(-2.27, -1.54)	-2.36	(-2.45, 0.53)	-1.76	(-2.07, -1.44)	0.69	(-0.43, 1.04)
FV Tau A	-0.34	(-0.40, -0.08)	-0.51	(-1.16, -0.14)	0.18	(0.11, 0.26)	0.31	(-0.24, 0.57)	0.09	(-0.09, 0.16)	0.04	(-0.22, 0.40)
FV Tau B	-0.29	(-0.41, -0.21)	-0.38	(-0.86, -0.01)	0.12	(0.08, 0.18)	0.46	(0.09, 0.71)	-0.03	(-0.12, 0.05)	0.20	(-0.04, 0.55)
FV Tau/c A	-0.63	(-0.72, -0.53)	-0.22	(-1.00, -0.15)	-0.28	(-0.43, -0.18)	0.00	(-0.56, 0.28)	-0.52	(-0.57, -0.38)	0.09	(-0.50, 0.22)
FV Tau/c B	-0.60	(-0.70, -0.46)	0.82	(0.43, 1.30)	-0.53	(-0.72, -0.40)	0.85	(0.49, 1.35)	-0.61	(-0.76, -0.51)	0.86	(0.65, 1.29)
KPNO 13	-0.81	(-0.90, -0.73)	-0.69	(-0.99, -0.08)	-0.73	(-0.91, -0.56)	-0.26	(-1.23, -0.02)	-0.73	(-0.83, -0.64)	0.25	(-0.62, 0.26)
DF Tau AB ^a	-0.33	(-0.40, -0.26)	-1.21	(-1.69, -0.63)	0.09	(-0.01, 0.15)	-0.49	(-1.08, -0.06)	-0.16	(-0.21, -0.10)	-0.13	(-1.14, -0.12)
DG Tau	-0.36	(-0.43, -0.22)	-0.53	(-1.89, -0.14)	0.15	(0.08, 0.19)	0.35	(-0.79, 0.64)	-0.04	(-0.12, 0.07)	-0.09	(-0.85, 0.51)
J04284263+2714039 A	-0.78	(-0.94, -0.67)	0.50	(0.22, 0.89)	-1.07	(-1.18, -0.74)	0.39	(-1.50, 0.66)	-0.98	(-1.09, -0.74)	0.66	(0.05, 0.87)
J04284263+2714039 B	-1.52	(-1.56, -0.74)	0.57	(-1.69, 1.10)	-1.34	(-1.59, -0.84)	-0.18	(-2.45, 0.89)	-1.33	(-1.55, -0.76)	0.61	(-0.53, 1.21)
J04290068+2755033	-1.76	(-1.79, -1.24)	0.77	(-1.99, 0.88)	-1.54	(-2.02, -1.40)	-2.28	(-2.42, 0.60)	-1.60	(-1.85, -1.21)	0.69	(-0.34, 1.10)
IRAS 04260+2642 ^b	-0.18	(-0.38, -0.10)	-0.22	(-1.21, 0.65)	0.14	(0.01, 0.20)	0.60	(-0.22, 1.12)	-0.02	(-0.13, 0.08)	0.41	(-0.18, 1.03)
IRAS 04263+2654	-0.93	(-0.97, -0.81)	-1.57	(-2.41, -1.26)	-0.68	(-0.83, -0.49)	-1.30	(-1.98, -0.85)	-0.65	(-0.78, -0.58)	-1.10	(-1.51, -0.52)
XEST 13-010	-0.66	(-0.76, -0.57)	-0.19	(-1.04, -0.15)	-0.34	(-0.51, -0.24)	-0.10	(-0.68, 0.20)	-0.55	(-0.60, -0.43)	0.10	(-0.58, 0.21)
DH Tau A	-0.56	(-0.59, -0.35)	-0.18	(-0.69, 0.15)	-0.12	(-0.24, -0.05)	0.40	(-0.02, 0.66)	-0.32	(-0.40, -0.22)	0.20	(0.04, 0.53)
DH Tau B	-2.04	(-2.06, -1.30)	1.41	(-1.88, 1.64)	-1.26	(-1.84, -1.21)	1.20	(0.10, 1.78)	-1.35	(-1.94, -1.27)	1.47	(0.22, 1.78)
IQ Tau	-0.53	(-0.60, -0.37)	-0.30	(-1.01, -0.11)	-0.05	(-0.19, 0.01)	0.25	(-0.30, 0.52)	-0.27	(-0.41, -0.16)	0.06	(-0.16, 0.40)
J04295950+2433078	-0.81	(-0.89, -0.73)	-0.63	(-0.91, -0.04)	-0.74	(-0.92, -0.57)	-0.18	(-1.21, 0.02)	-0.74	(-0.84, -0.65)	0.28	(-0.57, 0.29)
UX Tau A	0.10	(-0.04, 0.16)	0.22	(-0.15, 0.54)	0.31	(0.15, 0.37)	0.71	(0.43, 1.05)	0.20	(0.13, 0.26)	0.66	(0.35, 0.95)
KPNO 6	-1.90	(-1.96, -1.50)	-0.04	(-2.15, 0.85)	-1.69	(-2.18, -1.51)	1.03	(-2.05, 0.97)	-1.81	(-2.01, -1.37)	0.76	(-0.26, 1.28)
FX Tau A	-0.54	(-0.59, -0.32)	-0.15	(-0.79, 0.39)	-0.12	(-0.24, -0.05)	0.41	(-0.13, 0.76)	-0.32	(-0.41, -0.22)	0.24	(-0.03, 0.68)
FX Tau B	-0.75	(-0.83, -0.64)	-0.10	(-1.01, -0.04)	-0.51	(-0.71, -0.39)	-0.14	(-0.82, 0.14)	-0.62	(-0.72, -0.53)	0.20	(-0.58, 0.30)
DK Tau A	-0.46	(-0.54, -0.30)	-0.41	(-1.27, -0.18)	0.06	(-0.07, 0.12)	0.25	(-0.43, 0.55)	-0.15	(-0.31, -0.03)	0.00	(-0.36, 0.42)
DK Tau B	-0.38	(-0.53, -0.26)	0.33	(-0.21, 0.83)	-0.15	(-0.27, -0.07)	0.66	(0.22, 1.04)	-0.33	(-0.41, -0.22)	0.54	(0.23, 0.99)
ZZ Tau AB ^a	-0.42	(-0.48, -0.23)	-0.07	(-0.74, 0.12)	-0.21	(-0.33, -0.06)	0.16	(-0.39, 0.46)	-0.31	(-0.39, -0.18)	0.24	(-0.16, 0.44)
ZZ Tau IRS	-0.85	(-0.90, -0.66)	0.27	(-0.19, 0.56)	-1.05	(-1.09, -0.65)	0.22	(-1.56, 0.49)	-0.91	(-1.00, -0.69)	0.55	(-0.11, 0.67)
KPNO 7	-1.82	(-1.87, -1.30)	0.85	(-2.00, 0.99)	-1.61	(-2.07, -1.40)	0.89	(-2.23, 0.86)	-1.70	(-1.90, -1.23)	0.74	(-0.27, 1.28)
JH 56	-0.36	(-0.53, -0.25)	0.01	(-0.21, 0.44)	-0.06	(-0.23, -0.03)	0.61	(0.27, 0.89)	-0.27	(-0.37, -0.15)	0.41	(0.23, 0.78)
XZ Tau A	-0.59	(-0.66, -0.37)	-0.02	(-0.71, 0.55)	-0.24	(-0.38, -0.14)	0.41	(-0.26, 0.79)	-0.42	(-0.51, -0.32)	0.33	(-0.12, 0.76)
XZ Tau B	-0.72	(-0.82, -0.61)	-0.91	(-1.54, -0.19)	-0.40	(-0.58, -0.28)	-0.44	(-1.19, 0.03)	-0.55	(-0.63, -0.48)	0.05	(-1.08, 0.13)
HK Tau A	-0.37	(-0.55, -0.26)	-0.03	(-0.32, 0.47)	-0.06	(-0.23, -0.03)	0.56	(0.19, 0.88)	-0.27	(-0.37, -0.15)	0.40	(0.18, 0.79)
HK Tau B ^b	-0.46	(-0.64, -0.34)	0.36	(-0.68, 1.02)	-0.25	(-0.41, -0.15)	0.57	(-0.36, 1.13)	-0.43	(-0.52, -0.33)	0.61	(-0.32, 1.17)
V710 Tau A	-0.54	(-0.58, -0.30)	-0.18	(-0.67, 0.22)	-0.05	(-0.22, -0.01)	0.42	(-0.01, 0.73)	-0.27	(-0.38, -0.15)	0.24	(0.05, 0.63)
LkH α 267 ^b	-0.56	(-0.71, -0.42)	0.22	(0.00, 0.62)	-0.42	(-0.57, -0.29)	0.50	(0.16, 0.85)	-0.50	(-0.61, -0.42)	0.51	(0.36, 0.78)

Table 3—Continued

Name	DM97				BCAH98				SDF00			
	log M_*	CI(log M_*)	log t_*	CI(log t_*)	log M_*	CI(log M_*)	log t_*	CI(log t_*)	log M_*	CI(log M_*)	log t_*	CI(log t_*)
Haro 6-13	-0.53	(-0.57, -0.28)	-0.25	(-0.79, 0.14)	-0.01	(-0.19, 0.03)	0.40	(-0.11, 0.70)	-0.22	(-0.35, -0.10)	0.20	(0.00, 0.61)
MHO 5	-0.88	(-0.96, -0.82)	-0.49	(-0.73, 0.08)	-1.03	(-1.07, -0.80)	-0.13	(-2.36, -0.06)	-0.88	(-0.98, -0.78)	0.34	(-0.54, 0.34)
MHO 6	-0.73	(-0.86, -0.62)	0.43	(0.18, 0.82)	-1.05	(-1.08, -0.60)	0.37	(-0.95, 0.76)	-0.75	(-0.99, -0.65)	0.63	(0.19, 0.85)
J04322415+2251083	-0.72	(-0.84, -0.59)	0.34	(0.13, 0.69)	-0.66	(-1.02, -0.54)	0.32	(-0.57, 0.74)	-0.68	(-0.94, -0.61)	0.59	(0.24, 0.78)
GG Tau Aab ^a	-0.08	(-0.19, 0.01)	-0.24	(-0.62, 0.22)	0.29	(0.21, 0.34)	0.58	(0.12, 0.82)	0.13	(0.04, 0.20)	0.32	(0.06, 0.68)
GG Tau Ba	-0.87	(-0.94, -0.76)	0.17	(-0.50, 0.30)	-1.04	(-1.09, -0.74)	0.11	(-2.09, 0.20)	-0.90	(-0.99, -0.76)	0.44	(-0.34, 0.51)
GG Tau Bb	-1.65	(-1.66, -0.99)	0.65	(-1.32, 0.97)	-1.43	(-1.72, -1.23)	0.61	(-2.35, 0.59)	-1.45	(-1.60, -1.05)	0.70	(-0.24, 1.06)
FY Tau	-0.21	(-0.39, -0.06)	-0.37	(-0.80, 0.12)	0.16	(0.09, 0.23)	0.46	(0.06, 0.73)	0.07	(-0.09, 0.13)	0.25	(-0.05, 0.58)
FZ Tau	-0.50	(-0.60, -0.38)	-0.41	(-1.33, -0.33)	0.01	(-0.15, 0.06)	0.03	(-0.61, 0.36)	-0.35	(-0.41, -0.12)	-0.08	(-0.68, 0.23)
UZ Tau Wa	-0.46	(-0.65, -0.37)	0.00	(-0.35, 0.40)	-0.25	(-0.39, -0.15)	0.45	(0.06, 0.76)	-0.41	(-0.49, -0.31)	0.34	(0.18, 0.65)
UZ Tau Wb	-0.56	(-0.73, -0.43)	0.13	(-0.15, 0.50)	-0.41	(-0.57, -0.29)	0.40	(0.06, 0.76)	-0.50	(-0.60, -0.41)	0.44	(0.30, 0.70)
UZ Tau Eab ^a	-0.32	(-0.37, -0.19)	-0.24	(-1.02, 0.20)	0.03	(-0.07, 0.10)	0.31	(-0.33, 0.64)	-0.15	(-0.22, -0.07)	0.12	(-0.31, 0.55)
JH 112 Aa	-0.26	(-0.38, -0.18)	-0.26	(-0.55, 0.14)	0.11	(0.06, 0.16)	0.60	(0.25, 0.80)	-0.02	(-0.12, 0.04)	0.35	(0.07, 0.64)
JH 112 Ab	-1.87	(-1.93, -1.26)	0.96	(-2.05, 1.19)	-1.68	(-2.31, -1.41)	-2.51	(-2.38, 1.00)	-1.79	(-2.12, -1.24)	0.70	(-0.43, 1.38)
J04324938+2253082	-0.75	(-0.86, -0.66)	-0.89	(-1.26, -0.28)	-0.54	(-0.73, -0.40)	-0.47	(-1.06, -0.09)	-0.62	(-0.71, -0.55)	0.10	(-0.77, 0.12)
GH Tau A	-0.47	(-0.66, -0.39)	-0.03	(-0.41, 0.30)	-0.25	(-0.39, -0.15)	0.43	(0.03, 0.70)	-0.40	(-0.49, -0.31)	0.30	(0.16, 0.59)
GH Tau B	-0.61	(-0.67, -0.40)	-0.08	(-0.61, 0.23)	-0.24	(-0.38, -0.14)	0.35	(-0.11, 0.64)	-0.40	(-0.50, -0.31)	0.25	(0.08, 0.54)
V807 Tau A	-0.43	(-0.51, -0.28)	-0.44	(-1.26, -0.24)	0.08	(-0.02, 0.15)	0.25	(-0.37, 0.53)	-0.10	(-0.26, 0.01)	-0.03	(-0.29, 0.38)
J04330945+2246487	-0.85	(-1.07, -0.77)	0.45	(0.02, 0.70)	-1.16	(-1.27, -0.95)	0.35	(-2.03, 0.36)	-1.11	(-1.19, -0.90)	0.63	(-0.13, 0.71)
IRAS 04301+2608 ^b	-0.27	(-0.55, -0.21)	0.60	(-1.01, 1.03)	-0.05	(-0.23, 0.02)	0.61	(-0.34, 1.16)	-0.25	(-0.38, -0.13)	0.68	(-0.29, 1.22)
IRAS 04303+2240	-0.48	(-0.61, -0.41)	-1.09	(-1.40, -0.47)	0.01	(-0.14, 0.07)	-0.10	(-0.70, 0.22)	-0.37	(-0.41, -0.12)	-0.13	(-0.79, 0.08)
J04333278+1800436	-0.30	(-0.46, -0.22)	0.65	(0.31, 0.98)	-0.16	(-0.30, -0.12)	0.97	(0.64, 1.23)	-0.33	(-0.41, -0.22)	0.80	(0.57, 1.13)
GI Tau	-0.44	(-0.50, -0.23)	-0.36	(-1.00, 0.04)	0.07	(-0.04, 0.13)	0.45	(-0.14, 0.71)	-0.10	(-0.24, 0.00)	0.17	(-0.10, 0.58)
GK Tau	-0.43	(-0.51, -0.25)	-0.42	(-1.29, -0.08)	0.08	(-0.03, 0.14)	0.33	(-0.38, 0.63)	-0.11	(-0.26, 0.00)	0.04	(-0.31, 0.51)
IS Tau A	-0.35	(-0.56, -0.25)	-0.15	(-0.53, 0.29)	-0.04	(-0.20, 0.02)	0.50	(0.06, 0.80)	-0.22	(-0.34, -0.10)	0.30	(0.11, 0.71)
IS Tau B	-0.62	(-0.72, -0.46)	0.43	(0.22, 0.83)	-0.51	(-0.68, -0.37)	0.64	(0.27, 1.00)	-0.57	(-0.71, -0.48)	0.64	(0.49, 0.92)
DL Tau	-0.28	(-0.46, -0.17)	-0.15	(-0.57, 0.40)	0.04	(-0.06, 0.10)	0.60	(0.15, 0.92)	-0.09	(-0.23, -0.01)	0.41	(0.09, 0.80)
J04333905+2227207	-0.35	(-0.51, -0.30)	1.33	(0.94, 1.64)	-0.29	(-0.47, -0.26)	1.46	(1.10, 1.73)	-0.44	(-0.55, -0.35)	1.34	(1.05, 1.67)
HN Tau A	-0.09	(-0.27, -0.05)	0.48	(-0.22, 1.07)	0.07	(-0.08, 0.15)	0.85	(0.43, 1.54)	-0.04	(-0.14, 0.05)	0.73	(0.31, 1.37)
HN Tau B	-0.65	(-0.78, -0.53)	1.25	(0.81, 1.64)	-0.68	(-0.90, -0.52)	1.12	(0.68, 1.57)	-0.72	(-0.89, -0.61)	1.11	(0.86, 1.59)
J04334171+1750402	-0.67	(-0.80, -0.53)	0.27	(0.05, 0.63)	-0.58	(-0.83, -0.44)	0.39	(-0.04, 0.77)	-0.61	(-0.83, -0.53)	0.55	(0.35, 0.76)
J04334465+2615005	-0.79	(-0.88, -0.71)	-0.66	(-0.94, -0.06)	-0.70	(-0.87, -0.52)	-0.19	(-1.03, 0.03)	-0.71	(-0.81, -0.62)	0.25	(-0.57, 0.28)
DM Tau	-0.31	(-0.47, -0.23)	0.48	(0.21, 0.83)	-0.15	(-0.29, -0.11)	0.89	(0.57, 1.13)	-0.33	(-0.41, -0.22)	0.70	(0.49, 1.01)
CI Tau	-0.31	(-0.49, -0.21)	-0.29	(-0.76, 0.15)	0.06	(-0.04, 0.11)	0.49	(0.04, 0.78)	-0.10	(-0.23, 0.00)	0.25	(0.01, 0.64)
J04335245+2612548	-1.94	(-2.01, -1.52)	0.03	(-2.16, 0.89)	-1.73	(-2.17, -1.49)	1.10	(-1.87, 1.11)	-1.86	(-2.05, -1.38)	0.81	(-0.21, 1.38)
IT Tau A	0.02	(-0.11, 0.08)	0.22	(-0.14, 0.52)	0.23	(0.12, 0.29)	0.71	(0.50, 1.07)	0.15	(0.09, 0.20)	0.66	(0.36, 0.93)
IT Tau B	-0.77	(-0.82, -0.59)	0.05	(-0.65, 0.30)	-0.55	(-0.76, -0.42)	0.07	(-0.51, 0.46)	-0.63	(-0.77, -0.53)	0.37	(-0.22, 0.56)
AA Tau	-0.33	(-0.48, -0.19)	-0.30	(-0.94, 0.33)	0.06	(-0.05, 0.12)	0.50	(-0.08, 0.86)	-0.10	(-0.24, -0.01)	0.31	(-0.06, 0.77)
HO Tau	-0.21	(-0.42, -0.19)	0.98	(0.60, 1.30)	-0.18	(-0.31, -0.14)	1.21	(0.87, 1.51)	-0.25	(-0.41, -0.21)	1.12	(0.82, 1.45)
DN Tau	-0.53	(-0.58, -0.31)	-0.29	(-0.88, -0.01)	0.00	(-0.18, 0.04)	0.33	(-0.18, 0.62)	-0.22	(-0.36, -0.09)	0.12	(-0.05, 0.51)
CoKu Tau/3 A	-0.55	(-0.60, -0.37)	-0.22	(-0.78, 0.05)	-0.12	(-0.23, -0.04)	0.35	(-0.09, 0.61)	-0.32	(-0.41, -0.22)	0.15	(0.00, 0.47)
CoKu Tau/3 B	-0.82	(-0.92, -0.48)	0.07	(-0.83, 0.42)	-0.78	(-0.85, -0.36)	0.05	(-0.57, 0.59)	-0.79	(-0.92, -0.51)	0.35	(-0.63, 0.54)
HQ Tau	0.15	(-0.04, 0.21)	-0.13	(-0.46, 0.16)	0.37	(0.29, 0.43)	0.45	(0.10, 0.71)	0.28	(0.21, 0.33)	0.34	(0.08, 0.58)
HP Tau	0.01	(-0.12, 0.10)	0.04	(-0.29, 0.34)	0.27	(0.18, 0.33)	0.60	(0.38, 0.89)	0.18	(0.12, 0.23)	0.50	(0.23, 0.76)
Haro 6-28 A	-0.46	(-0.59, -0.32)	0.28	(0.03, 0.72)	-0.27	(-0.42, -0.18)	0.68	(0.32, 0.98)	-0.42	(-0.50, -0.31)	0.55	(0.37, 0.88)
Haro 6-28 B	-0.66	(-0.76, -0.49)	0.20	(-0.28, 0.65)	-0.49	(-0.67, -0.36)	0.40	(-0.09, 0.83)	-0.56	(-0.70, -0.47)	0.52	(0.24, 0.82)
J04361030+2159364	-1.88	(-1.93, -1.48)	-0.04	(-2.15, 0.83)	-1.67	(-2.18, -1.51)	0.96	(-2.14, 0.88)	-1.78	(-2.00, -1.36)	0.75	(-0.28, 1.22)
J04362151+2351165	-0.81	(-1.02, -0.70)	1.16	(0.84, 1.52)	-0.95	(-1.25, -0.78)	0.91	(0.41, 1.37)	-0.94	(-1.13, -0.79)	1.04	(0.87, 1.49)
ITG 1	-0.82	(-1.13, -0.71)	1.70	(1.01, 1.83)	-0.87	(-1.20, -0.74)	1.56	(0.83, 1.79)	-0.88	(-1.16, -0.77)	1.63	(1.08, 1.83)
J04381486+2611399	-1.52	(-1.78, -1.09)	1.02	(-0.65, 1.49)	-1.56	(-1.69, -1.12)	0.98	(-0.83, 1.45)	-1.23	(-1.70, -1.09)	1.04	(0.13, 1.63)

Table 3—Continued

Name	DM97				BCAH98				SDF00			
	log M_*	CI(log M_*)	log t_*	CI(log t_*)	log M_*	CI(log M_*)	log t_*	CI(log t_*)	log M_*	CI(log M_*)	log t_*	CI(log t_*)
GM Tau	-0.91	(-1.21, -0.83)	0.55	(0.00, 0.84)	-1.23	(-1.39, -1.08)	0.45	(-2.01, 0.41)	-1.23	(-1.31, -0.99)	0.67	(-0.13, 0.80)
DO Tau	-0.50	(-0.61, -0.39)	-0.43	(-1.49, -0.36)	0.01	(-0.15, 0.07)	-0.03	(-0.75, 0.32)	-0.33	(-0.40, -0.12)	-0.11	(-0.89, 0.19)
HV Tau C ^b	-0.34	(-0.39, -0.13)	-0.29	(-1.14, 0.61)	0.12	(0.02, 0.17)	0.60	(-0.14, 1.08)	-0.04	(-0.13, 0.03)	0.43	(-0.12, 0.99)
J04385859+2336351	-0.68	(-0.80, -0.55)	0.56	(0.23, 1.05)	-0.65	(-0.94, -0.50)	0.65	(-0.02, 1.04)	-0.68	(-0.89, -0.59)	0.69	(0.44, 1.05)
J04390163+2336029	-0.92	(-0.99, -0.80)	0.24	(-0.37, 0.34)	-1.05	(-1.17, -0.89)	0.19	(-2.38, 0.13)	-0.99	(-1.07, -0.86)	0.51	(-0.31, 0.53)
J04390396+2544264	-1.11	(-1.36, -0.91)	0.40	(-0.97, 0.52)	-1.19	(-1.39, -1.05)	-1.15	(-2.52, 0.14)	-1.18	(-1.34, -1.00)	0.58	(-0.44, 0.62)
VY Tau A	-0.28	(-0.45, -0.17)	0.34	(0.03, 0.77)	-0.07	(-0.24, -0.04)	0.85	(0.45, 1.11)	-0.22	(-0.35, -0.12)	0.68	(0.41, 1.03)
VY Tau B	-0.67	(-0.99, -0.45)	0.39	(-0.18, 1.07)	-1.06	(-1.17, -0.50)	0.33	(-1.96, 0.93)	-1.01	(-1.08, -0.53)	0.59	(-0.14, 1.04)
LkCa 15	-0.15	(-0.30, -0.04)	0.16	(-0.26, 0.61)	0.09	(0.02, 0.16)	0.71	(0.40, 1.10)	0.02	(-0.11, 0.08)	0.57	(0.24, 0.94)
GN Tau A	-0.64	(-0.71, -0.50)	-0.16	(-0.88, -0.01)	-0.29	(-0.44, -0.19)	0.14	(-0.46, 0.41)	-0.48	(-0.56, -0.37)	0.14	(-0.35, 0.35)
GN Tau B	-0.68	(-0.75, -0.42)	-0.10	(-0.80, 0.16)	-0.33	(-0.57, -0.18)	0.21	(-0.52, 0.55)	-0.59	(-0.63, -0.31)	0.22	(-0.27, 0.51)
J04393364+2359212	-0.86	(-0.91, -0.66)	0.28	(-0.15, 0.56)	-1.05	(-1.09, -0.65)	0.23	(-1.58, 0.50)	-0.92	(-1.00, -0.69)	0.55	(-0.09, 0.67)
ITG 15	-0.88	(-0.94, -0.74)	-1.16	(-1.72, -0.71)	-0.67	(-0.84, -0.49)	-0.85	(-1.57, -0.41)	-0.65	(-0.76, -0.59)	-0.78	(-1.05, -0.06)
CFHT 4	-0.94	(-1.06, -0.85)	-0.72	(-1.24, -0.13)	-1.02	(-1.08, -0.82)	-0.46	(-2.51, -0.24)	-0.90	(-1.04, -0.79)	-0.63	(-0.88, 0.17)
J04400067+2358211	-0.86	(-1.13, -0.78)	0.67	(0.36, 1.03)	-1.21	(-1.35, -0.97)	0.50	(-1.57, 0.64)	-1.18	(-1.27, -0.90)	0.73	(0.02, 0.98)
IRAS 04370+2559	-0.55	(-0.76, -0.27)	-0.31	(-1.45, -0.01)	-0.05	(-0.49, 0.02)	0.00	(-1.21, 0.43)	-0.50	(-0.57, -0.06)	0.02	(-0.96, 0.47)
J04403979+2519061 AB ^a	-0.68	(-0.76, -0.42)	0.25	(-0.25, 0.48)	-0.79	(-0.86, -0.46)	0.20	(-1.88, 0.38)	-0.74	(-0.81, -0.46)	0.53	(-0.17, 0.62)
JH 223 A	-0.46	(-0.59, -0.32)	0.25	(0.03, 0.66)	-0.27	(-0.41, -0.17)	0.61	(0.32, 0.94)	-0.42	(-0.49, -0.31)	0.52	(0.36, 0.84)
JH 223 B	-1.31	(-1.46, -0.73)	0.66	(-0.48, 1.32)	-1.37	(-1.55, -0.88)	0.59	(-2.09, 1.03)	-1.36	(-1.44, -0.78)	0.76	(-0.05, 1.37)
ITG 33A ^b	-0.65	(-0.73, -0.45)	0.08	(-0.71, 0.71)	-0.39	(-0.56, -0.27)	0.34	(-0.43, 0.87)	-0.52	(-0.62, -0.43)	0.47	(-0.24, 0.90)
ITG 34	-0.80	(-0.98, -0.70)	0.52	(0.26, 0.88)	-1.15	(-1.23, -0.81)	0.40	(-1.63, 0.60)	-1.06	(-1.14, -0.79)	0.66	(0.02, 0.86)
CoKu Tau/4 AB ^a	-0.14	(-0.27, -0.03)	0.11	(-0.11, 0.53)	0.04	(-0.09, 0.13)	0.59	(0.27, 0.88)	-0.06	(-0.18, 0.03)	0.43	(0.27, 0.76)
ITG 40	-0.72	(-0.78, -0.53)	0.02	(-0.73, 0.33)	-0.46	(-0.64, -0.33)	0.14	(-0.48, 0.54)	-0.57	(-0.68, -0.47)	0.36	(-0.24, 0.60)
IRAS 04385+2550	-0.32	(-0.48, -0.19)	0.23	(-0.10, 0.64)	-0.05	(-0.23, -0.02)	0.75	(0.36, 1.03)	-0.22	(-0.34, -0.11)	0.59	(0.32, 0.94)
J04414489+2301513	-1.82	(-1.88, -1.43)	-0.11	(-2.15, 0.75)	-1.63	(-2.14, -1.49)	-1.97	(-2.36, 0.60)	-1.71	(-1.95, -1.37)	0.71	(-0.35, 1.07)
J04414825+2534304	-1.57	(-1.61, -0.99)	0.58	(-1.68, 0.78)	-1.40	(-1.68, -1.17)	-1.05	(-2.54, 0.43)	-1.38	(-1.59, -1.07)	0.64	(-0.42, 0.88)
V955 Tau A	-0.45	(-0.49, -0.22)	-0.34	(-0.89, 0.06)	0.06	(-0.04, 0.12)	0.46	(-0.04, 0.72)	-0.10	(-0.23, 0.01)	0.19	(-0.04, 0.58)
V955 Tau B	-0.65	(-0.71, -0.46)	-0.09	(-0.72, 0.14)	-0.31	(-0.46, -0.20)	0.23	(-0.29, 0.53)	-0.45	(-0.56, -0.36)	0.19	(-0.04, 0.46)
CIDA 7	-0.84	(-0.88, -0.65)	0.17	(-0.35, 0.40)	-0.89	(-1.01, -0.58)	0.15	(-1.07, 0.44)	-0.85	(-0.93, -0.64)	0.48	(-0.16, 0.59)
DP Tau A	-0.28	(-0.47, -0.20)	0.61	(0.05, 1.03)	-0.13	(-0.27, -0.07)	0.89	(0.42, 1.24)	-0.27	(-0.39, -0.17)	0.77	(0.41, 1.20)
DP Tau B	-0.42	(-0.64, -0.28)	0.50	(0.03, 1.04)	-0.26	(-0.52, -0.18)	0.75	(0.19, 0.19)	-0.42	(-0.56, -0.27)	0.69	(0.40, 1.20)
GO Tau	-0.27	(-0.44, -0.17)	0.47	(0.08, 0.88)	-0.09	(-0.25, -0.04)	0.89	(0.48, 1.18)	-0.20	(-0.35, -0.12)	0.75	(0.44, 1.11)
CIDA 14	-0.81	(-0.89, -0.73)	-0.63	(-0.92, -0.02)	-0.74	(-0.93, -0.57)	-0.18	(-1.23, 0.02)	-0.74	(-0.84, -0.65)	0.28	(-0.57, 0.29)
IRAS 04414+2506	-1.03	(-1.30, -0.90)	0.32	(-1.05, 0.38)	-1.15	(-1.32, -1.00)	-1.24	(-2.55, 0.06)	-1.12	(-1.27, -0.95)	0.55	(-0.55, 0.56)
IRAS 04429+1550	-0.51	(-0.68, -0.39)	0.10	(-0.13, 0.46)	-0.34	(-0.48, -0.22)	0.45	(0.13, 0.78)	-0.45	(-0.54, -0.36)	0.41	(0.28, 0.68)
DQ Tau AB ^a	-0.01	(-0.14, 0.07)	0.18	(-0.23, 0.68)	0.21	(0.12, 0.27)	0.66	(0.25, 1.02)	0.09	(0.00, 0.16)	0.55	(0.25, 0.96)
Haro 6-37 A	-0.28	(-0.46, -0.18)	-0.16	(-0.52, 0.33)	0.05	(-0.06, 0.10)	0.60	(0.17, 0.89)	-0.09	(-0.23, -0.01)	0.39	(0.10, 0.76)
Haro 6-37 B	-0.81	(-0.97, -0.36)	0.09	(-1.01, 0.63)	-0.71	(-0.83, -0.25)	0.05	(-0.53, 0.81)	-0.80	(-0.96, -0.36)	0.36	(-0.78, 0.75)
Haro 6-37 C	-0.37	(-0.51, -0.26)	0.28	(-0.05, 0.70)	-0.14	(-0.27, -0.08)	0.70	(0.36, 1.00)	-0.32	(-0.40, -0.22)	0.53	(0.31, 0.90)
DR Tau	-0.34	(-0.39, -0.07)	-0.43	(-0.95, 0.04)	0.17	(0.10, 0.24)	0.45	(-0.05, 0.68)	0.08	(-0.09, 0.14)	0.17	(-0.11, 0.52)
DS Tau	-0.14	(-0.29, -0.04)	0.21	(-0.21, 0.64)	0.08	(0.02, 0.15)	0.75	(0.45, 1.13)	0.02	(-0.11, 0.07)	0.61	(0.27, 0.97)
UY Aur A	-0.51	(-0.59, -0.34)	-0.35	(-1.18, -0.15)	0.00	(-0.17, 0.05)	0.19	(-0.46, 0.50)	-0.23	(-0.39, -0.11)	0.01	(-0.39, 0.40)
UY Aur B	-0.63	(-0.72, -0.51)	-0.18	(-1.00, -0.02)	-0.28	(-0.43, -0.18)	0.10	(-0.59, 0.37)	-0.49	(-0.56, -0.38)	0.11	(-0.56, 0.32)
St 34 AB ^a	-0.26	(-0.30, -0.12)	0.79	(0.51, 1.19)	-0.14	(-0.26, -0.06)	0.96	(0.63, 1.33)	-0.26	(-0.33, -0.17)	0.88	(0.70, 1.21)
St 34 C	-0.85	(-1.08, -0.74)	1.10	(0.78, 1.48)	-1.00	(-1.32, -0.83)	0.89	(0.03, 1.30)	-0.97	(-1.18, -0.83)	1.02	(0.83, 1.45)
GM Aur	0.03	(-0.10, 0.08)	0.33	(-0.02, 0.60)	0.17	(0.09, 0.25)	0.85	(0.62, 1.17)	0.13	(0.08, 0.18)	0.75	(0.47, 1.01)
J04554535+3019389	-0.73	(-0.86, -0.61)	0.39	(0.22, 0.74)	-1.05	(-1.08, -0.60)	0.34	(-1.04, 0.72)	-0.72	(-1.00, -0.65)	0.61	(0.21, 0.81)
AB Aur	0.36	(0.30, 0.42)	1.29	(0.79, 1.79)	0.32	(0.28, 0.79)	1.36	(0.77, 1.85)	0.36	(0.31, 0.44)	1.32	(0.78, 1.80)
J04554801+3028050	-0.85	(-1.07, -0.73)	1.08	(0.77, 1.46)	-1.00	(-1.32, -0.83)	0.87	(-0.01, 1.27)	-0.97	(-1.18, -0.82)	0.98	(0.83, 1.42)
J04554969+3019400	-0.89	(-1.17, -0.79)	0.83	(0.53, 1.17)	-1.28	(-1.39, -0.96)	0.59	(-1.10, 0.85)	-1.03	(-1.30, -0.90)	0.81	(0.22, 1.13)

Table 3—Continued

Name	DM97				BCAH98				SDF00			
	$\log M_*$	CI($\log M_*$)	$\log t_*$	CI($\log t_*$)	$\log M_*$	CI($\log M_*$)	$\log t_*$	CI($\log t_*$)	$\log M_*$	CI($\log M_*$)	$\log t_*$	CI($\log t_*$)
XEST 26-062	-0.76	(-0.82, -0.62)	-0.03	(-0.76, 0.08)	-0.54	(-0.74, -0.41)	0.02	(-0.59, 0.28)	-0.65	(-0.75, -0.53)	0.30	(-0.35, 0.40)
SU Aur	0.40	(0.30, 0.47)	-0.04	(-0.32, 0.29)	0.54	(0.44, 0.64)	0.43	(-0.19, 0.65)	0.40	(0.30, 0.45)	0.46	(0.14, 0.70)
XEST 26-071	-0.62	(-0.73, -0.46)	0.37	(0.15, 0.78)	-0.51	(-0.68, -0.37)	0.60	(0.21, 0.95)	-0.56	(-0.71, -0.48)	0.60	(0.45, 0.88)
MWC 480	0.26	(0.24, 0.31)	1.20	(0.84, 1.80)	0.26	(0.23, 0.35)	1.36	(1.35, 1.88)	0.28	(0.26, 0.32)	0.85	(0.92, 1.82)
V836 Tau	-0.25	(-0.39, -0.14)	0.11	(-0.21, 0.55)	0.02	(-0.07, 0.07)	0.78	(0.38, 1.03)	-0.08	(-0.23, -0.02)	0.57	(0.26, 0.89)
CIDA 8	-0.76	(-0.78, -0.50)	0.09	(-0.34, 0.39)	-0.48	(-0.67, -0.35)	0.28	(-0.12, 0.63)	-0.53	(-0.69, -0.46)	0.41	(0.21, 0.62)
CIDA 9 A	-0.21	(-0.33, -0.16)	1.19	(0.72, 1.68)	-0.18	(-0.25, -0.09)	1.41	(1.01, 1.81)	-0.21	(-0.35, -0.16)	1.38	(0.95, 1.76)
CIDA 9 B	-0.37	(-0.64, -0.26)	1.02	(0.23, 1.51)	-0.28	(-0.65, -0.20)	1.13	(0.25, 1.55)	-0.41	(-0.64, -0.27)	1.12	(0.56, 1.61)
CIDA 11 AB ^a	-0.35	(-0.45, -0.21)	0.38	(0.15, 0.80)	-0.30	(-0.47, -0.17)	0.61	(0.21, 0.97)	-0.38	(-0.48, -0.25)	0.61	(0.45, 0.90)
RW Aur A	0.08	(-0.12, 0.14)	0.13	(-0.31, 0.49)	0.26	(0.15, 0.34)	0.60	(0.30, 0.97)	0.18	(0.08, 0.23)	0.49	(0.17, 0.85)
RW Aur B	-0.14	(-0.30, -0.04)	0.18	(-0.27, 0.63)	0.09	(0.02, 0.16)	0.71	(0.40, 1.11)	0.02	(-0.11, 0.08)	0.58	(0.24, 0.95)
CIDA 12	-0.66	(-0.76, -0.52)	0.51	(0.31, 0.90)	-0.60	(-0.84, -0.45)	0.65	(0.20, 1.01)	-0.65	(-0.83, -0.55)	0.67	(0.52, 0.95)

^aThe $\log M_*$ values (and their confidence intervals) in these composite multiple systems were determined by properly combining the marginal probability density functions determined for their individual components, as described in the text. The corresponding $\log t_*$ values (and their confidence intervals) correspond to the primary components.

^bThese systems are either known or strongly suspected to be associated with nearly edge-on disks. Since such a viewing geometry substantially obscures the starlight, the derived estimates of L_* for these cases are not used to determine masses and ages. Instead, we compute the weighted mean and standard deviation of the luminosities for the ensemble of sources with the same spectral type (± 1 subclass), and associate them with L_* and σ_L in the Bayesian inference method for $\{M_*, t_*\}$: details are available in Appendix B.

Note. — The units of the compiled stellar masses and ages are in units of M_\odot and Myr, respectively. The quantity CI(X) is meant to represent the extreme values of the variable X that span its 68.2% (“1- σ ”) confidence interval, derived from its associated marginal probability density function (see §3.2.1). As an example, consider the results for CIDA 12 from the SDF00 grid: an alternative (perhaps more familiar) way of quoting the measurements would be $\log M_* = -0.65^{+0.10}_{-0.18}$ and $\log t_* = 0.67^{+0.28}_{-0.15}$.

Table 4. Stellar Spectrum Fitting Results

Name	$\log(T_*/\text{K})$	$\log(L_*/L_\odot)$	A_V (mags)
IRAS 04108+2910	3.5855 ± 0.0237	-0.691 ± 0.290	1.73 ± 1.09
J04141188+2811535	3.4717 ± 0.0189	-1.746 ± 0.082	0.00 ± 1.43
FM Tau	3.5855 ± 0.0237	-0.393 ± 0.122	1.94 ± 0.64
FN Tau	3.4948 ± 0.0202	-0.082 ± 0.097	2.02 ± 0.73
CW Tau	3.6749 ± 0.0156	0.384 ± 0.205	3.17 ± 1.20
CIDA 1	3.4854 ± 0.0199	-0.901 ± 0.089	2.06 ± 0.68
MHO 1	3.5425 ± 0.0181	0.230 ± 0.883	12.75 ± 3.28
MHO 2 A ^a	3.5425 ± 0.0181	0.019 ± 0.189	9.00 ± 1.08
MHO 2 B ^a	3.4854 ± 0.0714	-0.491 ± 0.255	9.00 ± 1.08
MHO 3 A ^a	3.6085 ± 0.0225	-0.042 ± 0.188	7.29 ± 1.08
MHO 3 B ^a	3.5515 ± 0.0531	-0.453 ± 0.199	7.29 ± 1.08
FP Tau	3.5145 ± 0.0193	-0.490 ± 0.048	0.05 ± 0.39
CX Tau	3.5425 ± 0.0181	-0.431 ± 0.065	0.38 ± 0.42
FO Tau A	3.5241 ± 0.0188	-0.353 ± 0.080	2.40 ± 0.52
FO Tau B	3.5241 ± 0.0188	-0.495 ± 0.129	2.10 ± 0.65
J04153916+2818586	3.5193 ± 0.0190	-0.494 ± 0.071	2.21 ± 0.53
IRAS 04125+2902	3.5645 ± 0.0172	-0.500 ± 0.055	2.39 ± 0.49
J04155799+2746175	3.4854 ± 0.0199	-1.096 ± 0.097	1.38 ± 0.56
J04161210+2756385	3.4999 ± 0.0199	-1.084 ± 0.097	2.71 ± 0.56
J04163911+2858491	3.4854 ± 0.0199	-1.258 ± 0.077	3.50 ± 0.51
CY Tau	3.5602 ± 0.0173	-0.398 ± 0.090	0.44 ± 0.53
KPNO 10	3.4948 ± 0.0202	-1.129 ± 0.081	2.07 ± 0.55
V410 X-ray 1	3.5145 ± 0.0193	-0.351 ± 0.066	3.67 ± 0.39
V409 Tau	3.5602 ± 0.0173	-0.592 ± 0.084	0.66 ± 0.49
V410 Anon 13	3.4805 ± 0.0197	-0.987 ± 0.085	6.08 ± 0.62
DD Tau A	3.5241 ± 0.0188	-0.478 ± 0.216	0.90 ± 1.47
DD Tau B	3.5241 ± 0.0188	-0.583 ± 0.204	0.93 ± 1.36
CZ Tau A	3.5334 ± 0.0184	-0.730 ± 0.118	0.93 ± 0.71
CZ Tau B	3.4757 ± 0.0857	-1.135 ± 0.302	4.48 ± 2.26
V410 X-ray 2	3.5855 ± 0.0237	0.430 ± 0.077	17.61 ± 0.76
V892 Tau A ^a	4.0755 ± 0.1277	2.171 ± 0.653	10.04 ± 0.69
V892 Tau B ^a	4.0755 ± 0.1277	2.171 ± 0.653	10.04 ± 0.69
LR 1	3.6503 ± 0.0187	0.406 ± 0.135	28.15 ± 1.25
V410 X-ray 7 A ^a	3.5730 ± 0.0228	-0.326 ± 0.133	8.20 ± 0.78
V410 X-ray 7 B ^a	3.5380 ± 0.0365	-0.549 ± 0.164	8.20 ± 0.78
V410 X-ray 6	3.4854 ± 0.0199	-0.454 ± 0.050	3.48 ± 0.48
KPNO 12	3.3802 ± 0.0561	-2.973 ± 0.238	1.88 ± 1.78
FQ Tau A	3.5334 ± 0.0184	-1.068 ± 0.134	0.96 ± 0.83
FQ Tau B	3.5241 ± 0.0188	-0.931 ± 0.136	0.96 ± 1.07
BP Tau	3.6085 ± 0.0225	-0.012 ± 0.122	0.75 ± 0.58
V819 Tau	3.6085 ± 0.0225	-0.039 ± 0.076	1.60 ± 0.43
FR Tau	3.4901 ± 0.0200	-0.959 ± 0.058	0.23 ± 0.44
J04201611+2821325	3.4676 ± 0.0207	-1.870 ± 0.082	2.30 ± 0.70
J04202144+2813491 ^b	3.5688 ± 0.0170	-2.718 ± 0.110	0.55 ± 0.59
J04202555+2700355	3.4901 ± 0.0200	-1.343 ± 0.050	3.17 ± 0.49
IRAS 04173+2812	3.5145 ± 0.0193	-1.037 ± 0.123	12.21 ± 1.18

Table 4—Continued

Name	$\log(T_*/\text{K})$	$\log(L_*/L_\odot)$	A_V (mags)
J04202606+2804089	3.5241 ± 0.0188	-0.731 ± 0.041	0.50 ± 0.46
J04210795+2702204	3.4901 ± 0.0200	-1.205 ± 0.119	6.25 ± 0.67
J04210934+2750368	3.4901 ± 0.0200	-0.973 ± 0.106	1.16 ± 0.64
J04213459+2701388	3.4854 ± 0.0199	-0.912 ± 0.075	3.65 ± 0.54
IRAS 04187+1927	3.5855 ± 0.0237	0.152 ± 0.095	4.90 ± 0.60
J04214631+2659296	3.4805 ± 0.0197	-1.529 ± 0.074	4.72 ± 0.50
DE Tau	3.5688 ± 0.0170	0.014 ± 0.069	1.14 ± 0.61
RY Tau	3.7059 ± 0.0154	1.123 ± 0.159	2.25 ± 0.61
T Tau N	3.7202 ± 0.0141	1.130 ± 0.140	2.09 ± 0.44
FS Tau A	3.5855 ± 0.0237	0.041 ± 0.142	6.67 ± 0.86
FS Tau B	3.5241 ± 0.0188	-0.887 ± 0.171	5.04 ± 0.78
J04221675+2654570	3.5602 ± 0.0173	-0.508 ± 0.116	4.37 ± 0.65
IRAS 04196+2638	3.5688 ± 0.0170	-0.413 ± 0.108	5.57 ± 0.52
J04230607+2801194	3.4757 ± 0.0196	-1.332 ± 0.078	1.66 ± 0.51
IRAS 04200+2759	3.5515 ± 0.0177	-1.261 ± 0.242	1.96 ± 0.98
J04231822+2641156	3.5241 ± 0.0188	-0.638 ± 0.059	6.87 ± 0.47
FU Tau A	3.4529 ± 0.0314	-0.579 ± 0.162	2.66 ± 1.14
FU Tau B	3.3711 ± 0.0522	-2.077 ± 0.161	4.31 ± 1.59
FT Tau	3.5772 ± 0.0491	-0.251 ± 0.219	2.45 ± 1.53
J04242090+2630511	3.4676 ± 0.0207	-1.806 ± 0.096	1.87 ± 0.70
J04242646+2649503	3.4805 ± 0.0197	-1.517 ± 0.068	2.14 ± 0.51
IRAS 04216+2603	3.5772 ± 0.0204	-0.671 ± 0.443	3.07 ± 1.87
IP Tau	3.5855 ± 0.0237	-0.331 ± 0.126	0.51 ± 0.68
KPNO 3	3.4757 ± 0.0196	-1.655 ± 0.053	2.32 ± 0.42
FV Tau A	3.6385 ± 0.0240	0.369 ± 0.143	6.09 ± 0.66
FV Tau B	3.6238 ± 0.0150	0.130 ± 0.153	6.77 ± 0.66
FV Tau/c A	3.5425 ± 0.0181	-0.254 ± 0.080	4.16 ± 0.49
FV Tau/c B	3.6238 ± 0.0188	-1.193 ± 0.210	6.34 ± 0.94
KPNO 13	3.4948 ± 0.0202	-0.577 ± 0.080	3.51 ± 0.52
DF Tau A	3.5515 ± 0.0177	0.084 ± 0.132	0.50 ± 0.86
DF Tau B	3.5425 ± 0.0181	-0.173 ± 0.109	0.25 ± 0.87
DG Tau	3.6238 ± 0.0150	0.323 ± 0.430	1.29 ± 1.06
J04284263+2714039 A ^a	3.4901 ± 0.0200	-1.258 ± 0.143	2.19 ± 1.49
J04284263+2714039 B ^a	3.4594 ± 0.0724	-1.575 ± 0.250	2.19 ± 1.49
IRAS 04260+2642 ^b	3.6312 ± 0.0195	-1.386 ± 0.319	6.54 ± 2.58
IRAS 04263+2654	3.4901 ± 0.0200	-0.115 ± 0.073	6.17 ± 0.53
XEST 13-010	3.5334 ± 0.0184	-0.296 ± 0.093	3.76 ± 0.55
DH Tau A	3.5688 ± 0.0170	-0.262 ± 0.110	1.18 ± 0.56
DH Tau B	3.4464 ± 0.0373	-2.822 ± 0.111	0.09 ± 1.33
IQ Tau	3.5772 ± 0.0204	-0.089 ± 0.119	1.39 ± 0.56
J04295950+2433078	3.4948 ± 0.0202	-0.613 ± 0.072	5.13 ± 0.48
UX Tau A	3.6902 ± 0.0160	0.273 ± 0.169	1.14 ± 0.75
KPNO 6	3.4074 ± 0.0433	-2.468 ± 0.179	1.28 ± 1.40
FX Tau A	3.5688 ± 0.0170	-0.285 ± 0.215	1.82 ± 1.51
FX Tau B	3.5145 ± 0.0193	-0.467 ± 0.142	0.43 ± 1.29
DK Tau A	3.6010 ± 0.0231	0.119 ± 0.189	1.46 ± 1.24

Table 4—Continued

Name	$\log (T_*/\text{K})$	$\log (L_*/L_\odot)$	A_V (mags)
DK Tau B	3.5688 ± 0.0170	-0.498 ± 0.237	1.31 ± 2.29
ZZ Tau A ^a	3.5334 ± 0.0184	-0.466 ± 0.117	0.97 ± 0.76
ZZ Tau B ^a	3.5048 ± 0.0394	-0.639 ± 0.145	0.97 ± 0.76
ZZ Tau IRS	3.4948 ± 0.0202	-1.022 ± 0.113	4.30 ± 0.62
KPNO 7	3.4204 ± 0.0466	-2.272 ± 0.198	1.57 ± 1.57
JH 56	3.5772 ± 0.0204	-0.376 ± 0.065	0.00 ± 0.68
XZ Tau A	3.5515 ± 0.0177	-0.443 ± 0.265	1.32 ± 0.96
XZ Tau B	3.5241 ± 0.0188	-0.227 ± 0.239	4.83 ± 1.48
HK Tau A	3.5772 ± 0.0204	-0.353 ± 0.126	2.65 ± 2.03
HK Tau B ^b	3.5515 ± 0.0177	-1.571 ± 0.194	1.92 ± 0.87
V710 Tau A	3.5772 ± 0.0204	-0.241 ± 0.124	1.91 ± 0.69
V710 Tau B ^c	3.5515 ± 0.0177	-0.330 ± 0.180	1.86 ± 0.88
LkH α 267	3.5334 ± 0.0184	-0.758 ± 0.080	5.68 ± 0.56
Haro 6-13	3.5855 ± 0.0237	-0.159 ± 0.115	5.43 ± 0.56
MHO 5	3.4757 ± 0.0196	-0.827 ± 0.071	2.12 ± 0.55
MHO 6	3.4999 ± 0.0199	-1.134 ± 0.122	1.01 ± 0.67
J04322415+2251083	3.5048 ± 0.0197	-1.040 ± 0.065	1.68 ± 0.52
GG Tau Aa	3.6085 ± 0.0225	-0.070 ± 0.123	0.63 ± 0.63
GG Tau Ab	3.5772 ± 0.0204	-0.136 ± 0.107	3.04 ± 0.54
GG Tau Ba	3.4854 ± 0.0199	-0.926 ± 0.107	1.39 ± 0.63
GG Tau Bb	3.4464 ± 0.0373	-1.845 ± 0.124	0.87 ± 0.87
FY Tau	3.6385 ± 0.0240	0.206 ± 0.136	4.56 ± 0.68
FZ Tau	3.5855 ± 0.0237	0.100 ± 0.138	3.81 ± 0.71
UZ Tau Wa	3.5515 ± 0.0177	-0.488 ± 0.106	0.74 ± 0.55
UZ Tau Wb	3.5334 ± 0.0184	-0.691 ± 0.074	0.26 ± 0.53
UZ Tau Ea ^a	3.5688 ± 0.0170	-0.190 ± 0.229	1.62 ± 0.71
UZ Tau Eb ^a	3.5145 ± 0.0193	-0.549 ± 0.198	1.62 ± 0.71
JH 112 A ^a	3.6238 ± 0.0150	0.043 ± 0.131	4.15 ± 0.54
JH 112 B ^a	3.4074 ± 0.0773	-2.391 ± 0.223	4.15 ± 0.54
J04324938+2253082	3.5097 ± 0.0195	-0.352 ± 0.086	4.81 ± 0.46
GH Tau A	3.5515 ± 0.0177	-0.456 ± 0.073	0.29 ± 0.56
GH Tau B	3.5515 ± 0.0177	-0.402 ± 0.109	0.73 ± 0.59
V807 Tau A	3.6085 ± 0.0225	0.183 ± 0.163	0.80 ± 0.80
V807 Tau Ba ^{a,c}	3.5515 ± 0.0177	-0.345 ± 0.076	0.78 ± 0.48
V807 Tau Bb ^{a,c}	3.5470 ± 0.0179	-0.486 ± 0.088	0.78 ± 0.48
J04330945+2246487	3.4757 ± 0.0196	-1.310 ± 0.071	4.53 ± 0.55
IRAS 04301+2608 ^b	3.5855 ± 0.0237	-1.522 ± 0.100	6.20 ± 0.58
IRAS 04303+2240	3.5772 ± 0.0204	0.173 ± 0.075	7.81 ± 0.47
J04333278+1800436	3.5688 ± 0.0170	-0.721 ± 0.076	0.00 ± 1.00
GI Tau	3.6085 ± 0.0225	0.040 ± 0.176	1.91 ± 0.87
GK Tau	3.6085 ± 0.0225	0.129 ± 0.234	1.36 ± 0.84
IS Tau A	3.5855 ± 0.0237	-0.240 ± 0.098	3.30 ± 0.54
IS Tau B	3.5241 ± 0.0188	-0.965 ± 0.071	3.29 ± 0.53
DL Tau	3.6085 ± 0.0225	-0.131 ± 0.181	1.21 ± 0.72
J04333905+2227207	3.5558 ± 0.0175	-1.159 ± 0.118	2.81 ± 0.62
HN Tau A	3.6385 ± 0.0240	-0.376 ± 0.365	2.31 ± 1.31

Table 4—Continued

Name	$\log(T_*/\text{K})$	$\log(L_*/L_\odot)$	A_V (mags)
HN Tau B	3.5145 ± 0.0193	-1.558 ± 0.225	0.92 ± 1.30
J04334171+1750402	3.5145 ± 0.0193	-0.921 ± 0.062	1.58 ± 0.93
J04334465+2615005	3.4999 ± 0.0199	-0.565 ± 0.074	5.17 ± 0.50
DM Tau	3.5688 ± 0.0170	-0.646 ± 0.031	0.34 ± 0.44
CI Tau	3.6085 ± 0.0225	-0.032 ± 0.139	1.57 ± 0.72
IT Tau A	3.6749 ± 0.0156	0.155 ± 0.129	4.11 ± 0.64
IT Tau B	3.5145 ± 0.0193	-0.684 ± 0.165	3.61 ± 1.10
AA Tau	3.6085 ± 0.0225	-0.059 ± 0.252	1.24 ± 0.89
HO Tau	3.5772 ± 0.0204	-0.886 ± 0.087	0.37 ± 0.50
DN Tau	3.5855 ± 0.0237	-0.104 ± 0.083	0.36 ± 0.51
CoKu Tau/3 A ^a	3.5688 ± 0.0170	-0.221 ± 0.104	4.93 ± 0.68
CoKu Tau/3 B ^a	3.5048 ± 0.0394	-0.699 ± 0.137	4.93 ± 0.68
HQ Tau	3.6902 ± 0.0160	0.591 ± 0.118	2.95 ± 0.52
HP Tau	3.6749 ± 0.0156	0.292 ± 0.111	3.40 ± 0.50
Haro 6-28 A	3.5515 ± 0.0177	-0.664 ± 0.103	3.22 ± 0.82
Haro 6-28 B	3.5241 ± 0.0188	-0.799 ± 0.192	6.74 ± 1.67
J04362151+2351165	3.4901 ± 0.0200	-1.807 ± 0.069	0.63 ± 0.56
ITG 1	3.5048 ± 0.0295	-2.079 ± 0.136	1.05 ± 0.75
J04381486+2611399	3.4529 ± 0.0314	-2.358 ± 0.192	2.26 ± 1.18
GM Tau	3.4676 ± 0.0207	-1.507 ± 0.076	0.28 ± 0.54
DO Tau	3.5855 ± 0.0237	0.144 ± 0.180	2.94 ± 0.85
HV Tau C ^b	3.6238 ± 0.0150	-1.562 ± 0.119	1.72 ± 0.62
J04385859+2336351	3.5097 ± 0.0195	-1.148 ± 0.202	1.75 ± 0.69
J04390163+2336029	3.4757 ± 0.0196	-1.054 ± 0.035	0.00 ± 0.33
J04390396+2544264	3.4529 ± 0.0314	-1.336 ± 0.148	2.89 ± 1.12
VY Tau A ^a	3.5855 ± 0.0237	-0.498 ± 0.084	0.64 ± 0.45
VY Tau B ^a	3.5048 ± 0.0394	-1.125 ± 0.139	0.64 ± 0.45
LkCa 15	3.6385 ± 0.0240	-0.092 ± 0.170	0.99 ± 0.63
GN Tau A ^a	3.5425 ± 0.0181	-0.328 ± 0.116	3.48 ± 0.81
GN Tau B ^a	3.5425 ± 0.0181	-0.409 ± 0.097	3.48 ± 0.81
J04393364+2359212	3.4948 ± 0.0202	-1.031 ± 0.095	1.22 ± 0.52
ITG 15	3.4948 ± 0.0202	-0.295 ± 0.085	4.16 ± 0.54
CFHT 4	3.4594 ± 0.0256	-0.756 ± 0.116	5.67 ± 0.89
J04400067+2358211	3.4757 ± 0.0196	-1.547 ± 0.131	0.50 ± 1.20
IRAS 04370+2559	3.5772 ± 0.0491	-0.047 ± 0.150	10.65 ± 0.75
J04403979+2519061 A ^a	3.4901 ± 0.0200	-1.022 ± 0.083	3.96 ± 0.99
J04403979+2519061 B ^a	3.4594 ± 0.0724	-1.350 ± 0.183	3.96 ± 0.99
JH 223 A ^a	3.5515 ± 0.0177	-0.647 ± 0.068	1.71 ± 0.47
JH 223 B ^a	3.4757 ± 0.0407	-1.725 ± 0.095	1.71 ± 0.47
ITG 33A ^b	3.5334 ± 0.0184	-1.372 ± 0.096	4.85 ± 0.57
ITG 34	3.4854 ± 0.0199	-1.318 ± 0.113	4.28 ± 0.67
CoKu Tau/4 A ^a	3.5602 ± 0.0173	-0.513 ± 0.082	2.32 ± 0.69
CoKu Tau/4 B ^a	3.5515 ± 0.0354	-0.604 ± 0.091	2.32 ± 0.69
ITG 40	3.5241 ± 0.0188	-0.602 ± 0.210	19.49 ± 2.80
IRAS 04385+2550	3.5855 ± 0.0237	-0.425 ± 0.086	5.24 ± 0.48
J04414489+2301513	3.4074 ± 0.0433	-2.262 ± 0.182	1.40 ± 1.49

Table 4—Continued

Name	$\log (T_*/\text{K})$	$\log (L_*/L_\odot)$	A_V (mags)
J04414825+2534304	3.4397 ± 0.0434	-1.683 ± 0.195	3.22 ± 1.48
V955 Tau A	3.6085 ± 0.0225	0.016 ± 0.137	4.67 ± 0.71
V955 Tau B	3.5425 ± 0.0181	-0.414 ± 0.113	4.32 ± 0.54
CIDA 7	3.4999 ± 0.0199	-0.897 ± 0.078	2.01 ± 0.51
DP Tau A ^a	3.5772 ± 0.0204	-0.608 ± 0.231	1.30 ± 0.73
DP Tau B ^a	3.5515 ± 0.0265	-0.780 ± 0.220	1.30 ± 0.73
GO Tau	3.5855 ± 0.0237	-0.544 ± 0.121	1.73 ± 0.60
CIDA 14	3.4948 ± 0.0202	-0.617 ± 0.094	1.25 ± 0.61
IRAS 04414+2506	3.4529 ± 0.0314	-1.203 ± 0.154	2.05 ± 1.12
IRAS 04429+1550	3.5425 ± 0.0181	-0.614 ± 0.037	0.00 ± 0.22
DQ Tau A ^a	3.5855 ± 0.0237	-0.395 ± 0.164	1.51 ± 0.60
DQ Tau B ^a	3.5855 ± 0.0237	-0.395 ± 0.164	1.51 ± 0.60
Haro 6-37 A	3.6085 ± 0.0225	-0.118 ± 0.145	1.82 ± 0.80
Haro 6-37 B	3.5145 ± 0.0578	-0.684 ± 0.169	4.23 ± 2.19
Haro 6-37 C	3.5688 ± 0.0170	-0.515 ± 0.129	1.46 ± 0.60
DR Tau	3.6385 ± 0.0240	0.259 ± 0.146	1.36 ± 0.77
DS Tau	3.6385 ± 0.0240	-0.119 ± 0.162	0.76 ± 0.71
UY Aur A	3.5855 ± 0.0237	0.005 ± 0.159	1.12 ± 0.92
UY Aur B	3.5425 ± 0.0181	-0.288 ± 0.160	6.17 ± 1.53
St 34 A ^a	3.5334 ± 0.0184	-1.115 ± 0.072	0.04 ± 0.78
St 34 B ^a	3.5334 ± 0.0184	-1.115 ± 0.072	0.04 ± 0.78
St 34 C	3.4854 ± 0.0199	-1.825 ± 0.101	0.54 ± 1.08
GM Aur	3.6749 ± 0.0156	0.091 ± 0.100	1.37 ± 0.55
J04554535+3019389	3.4999 ± 0.0199	-1.122 ± 0.036	0.00 ± 0.43
AB Aur	3.9720 ± 0.0521	1.566 ± 0.385	0.31 ± 0.73
J04554801+3028050	3.4854 ± 0.0199	-1.807 ± 0.075	0.78 ± 0.63
J04554969+3019400	3.4757 ± 0.0196	-1.695 ± 0.068	0.09 ± 1.10
XEST 26-062	3.5145 ± 0.0193	-0.576 ± 0.098	1.41 ± 0.70
SU Aur	3.7419 ± 0.0212	1.030 ± 0.148	1.15 ± 0.49
XEST 26-071	3.5241 ± 0.0188	-0.924 ± 0.090	1.12 ± 0.67
MWC 480	3.9206 ± 0.0203	1.282 ± 0.273	0.34 ± 0.66
V836 Tau	3.6085 ± 0.0225	-0.246 ± 0.113	1.19 ± 0.55
CIDA 8	3.5241 ± 0.0188	-0.704 ± 0.068	1.55 ± 0.45
CIDA 9 A	3.6010 ± 0.0231	-1.010 ± 0.255	2.12 ± 1.05
CIDA 9 B	3.5602 ± 0.0347	-1.089 ± 0.408	5.23 ± 2.75
CIDA 11 A ^a	3.5241 ± 0.0188	-0.932 ± 0.105	0.39 ± 0.57
CIDA 11 B ^a	3.5048 ± 0.0295	-1.046 ± 0.137	0.39 ± 0.57
RW Aur A	3.6826 ± 0.0239	0.276 ± 0.168	0.37 ± 0.75
RW Aur B	3.6385 ± 0.0240	-0.101 ± 0.185	2.35 ± 0.79
CIDA 12	3.5145 ± 0.0193	-1.095 ± 0.056	0.26 ± 0.47

^aThe stellar parameters for these close pairs were determined by simultaneous fits to both their composite SEDs and any available contrast ratios, assuming that both components have the same extinction.

^bThese stars are known or suspected to host edge-on disks. The luminosities and extinctions reported here are the results of the formal measurements described in Appendix B. However, their L_* values are modified before use in §3.2, as described in the text.

^cThe components V807 Tau Bab and V710 Tau B are included here for

completeness, but are not considered part of the Class II sample. The stellar photosphere parameters listed here were used to subtract off their contribution to the composite SEDs shown in Appendix B.

REFERENCES

- Adams, F. C., Emerson, J. P., & Fuller, G. A. 1990, *ApJ*, 357, 606
- Adelman-McCarthy, J. K., & et al. 2011, *VizieR Online Data Catalog*, 2306, 0
- Akeson, R. L., Koerner, D. W., & Jensen, E. L. N. 1998, *ApJ*, 505, 358
- Alibert, Y., Mordasini, C., & Benz, W. 2011, *A&A*, 526, A63
- Alibert, Y., Mordasini, C., Benz, W., & Winisdoerffer, C. 2005, *A&A*, 434, 343
- Allard, F., Guillot, T., Ludwig, H.-G., et al. 2003, in *IAU Symposium*, Vol. 211, *Brown Dwarfs*, ed. E. Martín, 325
- Allard, F., Homeier, D., & Freytag, B. 2011, in *Astronomical Society of the Pacific Conference Series*, Vol. 448, *16th Cambridge Workshop on Cool Stars, Stellar Systems, and the Sun*, ed. C. Johns-Krull, M. K. Browning, & A. A. West, 91
- Altenhoff, W. J., Thum, C., & Wendker, H. J. 1994, *A&A*, 281, 161
- Andrews, S. M., & Williams, J. P. 2005, *ApJ*, 631, 1134
- . 2007a, *ApJ*, 671, 1800
- . 2007b, *ApJ*, 659, 705
- Andrews, S. M., Wilner, D. J., Espaillat, C., et al. 2011, *ApJ*, 732, 42
- Andrews, S. M., Wilner, D. J., Hughes, A. M., Qi, C., & Dullemond, C. P. 2009, *ApJ*, 700, 1502
- . 2010, *ApJ*, 723, 1241
- Apai, D., Pascucci, I., Sterzik, M. F., et al. 2004, *A&A*, 426, L53
- Artymowicz, P., & Lubow, S. H. 1994, *ApJ*, 421, 651
- Audard, M., Briggs, K. R., Grosso, N., et al. 2007, *A&A*, 468, 379
- Bailer-Jones, C. A. L. 2011, *MNRAS*, 411, 435
- Baraffe, I., Chabrier, G., Allard, F., & Hauschildt, P. H. 1998, *A&A*, 337, 403
- Basri, G., & Batalha, C. 1990, *ApJ*, 363, 654
- Bastian, U., & Mundt, R. 1979, *A&AS*, 36, 57
- Beckwith, S. V. W., & Sargent, A. I. 1991, *ApJ*, 381, 250
- Beckwith, S. V. W., Sargent, A. I., Chini, R. S., & Guesten, R. 1990, *AJ*, 99, 924

- Beichman, C. A., Neugebauer, G., Habing, H. J., Clegg, P. E., & Chester, T. J., eds. 1988, Infrared astronomical satellite (IRAS) catalogs and atlases. Volume 1: Explanatory supplement, Vol. 1
- Beskrovnaya, N. G., & Pogodin, M. A. 2004, *A&A*, 414, 955
- Bessell, M. S. 1979, *PASP*, 91, 589
- Birnstiel, T., Dullemond, C. P., & Brauer, F. 2010, *A&A*, 513, A79
- Birnstiel, T., Klahr, H., & Ercolano, B. 2012, *A&A*, 539, A148
- Birnstiel, T., Ormel, C. W., & Dullemond, C. P. 2011, *A&A*, 525, A11
- Boss, A. P. 1997, *Science*, 276, 1836
- . 2006, *ApJ*, 643, 501
- Bouvier, J., Bertout, C., & Bouchet, P. 1988, *A&AS*, 75, 1
- Bouvier, J., Cabrit, S., Fernandez, M., Martin, E. L., & Matthews, J. M. 1993, *A&AS*, 101, 485
- Bouvier, J., Covino, E., Kovo, O., et al. 1995, *A&A*, 299, 89
- Bouy, H., Huélamo, N., Pinte, C., et al. 2008, *A&A*, 486, 877
- Bowler, B. P., Johnson, J. A., Marcy, G. W., et al. 2010, *ApJ*, 709, 396
- Brauer, F., Dullemond, C. P., & Henning, T. 2008, *A&A*, 480, 859
- Briceño, C., Luhman, K. L., Hartmann, L., Stauffer, J. R., & Kirkpatrick, J. D. 2002, *ApJ*, 580, 317
- Brown, T. M., Latham, D. W., Everett, M. E., & Esquerdo, G. A. 2011, *AJ*, 142, 112
- Cabrit, S., Pety, J., Pesenti, N., & Dougados, C. 2006, *A&A*, 452, 897
- Cardelli, J. A., Clayton, G. C., & Mathis, J. S. 1989, *ApJ*, 345, 245
- Carpenter, J. M. 2001, *AJ*, 121, 2851
- Carpenter, J. M., Hillenbrand, L. A., & Skrutskie, M. F. 2001, *AJ*, 121, 3160
- Carpenter, J. M., Wolf, S., Schreyer, K., Launhardt, R., & Henning, T. 2005, *AJ*, 129, 1049
- Chen, C. H., & Jura, M. 2003, *ApJ*, 591, 267
- Chiang, E. I., & Goldreich, P. 1997, *ApJ*, 490, 368

- Cieza, L. A., Kessler-Silacci, J. E., Jaffe, D. T., Harvey, P. M., & Evans, II, N. J. 2005, *ApJ*, 635, 422
- Cieza, L. A., Schreiber, M. R., Romero, G. A., et al. 2012, *ApJ*, 750, 157
- Corder, S., Eisner, J., & Sargent, A. 2005, *ApJ*, 622, L133
- Cutri, R. M., Skrutskie, M. F., van Dyk, S., et al. 2003, 2MASS All Sky Catalog of point sources.
- Da Rio, N., & Robberto, M. 2012, *AJ*, 144, 176
- Dahm, S. E., & Lyke, J. E. 2011, *PASP*, 123, 1383
- D’Alessio, P., Calvet, N., Hartmann, L., Franco-Hernández, R., & Servín, H. 2006, *ApJ*, 638, 314
- D’Alessio, P., Canto, J., Calvet, N., & Lizano, S. 1998, *ApJ*, 500, 411
- D’Antona, F., & Mazzitelli, I. 1997, *Mem. Soc. Astron. Italiana*, 68, 807
- D’Antona, F., & Mazzitelli, I. 1998, in *Astronomical Society of the Pacific Conference Series*, Vol. 134, *Brown Dwarfs and Extrasolar Planets*, ed. R. Rebolo, E. L. Martin, & M. R. Zapatero Osorio, 442
- de Winter, D., van den Ancker, M. E., Maira, A., et al. 2001, *A&A*, 380, 609
- Dent, W. R. F., Matthews, H. E., & Ward-Thompson, D. 1998, *MNRAS*, 301, 1049
- di Francesco, J., Evans, II, N. J., Harvey, P. M., et al. 1997, *ApJ*, 482, 433
- Duchêne, G., Ménard, F., Stapelfeldt, K., & Duvert, G. 2003, *A&A*, 400, 559
- Duchêne, G., Monin, J.-L., Bouvier, J., & Ménard, F. 1999, *A&A*, 351, 954
- Duchêne, G., McCabe, C., Pinte, C., et al. 2010, *ApJ*, 712, 112
- Dullemond, C. P., & Dominik, C. 2004, *A&A*, 421, 1075
- Dullemond, C. P., Dominik, C., & Natta, A. 2001, *ApJ*, 560, 957
- Durisen, R. H., Boss, A. P., Mayer, L., et al. 2007, *Protostars and Planets V*, 607
- Dutrey, A., Guilloteau, S., Duvert, G., et al. 1996, *A&A*, 309, 493
- Dutrey, A., Guilloteau, S., & Simon, M. 2003, *A&A*, 402, 1003
- Dutrey, A., Guilloteau, S., Piétu, V., et al. 2008, *A&A*, 490, L15
- Duvert, G., Guilloteau, S., Ménard, F., Simon, M., & Dutrey, A. 2000, *A&A*, 355, 165
- Eiroa, C., Garzón, F., Alberdi, A., et al. 2001, *A&A*, 365, 110

- Eiroa, C., Oudmaijer, R. D., Davies, J. K., et al. 2002, *A&A*, 384, 1038
- Espaillat, C., D’Alessio, P., Hernández, J., et al. 2010, *ApJ*, 717, 441
- Espaillat, C., Ingleby, L., Hernández, J., et al. 2012, *ApJ*, 747, 103
- Evans, D. W., Irwin, M. J., & Helmer, L. 2002, *VizieR Online Data Catalog*, 1282, 0
- Feigelson, E. D., & Nelson, P. I. 1985, *ApJ*, 293, 192
- Fischer, W., Edwards, S., Hillenbrand, L., & Kwan, J. 2011, *ApJ*, 730, 73
- Foreman-Mackey, D., Hogg, D. W., Lang, D., & Goodman, J. 2013, *PASP*, 125, 306
- Fukugita, M., Ichikawa, T., Gunn, J. E., et al. 1996, *AJ*, 111, 1748
- Furlan, E., Luhman, K. L., Espaillat, C., et al. 2011, *ApJS*, 195, 3
- Gahm, G. F., Walter, F. M., Stempels, H. C., Petrov, P. P., & Herczeg, G. J. 2008, *A&A*, 482, L35
- Gennaro, M., Prada Moroni, P. G., & Tognelli, E. 2012, *MNRAS*, 420, 986
- Goodman, J., & Weare, J. 2010, *Comm. App. Math. Comp. Sci.*, 5, 65
- Gräfe, C., Wolf, S., Roccatagliata, V., Sauter, J., & Ertel, S. 2011, *A&A*, 533, A89
- Grankin, K. N., Bouvier, J., Herbst, W., & Melnikov, S. Y. 2008, *A&A*, 479, 827
- Grankin, K. N., Melnikov, S. Y., Bouvier, J., Herbst, W., & Shevchenko, V. S. 2007, *A&A*, 461, 183
- Gregorio-Hetem, J., Lepine, J. R. D., Quast, G. R., Torres, C. A. O., & de La Reza, R. 1992, *AJ*, 103, 549
- Guieu, S., Dougados, C., Monin, J.-L., Magnier, E., & Martín, E. L. 2006, *A&A*, 446, 485
- Guilloteau, S., & Dutrey, A. 1998, *A&A*, 339, 467
- Guilloteau, S., Dutrey, A., Piétu, V., & Boehler, Y. 2011, *A&A*, 529, A105
- Guilloteau, S., Dutrey, A., & Simon, M. 1999, *A&A*, 348, 570
- Gullbring, E., Hartmann, L., Briceno, C., & Calvet, N. 1998, *ApJ*, 492, 323
- Hamidouche, M. 2010, *ApJ*, 722, 204
- Hamidouche, M., Looney, L. W., & Mundy, L. G. 2006, *ApJ*, 651, 321
- Harris, R. J., Andrews, S. M., C. C. J., Wilner, D. J., & Kraus, A. L. 2013, *ApJ*, 751, 115

- Harris, R. J., Andrews, S. M., Wilner, D. J., & Kraus, A. L. 2012, *ApJ*, 751, 115
- Hartigan, P., Edwards, S., & Ghandour, L. 1995, *ApJ*, 452, 736
- Hartigan, P., & Kenyon, S. J. 2003, *ApJ*, 583, 334
- Hartigan, P., Kenyon, S. J., Hartmann, L., et al. 1991, *ApJ*, 382, 617
- Hartigan, P., Strom, K. M., & Strom, S. E. 1994, *ApJ*, 427, 961
- Hartmann, L., Calvet, N., Gullbring, E., & D’Alessio, P. 1998, *ApJ*, 495, 385
- Harvey, P. M., Henning, T., Liu, Y., et al. 2012, *ApJ*, 755, 67
- Hauschildt, P. H., Allard, F., & Baron, E. 1999, *ApJ*, 512, 377
- Henning, T., Burkert, A., Launhardt, R., Leinert, C., & Stecklum, B. 1998, *A&A*, 336, 565
- Herbig, G. H. 1978, *Can Post-T Tauri Stars Be Found?*, ed. L. V. Mirzoyan, 171
- Herbst, W., Herbst, D. K., Grossman, E. J., & Weinstein, D. 1994, *AJ*, 108, 1906
- Herbst, W., & Shevchenko, V. S. 1999, *AJ*, 118, 1043
- Herczeg, G. J., & Hillenbrand, L. A. 2008, *ApJ*, 681, 594
- Hernández, J., Calvet, N., Briceño, C., Hartmann, L., & Berlind, P. 2004, *AJ*, 127, 1682
- Hillenbrand, L. A. 1997, *AJ*, 113, 1733
- Hillenbrand, L. A., Strom, S. E., Vrba, F. J., & Keene, J. 1992, *ApJ*, 397, 613
- Hillenbrand, L. A., & White, R. J. 2004, *ApJ*, 604, 741
- Ho, P. T. P., Moran, J. M., & Lo, K. Y. 2004, *ApJ*, 616, L1
- Hogerheijde, M. R., van Langevelde, H. J., Mundy, L. G., Blake, G. A., & van Dishoeck, E. F. 1997, *ApJ*, 490, L99
- Honda, M., Inoue, A. K., Okamoto, Y. K., et al. 2010, *ApJ*, 718, L199
- Hubickyj, O., Bodenheimer, P., & Lissauer, J. J. 2005, *Icarus*, 179, 415
- Hughes, A. M., Wilner, D. J., Qi, C., & Hogerheijde, M. R. 2008, *ApJ*, 678, 1119
- Hughes, A. M., Andrews, S. M., Espaillat, C., et al. 2009, *ApJ*, 698, 131
- Ida, S., & Lin, D. N. C. 2004, *ApJ*, 604, 388
- . 2005, *ApJ*, 626, 1045

- . 2008, *ApJ*, 673, 487
- Ikoma, M., Nakazawa, K., & Emori, H. 2000, *ApJ*, 537, 1013
- Isella, A., Carpenter, J. M., & Sargent, A. I. 2009, *ApJ*, 701, 260
- . 2010, *ApJ*, 714, 1746
- Isella, A., Pérez, L. M., & Carpenter, J. M. 2012, *ApJ*, 747, 136
- Ishihara, D., Onaka, T., Kataza, H., et al. 2010, *A&A*, 514, A1
- Isobe, T., Feigelson, E. D., & Nelson, P. I. 1986, *ApJ*, 306, 490
- Itoh, Y., Hayashi, M., Tamura, M., et al. 2005, *ApJ*, 620, 984
- Jayawardhana, R., Ardila, D. R., Stelzer, B., & Haisch, Jr., K. E. 2003, *AJ*, 126, 1515
- Jensen, E. L. N., & Akeson, R. L. 2003, *ApJ*, 584, 875
- Jensen, E. L. N., Mathieu, R. D., & Fuller, G. A. 1994, *ApJ*, 429, L29
- . 1996, *ApJ*, 458, 312
- Jewitt, D. C. 1994, *AJ*, 108, 661
- Johnson, J. A., Butler, R. P., Marcy, G. W., et al. 2007, *ApJ*, 670, 833
- Johnson, J. A., Howard, A. W., Marcy, G. W., et al. 2010, *PASP*, 122, 149
- Jørgensen, B. R., & Lindegren, L. 2005, *A&A*, 436, 127
- Kelly, B. C. 2007, *ApJ*, 665, 1489
- Kennedy, G. M., & Kenyon, S. J. 2008, *ApJ*, 673, 502
- Kenyon, S. J., Gomez, M., Marzke, R. O., & Hartmann, L. 1994, *AJ*, 108, 251
- Kenyon, S. J., Gómez, M., & Whitney, B. A. 2008, *Low Mass Star Formation in the Taurus-Auriga Clouds*, ed. B. Reipurth, 405
- Kenyon, S. J., & Hartmann, L. 1995, *ApJS*, 101, 117
- Kitamura, Y., Kawabe, R., & Saito, M. 1996, *ApJ*, 465, L137
- Kitamura, Y., Momose, M., Yokogawa, S., et al. 2002, *ApJ*, 581, 357
- Klein, R., Apai, D., Pascucci, I., Henning, T., & Waters, L. B. F. M. 2003, *ApJ*, 593, L57
- Koerner, D. W., Chandler, C. J., & Sargent, A. I. 1995, *ApJ*, 452, L69

- Konopacky, Q. M., Ghez, A. M., Rice, E. L., & Duchêne, G. 2007, *ApJ*, 663, 394
- Kornet, K., Wolf, S., & Różyczka, M. 2006, *A&A*, 458, 661
- Kraus, A. L., & Hillenbrand, L. A. 2007, *ApJ*, 662, 413
- . 2009, *ApJ*, 703, 1511
- Kraus, A. L., Ireland, M. J., Martinache, F., & Hillenbrand, L. A. 2011, *ApJ*, 731, 8
- Kraus, A. L., White, R. J., & Hillenbrand, L. A. 2006, *ApJ*, 649, 306
- Kundurthy, P., Meyer, M. R., Robberto, M., Beckwith, S. V. W., & Herbst, T. 2006, *AJ*, 132, 2469
- Laughlin, G., Bodenheimer, P., & Adams, F. C. 2004, *ApJ*, 612, L73
- Lee, N., Williams, J. P., & Cieza, L. A. 2011, *ApJ*, 736, 135
- Lejeune, T., Cuisinier, F., & Buser, R. 1997, *A&AS*, 125, 229
- Lin, S.-Y., Ohashi, N., Lim, J., et al. 2006, *ApJ*, 645, 1297
- Liu, M. C., Najita, J., & Tokunaga, A. T. 2003, *ApJ*, 585, 372
- Loinard, L., Torres, R. M., Mioduszewski, A. J., et al. 2007, *ApJ*, 671, 546
- Looney, L. W., Mundy, L. G., & Welch, W. J. 2000, *ApJ*, 529, 477
- Luhman, K. L. 1999, *ApJ*, 525, 466
- . 2000, *ApJ*, 544, 1044
- . 2004, *ApJ*, 617, 1216
- Luhman, K. L., Allen, P. R., Espaillat, C., Hartmann, L., & Calvet, N. 2010, *ApJS*, 186, 111
- Luhman, K. L., Mamajek, E. E., Allen, P. R., & Cruz, K. L. 2009a, *ApJ*, 703, 399
- Luhman, K. L., Mamajek, E. E., Allen, P. R., Muench, A. A., & Finkbeiner, D. P. 2009b, *ApJ*, 691, 1265
- Malfait, K., Bogaert, E., & Waelkens, C. 1998, *A&A*, 331, 211
- Mann, R. K., & Williams, J. P. 2009, *ApJ*, 694, L36
- . 2010, *ApJ*, 725, 430
- Mannings, V., & Emerson, J. P. 1994, *MNRAS*, 267, 361
- Mannings, V., & Sargent, A. I. 1997, *ApJ*, 490, 792

- Mariñas, N., Telesco, C. M., Fisher, R. S., Packham, C., & Radomski, J. T. 2006, *ApJ*, 653, 1353
- Massarotti, A., Latham, D. W., Torres, G., Brown, R. A., & Oppenheimer, B. D. 2005, *AJ*, 129, 2294
- Mathews, G. S., Williams, J. P., Ménard, F., et al. 2012, *ApJ*, 745, 23
- Mathieu, R. D., Stassun, K., Basri, G., et al. 1997, *AJ*, 113, 1841
- Mathis, J. S. 1990, *ARA&A*, 28, 37
- McCabe, C., Duchêne, G., Pinte, C., et al. 2011, *ApJ*, 727, 90
- McCabe, C., Ghez, A. M., Prato, L., et al. 2006, *ApJ*, 636, 932
- McClure, M. 2009, *ApJ*, 693, L81
- Metchev, S. A., Hillenbrand, L. A., & Meyer, M. R. 2004, *ApJ*, 600, 435
- Momose, M., Ohashi, N., Kawabe, R., Hayashi, M., & Nakano, T. 1996, *ApJ*, 470, 1001
- Momose, M., Ohashi, N., Kudo, T., Tamura, M., & Kitamura, Y. 2010, *ApJ*, 712, 397
- Monnier, J. D., Tannirkulam, A., Tuthill, P. G., et al. 2008, *ApJ*, 681, L97
- Mora, A., Merín, B., Solano, E., et al. 2001, *A&A*, 378, 116
- Mordasini, C., Alibert, Y., & Benz, W. 2009, *A&A*, 501, 1139
- Moriarty-Schieven, G. H., Johnstone, D., Bally, J., & Jenness, T. 2006, *ApJ*, 645, 357
- Motte, F., & André, P. 2001, *A&A*, 365, 440
- Myers, P. C., Fuller, G. A., Mathieu, R. D., et al. 1987, *ApJ*, 319, 340
- Natta, A., Grinin, V., & Mannings, V. 2000, *Protostars and Planets IV*, 559
- Neuhaeuser, R., Sterzik, M. F., Schmitt, J. H. M. M., Wichmann, R., & Krautter, J. 1995, *A&A*, 297, 391
- Öberg, K. I., Qi, C., Fogel, J. K. J., et al. 2010, *ApJ*, 720, 480
- Ohashi, N., Hayashi, M., Kawabe, R., & Ishiguro, M. 1996, *ApJ*, 466, 317
- Osterloh, M., & Beckwith, S. V. W. 1995, *ApJ*, 439, 288
- Oudmaijer, R. D., Palacios, J., Eiroa, C., et al. 2001, *A&A*, 379, 564
- Palla, F., & Stahler, S. W. 1993, *ApJ*, 418, 414

- Pantin, E., Bouwman, J., & Lagage, P. O. 2005, *A&A*, 437, 525
- Pecaut, M. J., Mamajek, E. E., & Bubar, E. J. 2012, *ApJ*, 746, 154
- Pérez, L. M., Carpenter, J. M., Chandler, C. J., et al. 2012, *ApJ*, 760, L17
- Petrov, P. P., Zajtseva, G. V., Efimov, Y. S., et al. 1999, *A&A*, 341, 553
- Phan-Bao, N., Lee, C.-F., Ho, P. T. P., & Tang, Y.-W. 2011, *ApJ*, 735, 14
- Piétu, V., Dutrey, A., & Guilloteau, S. 2007, *A&A*, 467, 163
- Piétu, V., Dutrey, A., Guilloteau, S., Chapillon, E., & Pety, J. 2006, *A&A*, 460, L43
- Piétu, V., Gueth, F., Hily-Blant, P., Schuster, K.-F., & Pety, J. 2011, *A&A*, 528, A81
- Piétu, V., Guilloteau, S., & Dutrey, A. 2005, *A&A*, 443, 945
- Pollack, J. B., Hubickyj, O., Bodenheimer, P., et al. 1996, *Icarus*, 124, 62
- Prato, L., Simon, M., Mazeh, T., Zucker, S., & McLean, I. S. 2002, *ApJ*, 579, L99
- Ratzka, T., Schegerer, A. A., Leinert, C., et al. 2009, *A&A*, 502, 623
- Rebull, L. M., Padgett, D. L., McCabe, C.-E., et al. 2010, *ApJS*, 186, 259
- Ricci, L., Isella, A., Carpenter, J. M., & Testi, L. 2013, *ApJ*, 764, L27
- Ricci, L., Testi, L., Natta, A., et al. 2010, *A&A*, 512, A15
- Ricci, L., Trotta, F., Testi, L., et al. 2012, *A&A*, 540, A6
- Roberge, A., Lecavelier des Etangs, A., Grady, C. A., et al. 2001, *ApJ*, 551, L97
- Rodmann, J., Henning, T., Chandler, C. J., Mundy, L. G., & Wilner, D. J. 2006, *A&A*, 446, 211
- Rydgren, A. E. 1984, *Publications of the U.S. Naval Observatory Second Series*, 25, 1
- Rydgren, A. E., & Vrba, F. J. 1983, *AJ*, 88, 1017
- Sandell, G., Weintraub, D. A., & Hamidouche, M. 2011, *ApJ*, 727, 26
- Schaefer, G. H., Dutrey, A., Guilloteau, S., Simon, M., & White, R. J. 2009, *ApJ*, 701, 698
- Schaefer, G. H., Prato, L., Simon, M., & Zavala, R. T. 2012, *ApJ*, 756, 120
- Schaefer, G. H., Simon, M., Beck, T. L., Nelan, E., & Prato, L. 2006, *AJ*, 132, 2618
- Schmidt-Kaler, T. 1982, *Bulletin d'Information du Centre de Données Stellaires*, 23, 2
- Scholz, A., Jayawardhana, R., & Wood, K. 2006, *ApJ*, 645, 1498

- Siess, L., Dufour, E., & Forestini, M. 2000, *A&A*, 358, 593
- Simon, M., Dutrey, A., & Guilloteau, S. 2000, *ApJ*, 545, 1034
- Skemer, A. J., Close, L. M., Hinz, P. M., et al. 2010, *ApJ*, 711, 1280
- Skrutskie, M. F., Cutri, R. M., Stiening, R., et al. 2006, *AJ*, 131, 1163
- Slesnick, C. L., Carpenter, J. M., Hillenbrand, L. A., & Mamajek, E. E. 2006, *AJ*, 132, 2665
- Stahler, S. W. 1983, *ApJ*, 274, 822
- Straizys, V. 1992, Multicolor stellar photometry
- Strom, K. M., & Strom, S. E. 1994, *ApJ*, 424, 237
- Strom, K. M., Strom, S. E., Edwards, S., Cabrit, S., & Skrutskie, M. F. 1989, *AJ*, 97, 1451
- Takeuchi, T., & Lin, D. N. C. 2002, *ApJ*, 581, 1344
- Tamazian, V. S., Docobo, J. A., White, R. J., & Woitas, J. 2002, *ApJ*, 578, 925
- Tang, Y.-W., Guilloteau, S., Piétu, V., et al. 2012, *A&A*, 547, A84
- Thommes, E. W., Matsumura, S., & Rasio, F. A. 2008, *Science*, 321, 814
- Torres, C. A. O., Quast, G., de La Reza, R., Gregorio-Hetem, J., & Lepine, J. R. D. 1995, *AJ*, 109, 2146
- Torres, R. M., Loinard, L., Mioduszewski, A. J., et al. 2012, *ApJ*, 747, 18
- Torres, R. M., Loinard, L., Mioduszewski, A. J., & Rodríguez, L. F. 2009, *ApJ*, 698, 242
- Vieira, S. L. A., Corradi, W. J. B., Alencar, S. H. P., et al. 2003, *AJ*, 126, 2971
- Vrba, F. J., Chugainov, P. F., Weaver, W. B., & Stauffer, J. S. 1993, *AJ*, 106, 1608
- Vrba, F. J., Rydgren, A. E., Chugainov, P. F., Shakovskaia, N. I., & Weaver, W. B. 1989, *AJ*, 97, 483
- Vrba, F. J., Rydgren, A. E., Chugainov, P. F., Shakovskaia, N. I., & Zak, D. S. 1986, *ApJ*, 306, 199
- Wahhaj, Z., Cieza, L., Koerner, D. W., et al. 2010, *ApJ*, 724, 835
- Walker, M. F. 1987, *PASP*, 99, 392
- Weidenschilling, S. J. 1977, *MNRAS*, 180, 57
- Weintraub, D. A., Sandell, G., & Duncan, W. D. 1989, *ApJ*, 340, L69

- White, R. J., & Ghez, A. M. 2001, *ApJ*, 556, 265
- White, R. J., Ghez, A. M., Reid, I. N., & Schultz, G. 1999, *ApJ*, 520, 811
- White, R. J., & Hillenbrand, L. A. 2005, *ApJ*, 621, L65
- Williams, J. P., & Cieza, L. A. 2011, *ARA&A*, 49, 67
- Woitas, J., Leinert, C., & Köhler, R. 2001, *A&A*, 376, 982
- Wright, E. L., Eisenhardt, P. R. M., Mainzer, A. K., et al. 2010, *AJ*, 140, 1868